RICE UNIVERSITY

VOLATILE CYCLING AND THE THERMAL EVOLUTION OF PLANETARY MANTLE

by

Constantin Sandu

A THESIS SUBMITTED IN PARTIAL
FULFILLMENT OF THE REQUIREMENTS FOR
THE DEGREE OF

Doctor of Philosophy

Approved Thesis Committee

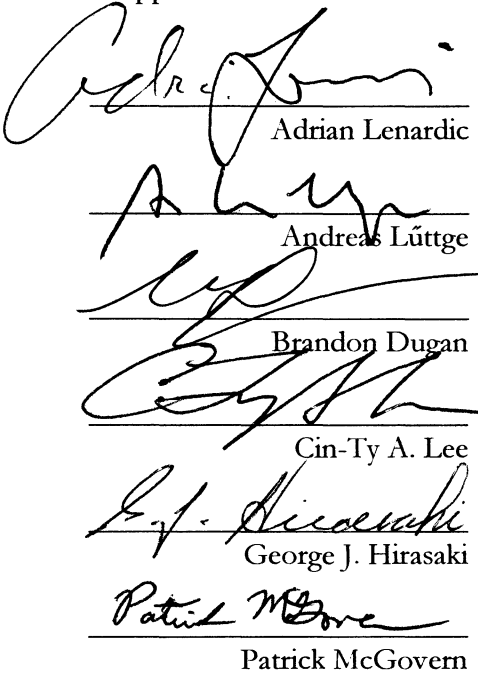

Adrian Lenardic

Andreas Lũttge

Brandon Dugan

Cin-Ty A. Lee

George J. Hirasaki

Patrick McGovern

HOUSTON, TEXAS

MAY 2010

ABSTRACT

VOLATILE CYCLING AND THE THERMAL EVOLUTION OF PLANETARY MANTLE

by Constantin Sandu

The thermal histories of terrestrial planets are investigated using two parameterized mantle convection models for either Earth like planets and planets with no active plate tectonics. Using parameterized models of mantle convection, we performed computer simulations of planetary cooling and volatile cycling. The models estimate the amount of volatile in mantle reservoir, and calculate the outgassing and regassing rates. A linear model of volatile concentration-dependent is assumed for the activation energy of the solid-state creep in the mantle. The kinematic viscosity of the mantle is thus dynamically affected by the activation energy through a variable concentration in volatile. Mantle temperature and heat flux is calculated using a model derived from classic thermal boundary layer theory of a single layered mantle with temperature dependent viscosity. The rate of volatile exchanged between mantle and surface is calculated by balancing the amount of volatiles degassed in the atmosphere by volcanic and spreading related processes and the amount of volatiles recycled back in the mantle by the subduction process. In the cases that lack plate tectonics, the degassing efficiency is dramatically reduced and the regassing process is absent. The degassing effect is dependent on average spreading rate of tectonic plates and on the amount of volatile in the melt extract in the transition zone between mantle and upper boundary layer. The regassing effect is dependent on the subduction rate and on the amount of volatile present on a hydrated layer on top of the subducting slab. The degassing and regassing parameters are all related to the intensity of the convection in the mantle and to the surface temperature of the

planet, and they are regulated by the amount of volatiles in reservoir. Comparative study with the previous models display significant differences and improve the versatility of the model. The optimum efficiency factors found are in the range of 0.01-0.06 for degassing/regassing processes, in agreement with more recent estimates. An important effect of the volatile cycling process is a general negative feedback effect that results in a general trend to adjust the mantle volatile content in time to a value set by the energy balance in the system. As a result, the initial amount of volatile in the mantle is rendered irrelevant for late stage of thermal evolution. In the case of no plate tectonics, the opposite effect takes place: initial volatilization plays an important role through entire evolution.

The implications of mantle convection on the stability of the lithosphere were investigated further using the thermal history calculations and numeric simulations. They point to the conclusion that mantle convection induced stress levels increase from the past to the present fact that leads to a greater potential of craton deformation. The main consequence of this trend is that sections of continental lithosphere that have remained stable since the Archean and Proterozoic are becoming progressively more prone to instability in the geologically modern era.

After the volatiles are degassed from the mantle, they are cycled through the atmosphere. They interact with the climate influencing the surface temperature, and further controlling the mantle convection. Using a grey radiative-convective model for the atmosphere, we analyzed the feedback relationships between volatiles, especially water, and surface temperature. We showed that large amount of water degassed during a hot, possible melt ocean phase after the planet formation could conserve large amount of water in atmosphere and maintain the surface temperature at moderate level.

ACKNOWLEDGEMENTS

It is great pleasure to thank the many people that surrounded me during the Ph.D. years: mentors, colleagues and family members. They all made this personal endeavor possible.

I am especially grateful to my doctoral adviser Adrian Lenardic whose inspiring wisdom and willingness to teach me how to think converted me into a scientist rather than a degree earner. Many thanks go also to the rest of the research committee, Andreas Luttge, Brandon Dugan, Cin-Ty Lee, and Patrick McGovern for their suggestions during my study at Rice and their reviews of the thesis manuscript. Special thanks also go to Sandra and Soookie for coordinating and helping with everything else than science a graduate student needs for life in the department.

Deep gratitude goes also to my family that provided me the warm environment and encouragements. To my wife Corina for her heavy support and patience. To my two sons Matei and Horia, that were born during these years, for giving me motivation and happiness. To my mother-in-law for picking up the multitude of the household tasks I would not have had time to sort out. To my parents far away from Houston but always close in thoughts.

I would also like to thank to many and impossible to list here among the previous teachers, scholars, friends, and colleagues that influenced me into love and devotion for knowledge, and helped me along the long road to the Ph.D. program.

I hope one day I would be able to give back to people at least that much I received from all of you.

TABLE OF CONTENTS

LIST OF TABLES

LIST OF FIGURES

INTRODUCTORY NOTES

Many tectonic and topographic features we see today on planetary surfaces are linked to the thermal history of the planet; therefore understanding thermal evolution of terrestrial planets is a key factor for understanding the differences in their tectonics. The Earth shares many common characteristics with its sister planets, Mars and especially Venus and at the beginning of their formation they probably started in a similar manner. What makes their latter evolution so different is still not well understood. In planetary science, many questions today stimulate the scientific curiosity. Why it is plate tectonics still active on Earth today but absent on any other planet? What is the effect of mantle volatilization on the stress state of lithosphere and on the craton stability? Is the atmosphere composition and climate on planets linked to its thermal evolution? This work is an attempt to bring a small contribution to the great endeavor to answer them. The essence of the work consist in a comprehensive investigation that tests the effect of volatile degassing-regassing on the mantle convection, the effect of convection on lithospheric stability, and the fate of volatiles in atmosphere and their role in planetary climate feedbacks. The ultimate objective of the study is to evaluate the coupled effect of volatile degassing and climate on the mantle thermal evolution.

The model will be applied for Earth-like planets that pose an active tectonic at surface and then the model is applied to a presumed Earth-size planet with inactive tectonics; more like present day condition of other terrestrial planets in our Solar System. The thermal history for these two cases will be investigated in chapter 1 and 2 respectively by running parameterized mantle convection models. The two tectonic styles, known in literature as thin lid and stagnant lid respectively, have each one a distinctive way to remove the internal heat,

and accordingly the methods to investigate them employ different parameterizations. The results of these numeric investigations are presented in chapter 1, for thin lid model, and chapter 2 for the stagnant lid. The focus of these studies will be the feedback plays between water-viscosity-temperature during thermal evolution as well as what factors affects the degassing-regassing process.

Thermal evolution of planetary mantle is in the direct connection with its convection intensity, and the viscosity induced deformation stress that act upon the lithosphere is ultimately controlled by convection. One condition for lithospheric stability is that the agents that cause tectonic deformation to be reduced. In this case, it is generally assumed that more vigorous mantle convection in the Earth's past would have made stability more difficult to achieve. Or it would have been easier? In chapter 3 we investigate the possible outcome of a decaying mantle convection intensity through time on the stability of continental lithosphere particularly to those parts that remained stable over the long geological time – cratons.

Volatiles affect the mantle convection directly through their feedback relationship with the viscosity and indirectly through their control on the melt formation. Nevertheless, things do not stop inside the planet. The outgassed volatiles once in the planet's atmospheric system interact with the radiative and convective processes and robustly decide the climate evolution path and surface temperature. Mantle convection is driven not only by its internal heat but also by the temperature difference between the interior and surface. The coupling of the climate system that closes the entire volatile cycle becomes obvious. In chapter 4 we used a one dimensional grey radiative-convective climate model to address some of the effects of volatiles, especially water, have in the climate system and the feedback mechanism of interest for the climate stability and determination of the planet's surface temperature.

TECHNICAL WORK

Chapter 1

THE EFFECTS OF VOLATILE CYCLING ON PLANETARY THERMAL EVOLUTION

Introduction

Parameterized, whole-mantle convection models have been used by several authors to study the thermal history of Earth and other terrestrial planets (Schubert 1978; Stevenson *et al.* 1983). The global tectonic evolution of a planet is related to its thermal evolution, and the tectonic features present on a planet's surface have been analyzed in relation with its thermal state. Early work by Tozer (1972) and Schubert *et al.* (1979) investigated the cooling histories of terrestrial planets using simplified analytical models of subsolidus mantle convection and assuming temperature-dependent viscosity. Further studies updated and developed this model by including the effect of volatiles, in particular water, on mantle viscosity (McGovern and Schubert 1989; Franck and Bounama 1995b). Volatiles in the mantle reduce its viscosity by lowering the activation energy for solid-state creep (Karato and Wu 1993). Thermal evolution models that considered the volatile effect on mantle viscosity have shown how it could lead to a more gradual cooling of the Earth over the geologic time and compared to models that did not consider volatile dependent rheology (McGovern and Schubert 1989).

Whole-mantle convection models coupled with volatile balance models show in general the viscosity value increasing with cooling of the system and increasing with the mantle becoming more depleted in water (McGovern and Schubert 1989; Franck and Bounama 1995a). However, since these early calculations our understanding of several key aspects within them has increased.

The effect of volatile concentration on mantle viscosity in the original study of McGovern and Schubert (1989) was based on two-point parameterization derived from some early experimental work (Chopra and Paterson 1984). A slightly more elaborate parameterization for mantle rheology was used by (Franck and Bounama 1995a). That model used a power-law dependence between the ratio of wet to dry olivine creep rates and water fugacity (Karato 1989). However, the wet value for olivine aggregate creep rate was still interpolated linearly from the two point function derived from the Chopra and Paterson (1984) model.

The degassing and regassing rate are the most important parameters that determine the amount of volatile present in both internal and external planetary reservoirs. There is no accurate understanding about how the Earth volatile cycle evolved through time, and it is even more difficult to understand the volatile exchange mechanisms of other planets like Venus and Mars. The degassing and regassing processes were quantified in terms of the areal spreading rate for Earth-like plate tectonics regime (McGovern and Schubert 1989). They scale also with the concentration of water in the mantle or the concentration of water in the subducting layer respectively.

In the present paper, we address the effect of volatile cycling on planetary thermal evolution using a mantle convection parameterization that corresponds to a planet with active plate tectonics. We develop models for the volatile degassing and regassing, and self consistently calculate the factors that affect the volatile flow rates among surface and internal planetary reservoirs. In addition to the work done by several authors mentioned above, we include several recent experimental and theoretical relations that had improved our

understanding about the system being simulated. In our model application we address water cycling only (although aspects of our approach could be adapted to other volatiles).

Numeric implementation of the planetary system model

Our model addresses the coupled effect of temperature and water concentration in the mantle on the heat flow out of the mantle. To achieve this we combined a planetary volatile (water) circulation model with a mantle convection model. The water circulation module solves a global mass balance equation that calculates the concentration of water in mantle and in a surface reservoir. Exchange between the mantle and surface reservoirs occurs by degassing due to melting and regassing associated with subduction. Degassing releases water into the atmosphere and hydrosphere (our surface reservoir) and depletes the mantle. Regassing recycles water back to the mantle. The degassing process is assumed to occur mostly at mid-ocean ridges and is controlled by the extent of a partial melting zone below the mid-ocean ridges and on the vigor of the convection as expressed in the areal plate spreading rate. The regassing process occurs at subduction zones and is calculated based on the variable thickness of a hydrated layer. The hydrated layer thickness is calculated based on the stability field for serpentine in the subducting lithosphere. Thermal evolution is simulated using a parameterized mantle convection algorithm that solves a globally averaged heat balance equation in one dimension. Heat is produced in the mantle by the radioactive decay of radiogenic elements. The heat flux exiting the mantle scales with Rayleigh number through a parameterization based on mantle convection experimental simulations (Olson and Corcos 1980; Kerr 1996; Schubert *et al.* 2001). The mantle viscosity is dependent on temperature and on the volatile concentration of the mantle (Kohlstedt 2006; Li *et al.* 2008). The mantle density is considered

constant with depth (Boussinesq approximation) and the viscosity varies with temperature and with the mass fraction of volatiles in mantle.

Volatile circulation

The general geological settings simulated by our model are analogues to the major features of an Earth-like planet that exhibits active plate tectonics. The exchange of volatiles between mantle and surface occurs along two major circuits: outgassing along mid-ocean ridges (MOR) and regassing along subduction zones (Fig. 1.1). A model that prescribes the content of volatiles in the mantle as a function of areal spreading rate for Earth's mid-ocean ridges is presented by (McGovern and Schubert 1989). The model balances the volatiles degassed at the mid-ocean ridges and the volatiles re-gassed along the subduction zones. The major improvements of our model consist of deriving the outgassing flow rate based on the water concentration in a partial melt channel below the MOR and the regassing flow rate based on a self consistently determined variable hydrated layer.

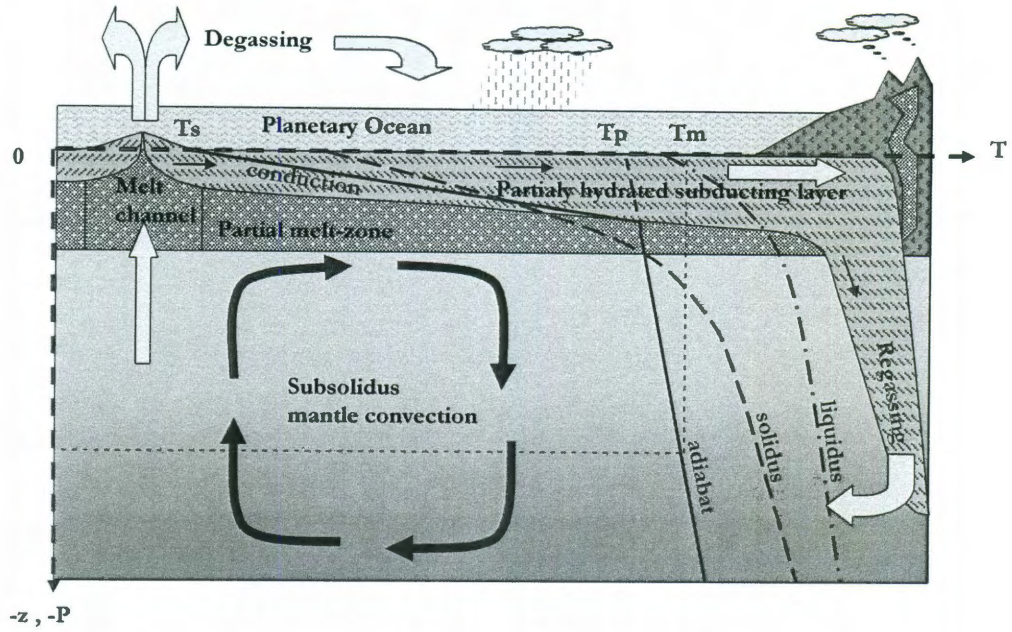

Figure 1.1. Schematic of the planetary volatile circulation system depicting main fluxes and reservoirs. The continuous line represents an average thermal profile through mantle. Dashed lines depicts the the solidus and liquidus lines as calculated by the melting module and used to derive melt-zone parameters. The average mantle temperature T_m is calculated from a parameterized model that considers the dependence of viscosity on the mantle temperature and water concentration, in mantle. Based on this temperature and water concentration the model calculates the partial melt-zone thickness and the amount of water in this zone from the intersection of the temperature profile with the solidus line and its relative position to the liquidus line. The thickness of the hydrated portion of the subducting layer is calculated based on the temperature profile and the stability field for serpentine.

At the MOR water is degassed from the mantle at a rate proportional to the volume of mantle that enters the partial melt channel below the ridge and to the amount of water within the melt channel. The melt channel volume depends on the spreading rate of the surface, which scales with convection velocity and on the depth over which partial melt occurs. The flow rate of water degassed at the mid-ocean ridges r_{MOR} is thus given by:

$$r_{MOR} \uparrow = \rho_m \cdot F_{melt} \cdot X_{melt} \cdot D_{melt} \cdot S \cdot \chi_d$$

where ρ_m is the mantle density, F_{melt} is the integrated melt fraction in the melt zone, X_{melt} is weight fraction of volatiles in the melt, D_{melt} is the thickness of the melt zone under the mid ocean ridges, S is areal spreading rate, and χ_d is degassing factor. The amount of water in melt as well as the melt zone thickness is calculated in a separate module and that is described in more detail later.

Volatiles are recycled back into the mantle at subduction zones. The flux of water depends on the thickness of a serpentinized layer and of a thin sedimentary layer (Rupke *et al.* 2004). These layers transport chemically bound water back into the mantle. Although the sedimentary layer carries a significant amount of water along the subduction zone, it is believed to release this water near the surface early in the subduction process and does not contribute significantly to the re-hydration of deeper mantle. It is estimated that up to 85% of the water that enters the subduction zone escapes via arc volcanism processes (Schmidt and Poli 1998). Hydration of the subducting slab takes place during plate bending and water percolates into upper crustal layers through normal faults in lithosphere. Water reacts with the olivine in the mantle and produces serpentine, the thickness of this hydrated layer thus covers the thermodynamic stability field of serpentinite. We calculate the regassing flux into the mantle by scaling the thickness of a hydrated layer with the average spreading (subducting) rate derived from the convection velocity. The hydrated layer is represented by the serpentinized portion of the lithospheric mantle. Assuming decomposition of the hydrous phase occurs at about 3 GPa, we set the stability temperature limit at 700°C (Ulmer and Trommsdorff 1995). The hydrated layer thickness is then calculated as a depth to this isotherm on the temperature profile of the thermal boundary layer. Thus, at subduction zones, the rate of volatiles recycled back to the mantle r_{SUB} is:

$$r_{SUB} \downarrow = f_h \cdot \rho \cdot D_{hydr} \cdot S \cdot \chi_r$$

where f_h is mass fraction of volatiles in the hydrated layer, ρ is upper mantle density, D_{hydr} is the average hydrated layer thickness, χ_r is the regassing factor efficiency.

The spreading rate (S) as a function of time is derived from the convection velocity evolution assuming a constant length of mid-ocean ridges and subduction zones. The convection velocity (spreading and subduction velocity) is derived from boundary layer theory (Schubert *et al.* 2001):

$$S = L \cdot u$$

where L is the length of mid-ocean ridges considered constant over time, and u is the convection velocity. The rate balance then becomes:

$$r_{Mmv} = r_{SUB} \downarrow - r_{MOR} \uparrow$$

The absolute rate r_{Mmv} represents the overall flow rate of water in the mantle; it is negative when mantle loses more water than is recycled back and is positive otherwise. This flow rate is then integrated in time and the value of this integral at any time represents the amount of water in the mantle. The difference is assumed to represent the water in surface reservoir.

Mantle convection

The fundamentals of mantle convection parameterization and its relationship with mantle thermal evolution has been developed and described in much detail earlier (Tozer 1972;

Schubert 1978; Schubert *et al.* 1980). Assuming spherical geometry the model is based on solving an energy conservation equation in a one-dimensional mantle domain:

$$\rho_m \cdot c_m \cdot (R_m^3 - R_c^3)\frac{dT_m}{dt} = -3 \cdot R_m^2 \cdot q_m + Q(t) \cdot (R_m^3 - R_c^3)$$

where ρ_m is the mantle density, c_m is the mantle heat capacity, T_m is the mantle temperature, t is time, T_s is the surface temperature, R_c is the core radius, R_m is the mantle radius, and q_m is the mantle heat flow. Heat Q is produced by the decay of radiogenic elements in the mantle, which is assumed to be the only source of heat in the system. The fundamental concept is that the mantle temperature is considered its integrated value over the volume of the mantle and thus is represented by an average temperature at the midpoint of the mantle thickness. While this is a satisfactory assumption for the mantle convection algorithm an adiabatic profile starting from this point was required and calculated in order to estimate the melt zone parameters further in this chapter.

Heat flux q_m from the mantle is defined using a relationship between Nusselt number Nu and the thermal Rayleigh number Ra:

$$Nu = \frac{q_m}{k\frac{\Delta T}{Z}} = a \cdot \left(\frac{Ra}{Ra_{cr}}\right)^{\beta}$$

where k is the mantle thermal conductivity, ΔT is the temperature difference between mantle and surface (T_m-T_s), Z is the convection cell scale taken as the mantle thickness, Ra_{cr} is the critical Rayleigh number, a is the scaling constant, and β is the scaling exponent.

Outgassing and regassing of water are determined from a model based on the areal spreading rate. We derive the spreading rate from boundary layer theory. First, we estimate the lithosphere thickness from Fourier's law:

$$D_b = k\frac{(T_b - T_s)}{q}$$

The value of temperature at the bottom of the lithosphere T_b is considered equal to T_m (isothermal mantle) in the scaling theory of mantle convection. However, in the melt-zone calculation module, the adiabatic mantle temperature profile requires that T_b is different than T_m and consequently we assigned a constant value set to a predefined isotherm similar to the approach used by (Schubert *et al.* 1979). The age of subduction is calculated as (Schubert *et al.* 2001):

$$t_s = 2\frac{(k\cdot(T_b - T_s))^2}{q^2\cdot\pi\cdot\kappa}$$

The convection velocity is:

$$u_c = \frac{(R_m - R_c)}{t_s}$$

Areal spreading rate is then scaled with velocity assuming a constant total length of the MOR system over time and using this length as a scaling constant:

$$S = 2 * u_c \cdot L_{ridge}$$

The factor of *2* was applied in order to accommodate the symmetry of the spreading as well as of subduction that take place in both directions.

Water concentration dependent viscosity

Early deformation experiments on dunite and peridotite samples showed that olivine-rich rocks deform more easily when water concentration is higher (Carter and Ave'Lallemant 1970; Chopra and Paterson 1984). Further experiments on olivine single crystals treated in hydrous and anhydrous environments proved that these crystals deform at a reduced strain rate when samples have higher water content (Mackwell *et al.* 1985). The results of the deformation experiments were statistically modeled by a power law equation that relates the strain rate to temperature and scaled by an exponential value of the stress and by the creep state activation energy (Chopra and Paterson 1984; Karato and Wu 1993). The power law was further developed to include the dependence of strain rate on the fugacity of water in olivine (Hirth and Kohlstedt 1996; Mei and Kohlstedt 2000).

$$\frac{\partial \varepsilon}{\partial t} = A_{cre} \tau^{n} \ln f_{H_2O}^{r} \cdot \exp\left(-\frac{Q_a}{RT}\right)$$

where $\partial\varepsilon/\partial t$ is the shear strain rate, A_{cre} and r are empirical constants, τ is shear stress, n is the stress exponent, Q_a is the activation energy for the dislocation creep regime, T is temperature and R is the universal gas constant.

We assign a Newtonian behavior for the mantle material, and hence a linear dependence of strain rate on stress (n=1) for simplicity. In order to eliminate fugacity from our calculations we implement an empirical logarithmic relation that expresses the fugacity in terms of water concentration (Li *et al.* 2008):

$$\ln f_{H_2O} = c_0 + c_1 \ln C_{OH} + c_2 \ln^2 C_{OH} + c_3 \ln^3 C_{OH}$$

where f_{H2O} is water fugacity in MPa, c_0 = -7.98, c_1 = 4.35, c_2 = -0.57, c_3 = 0.03 are experimentally determined constants by (Li *et al.* 2008), and C_{OH} is water concentration expressed in atomic H/10^6 Si. Mineral ratio Fe_2SiO_4/Mg_2SiO_4 in the olivine composition was considered 1/9. The flow law is:

$$\frac{\partial \varepsilon}{\partial t} = A_{cre} \tau \ln f_{H_2O}^r \cdot \exp\left(-\frac{Q_a}{RT}\right)$$

where $\partial\varepsilon/\partial t$ is the shear strain rate, A_{cre} and r are experimental constants, τ is shear stress, Q_a is the activation energy for the dislocation creep regime, T is temperature and R is the universal gas constant. The effective viscosity thus becomes:

$$\eta_{eff} = \frac{\tau}{\dot{\varepsilon}} = \eta_0 \cdot A_{cre}^{-1} \left(\exp\left(c_0 + c_1 \ln C_{OH} + c_2 \ln^2 C_{OH} + c_3 \ln^3 C_{OH}\right)\right)^{-r} \cdot \exp\left(\frac{Q_a}{RT}\right)$$

This equation is represented in Fig. 1.2 along with the two parameterizations of (Chopra and Paterson 1984).

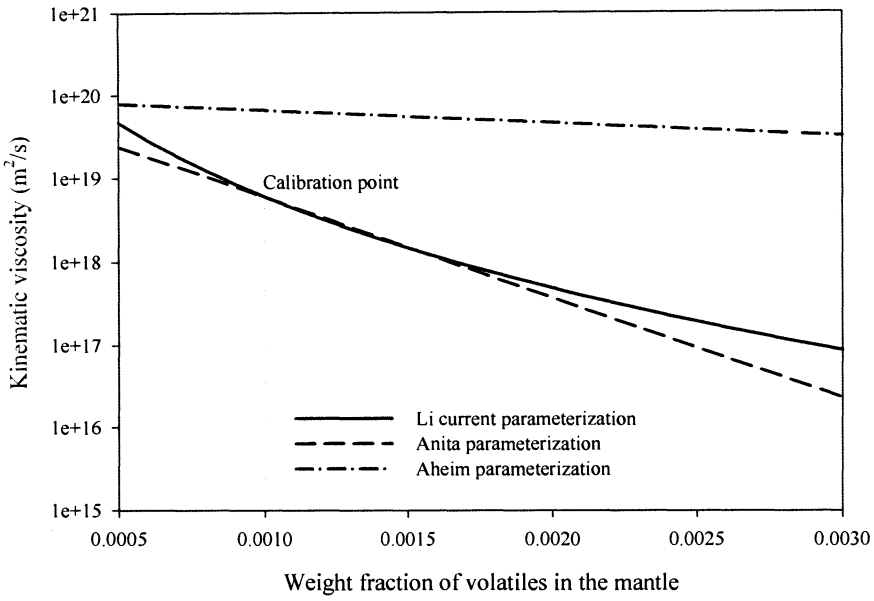

Figure 1.2. Viscosity function of water concentration for different parameterizations calculated at 2200 K.

Melt-zone calculation

Computation of the melt-zone thickness and water concentration in the melt extract was based on a model that considers the effect of water on the melting, particularly on the shift of the solidus and liquidus profiles for the mantle peridotite as a result of hydrous melting (Katz *et al.* 2003). In the melting process, water was considered a trace element and the partition between the solid phase and partial melt extracted was approximated using a constant bulk distribution coefficient D_{H2O} of 0.01. The partition is then estimated from:

$$X_{melt} = \frac{C_{mv}}{D_{H_2O} + F_{melt}(1 - D_{H_2O})}$$

where C_{mv} is the bulk water composition in the solid mantle phase expressed as weight fraction, and F_{melt} is the degree of melting expressed as melt fraction. Since we average the melt

fraction over a large depth interval it is safe to assume that the process is equivalent to equilibrium batch melting and the clinopyroxene phase is never exhausted. These assumptions are required to assure continuity for the solidus and liquidus functions. The water behaves as an incompatible element and segregates from the solid mantle. Therefore, the estimated outgassed flux based on water concentration in the melt is slightly higher than the one based on bulk mantle concentration alone with effects that we will investigate further. Melt fraction is represented by a function that depends on solidus and liquidus temperature at any depth or pressure. The dependence for anhydrous melting is expressed by a second order polynomial function as suggested by Hirschmann (2000). This function is extended to hydrous melting by adding a dissolved water component that decreases the solidus and liquidus temperatures respectively:

$$T_{sol-hydr} = T_{sol-dry} - \Delta T_{H_2O}$$
$$T_{liq-hydr} = T_{liq-dry} - \Delta T_{H_2O}$$

where $T_{sol\text{-}hydr}$, $T_{liq\text{-}hydr}$, $T_{sol\text{-}dry}$ and $T_{liq\text{-}hydr}$ are the hydrous solidus, liquidus and dry solidus and liquidus temperatures respectively, and ΔT_{H2O} is the temperature shift of the dry curves as a result of hydrous melting. The temperature shift scales with water concentration in the melt according to the empirical formula:

$$\Delta T_{H_2O} = K \cdot X_{melt}^{\gamma}$$

The K and γ are calibration constants and the values were obtained by Katz *et al.* (2003). The above equations were used assuming bulk water concentration in the mantle below saturation level. However, this could be tested against the experimental work performed by

Kawamoto and Holloway (1997) to ensure the model runs below saturation at any time. Melt fraction is then parameterized in the form of power law:

$$F_{melt} = \left[\frac{T - \left(T_{sol-dry} - \Delta T_{H_2O}(X_{melt})\right)}{T_{liq-dry} - T_{sol-dry}} \right]^{\beta}$$

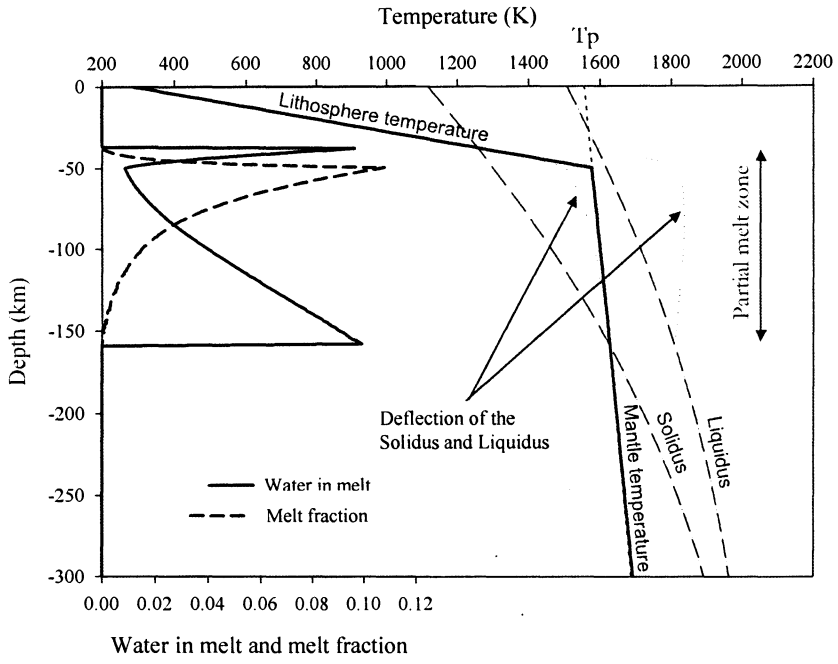

Figure 1.3. General thermal profile through mantle and the parameters for melt-zone calculation. The melt-zone thickness is located between the points where the average temperature profile crosses the solidus line. The melt fraction in the zone is calculated based on the proximity of the point on the thermal profile to the variable solidus and liquidus lines and then integrating over the entire zone.

The melt fraction and the water content of the mantle are calculated along a profile from surface to depth up to 300 km (Fig. 1.3). This value was chosen to reflect the maximum depth for which the melting model was constrained by observation and laboratory

experiments. The melt fraction and water concentration in the melt extract profiles were integrated over depth to obtain average values used in the volatile budget calculation.

The calculation of the thickness of melt zone involves determination of the upper and lower boundary of the melt zones for an average thermal profile in the mantle. They are determined by calculating the depth where the thermal profile crosses the solidus line and the difference is interpreted as average melt-zone thickness. The standard thermal profile consists of two parts: the conductive profile through lithosphere and the mantle adiabat. The temperature on the thermal profile is compared with the solidus and liquidus temperatures at any depth in order to determine the melt fraction and the water concentration in the melt. The crossing points between thermal profile and the solidus line are located and the distance between them are assigned to the melt zone thickness. The conductive profile is determined in the lithosphere from:

$$T(z)\big|_{z\le D_{bl}} = T_s + z \cdot \frac{q_m}{k}$$

On the adiabat, the temperature is determined according to McKenzie and Bickle (1988):

$$T(z)\big|_{z>D_{bl}} = T_p + z \cdot \frac{g \cdot \alpha \cdot T_m}{c_p}$$

Since the mantle temperature T_m is averaged for the whole mantle thickness, the adiabat is approximated to a line of slope g/cp that intercepts the mid-distance of the mantle interval at mantle temperature T_m and the surface at potential temperature T_p.

Comparative analysis of the volatile cycling models

The current model output was compared to a set of previous models and the differences are presented in Fig. 1.4. The initial amount of radiogenic heat and the initial amount of water in mantle were identical for all runs. The six runs numbered from Case 1 to Case 6 correspond to models described in Table 1.1.

Case no	*Description*	*Reference*
Case 1	Classic model, no water effect	Schubert (1980)
Case 2	Anita Bay parameterization	McGovern (1989)
Case 3	Anheim parameterization	McGovern (1989)
Case 4	Li parameterization	Li (2008)
Case 5	Melt controlled degassing	Katz (2003)
Case 6	Hydrated layer controlled regassing	Rupke (2004)

Table 1.1. Comparative test runs indicating the parameterization settings.

A nominal case (Case 1) was run as a reference model. The reference case is based on now classic parameterization of mantle convection (Schubert *et al.* 1980) that does not include a dependence of viscosity on volatile content (the equivalent initial viscosity for this case was set to equivalent of Anita Bay parameterization for 1000 ppm). The set of parameters used are presented in Table 1.2. In the next case, we added the effect of volatile dependent viscosity by coupling the volatile and melting modules with the initial mantle convection module.

The parameters that define the volatile dependent characteristics of the model are presented in Table 1.3. All models were run for 4.6 Ga.

Parameter	*Value*	*Unit*
T_s	300	K
Q(0)	4.51	$J/(m^3*y)$
R_m	6271	km
R_c	3471	km
ρ_m	3000	Kg/m^3
k_m	4.2	W/(m*K)
cp	1400	J/(kg*K)
α	$3.00*10^{-5}$	K^{-1}
β	0.33	-
λ	$3.4*10^{-10}$	y^{-1}
Ra_{cr}	1100	-
ν	$4*10^{17}$	m^2/s

Table 1.2. Mantle convection parameters.

Parameter	*Value*	*Unit*
η_0	$1.7*10^{17}$	Pa*s
Acre	90	MPa^{-r}/s
r	1.2	-
Ae_c	$4.8*10^5$	J/mol
X_d	0.02	-
X_r	0.03	-
OM	$1.39*10^{21}$	kg

Table 1.3. Parameters for volatile cycling module.

Cases 2 and 3 represent the result of the simulation using the McGovern and Schubert (1989) model with the viscosity laws given by Anita Bay and Anheim parameterizations

respectively. They correspond to case 1 and 2 in McGovern and Schubert (1989). In Case 4 we introduced the viscosity calculated using the Li *et al.* (2008) updated formula. The viscosity functions for volatile independent, Anita, Anheim and Li parameterizations were each calibrated for $6 \cdot 10^{18}$ m^2/s at 2200 K and 1000 ppm volatile fraction (Fig. 1.2). Case 5 was run replacing the constant melt-zone thickness and mantle bulk concentration dependent degassing terms in McGovern and Schubert (1989) formulation with the more complex parameterization based on the variable partial melting model and melt water dependent degassing (Katz *et al.* 2003). Case 6 was run introducing the variable thickness serpentinized – hydrated layer in the regassing module. Cases 5 and 6 also introduced the areal spreading rate calculated from derived convective velocity.

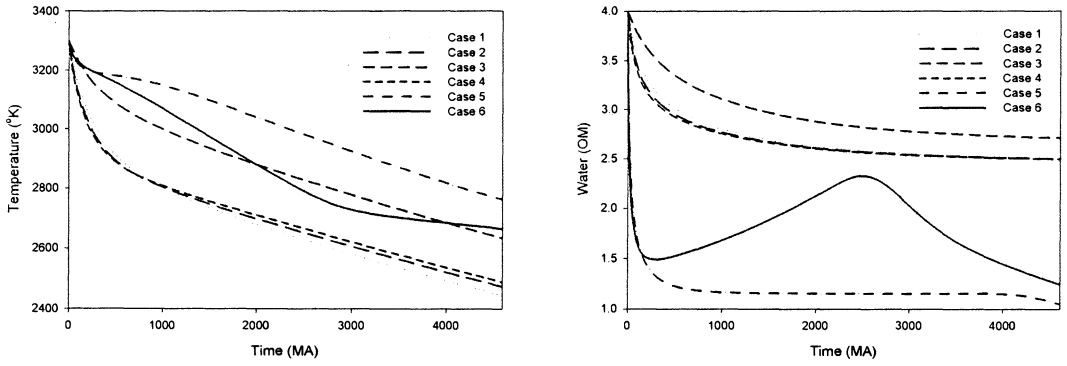

a) *b)*

Figure 1.4. Results of the comparative parameterization study for: a) Mantle temperature evolution, and b) Water in mantle evolution. Case 1 represents classic parameterization that does not involve volatile cycling and no dependence on the viscosity on the water concentration. Cases 2 and 3 have the viscosity depend on water concentration according to Anita Bay and Aheim models respectively and the volatile flow rates scales with constant degassing and regassing layers. Case 4 introduces the Li parameterization for water dependent viscosity but the flow rate scaling is the same as in previous two cases. In case 5 the melt dependent outgassing model is introduced and case 6 represents the full model implementation including the variable thickness regassing rate calculation.

The results of the comparative runs for mantle temperature and the amount of water in mantle evolution are presented in Fig. 1.4. In case 1 mantle temperature reaches the lowest level as the viscosity is unaffected by the volatile evolution. The fact that volatile cycling is absent in this case is equivalent to evolution with constant amount of water in the mantle. The rest of the cases allow for variable levels of devolatilization that removes water from the mantle, which increases viscosity. Cases 2 and 4 display about the same level for both the temperature and water content with case 4 producing the most degassing and the highest temperature. Case 3 displays an interesting evolution: although this model produces the wettest condition for the mantle and one would expect the temperature to be lower, instead it exhibits the highest temperature. This behavior is the consequence of the Aheim viscosity parameterization that is less dependent on water concentration compared with any other model. As a result, the Aheim function requires much higher water concentration to attain the same viscosity as the Anita and Li parameterization. Compared with cases 2 and 4 although mantle is wetter in case 3, the viscosity is still higher due to its response function and this raises the temperature compared with the other cases analyzed. Case 5 is the driest situation and as expected, it displays the highest temperature. The case is so dry since at this step the model allows for a very efficient outgassing that results from melting but also maintains an inefficient regassing due to the assumption of a constant thickness hydrated layer and due to the dependence of spreading rate on convective vigor (Fig. 1.5). The method used to track the spreading rate is to compute an average convective velocity and to assume a constant length of spreading and of subduction zone. This eventually led to higher areal spreading and bigger degassing rates (Fig 1.5). The mantle thus becomes dry and evolves at an elevated temperature. Case 6 brings together our entire model and shows three stages of evolution. A rapid degassing depletes the mantle in volatile in the first 300 MA of evolution, as this stage is associated with a

thick total melt zone and high areal spreading rate. The mantle becomes dry and the degassing rate is reduced. An absolute overall regassing phase follows in the next about 2500 MA as the melt zone thickness decreases and the hydrated layer grows along with the decrease in temperature. This allows the mantle to regain water until the total flow rate changes its direction again and the mantle starts an overall degassing phase. The trend in this final stage is determined by the development of a partially melted zone in the upper mantle that contains a larger concentration of volatiles (i.e. water). Thus, the mantle becomes drier and the temperature path adjusts itself evolving at significantly reduced cooling rate as more heat is built up.

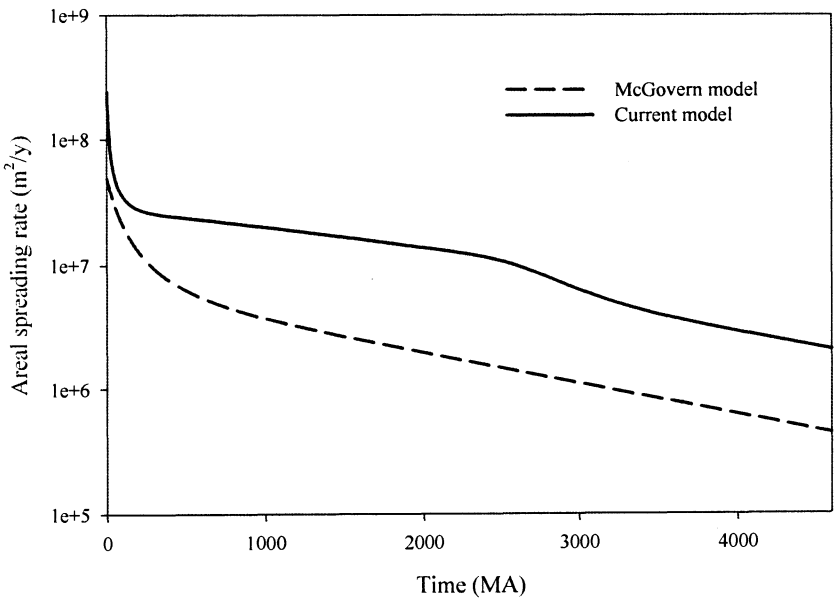

Figure 1.5. Areal spreading rate calculated according to the McGovern (1989) model and current model respectively. The current calculation yields higher average spreading rates and as a result, it tends to outgas the volatiles in the mantle faster.

The comparative analysis of the six cases points to the conclusion that our updated model yields higher flow rates and cycles more water than previous models (McGovern and Schubert 1989).

Constraining model and free parameters

Heat flux out of the mantle was set to the present Earth average value of ~70 mW/m^2. By calibrating the reference model to output that value, we could set the initial amount of heat produced by the radioactive elements (see Table 1.1). The potential temperature of the shallow mantle has been constrained by some authors using a calculation based on the heat flux and the dependence of conductivity on temperature measurements (McKenzie *et al.* 2005), or based on petrological aspects of average basalt composition (McKenzie and Bickle 1988). The values found by most authors agree around 1400 K. Starting from this value and extrapolating along the mantle adiabat, we find an estimated value of 2400 K for the present day integrated mantle temperature.

The value of mantle viscosity and its variation according to temperature and concentration of volatiles largely determines the thermal state and the evolution of mantle convection inside Earth. This function was parameterized according to results of experiments on olivine deformation (Li *et al.* 2008). We always assume an olivine-rich mantle. The estimated value of mantle viscosity was tested by running a present day convection model for the predefined assumed mantle temperature. Using a scaling factor for convection of 0.33 (Schubert 1978; Olson and Corcos 1980), and the rest of parameters from Table 1.1 we obtain an average value of $2.4*10^{21}$ Pa*s. This value is in good agreement with the viscosity range $4*10^{20}$ - 10^{23} derived by other authors using a joint convection inversion and glacial isostatic adjustment analysis (Mitrovica and Forte 2004).

The next step is to calibrate the viscosity for the volatile content at a predefined temperature. Unfortunately the amount of water and its distribution within the mantle is poorly constrained, value ranging from 40-1000 ppm (Thompson 1992), 50-200 ppm (Hirschmann 2006), minimum 700 ppm (Bolfan-Casanova 2007). For a reference, an average of 500 ppm was used for calibration of mantle viscosity at 2300 K temperature. We note that the volume of water in the mantle varies in our models and the range of values that lead to successful models is something we seek to constrain.

Temperature evolution

We analyze here the evolution of three initial scenarios, each with three different initial amounts of volatiles in the mantle. We used 2 OM (1 OM = the water amount equivalent to the Earth ocean mass), 4 OM, and 6 OM, to test the effect of initial volatile content on thermal evolution. The outputs of these simulations are presented in Fig. 1.6, along with the reference nonvolatile-dependent case. These results show a relative decrease in temperature over time and are in general agreement with the previous results that highlight the effect of temperature and volatile dependent viscosity on thermal evolution. Mantle temperature is controlled by the balance of heat in the system in time. The surface heat flow is controlled by the viscosity dependent convection and the feedback loop closes as temperature determines the viscosity. The convection intensity in terms of Ra, the heat flux and the convective velocity (Fig. 1.7 a,b,c) are not directly dependent on the amount of volatile in the mantle except for the initial stage. The system tends to self regulate these variables by adjusting the temperature and, as we will demonstrate further, the water concentration. However, coupling the volatile dependent model produces an added effect (Fig 1.7). Because of the coupling of the two negative feedback loops (temperature and volatile content dependent viscosity), the thermal

evolution in cases allowing water cycling is much better regulated than in the case of temperature feedback loop only. While temperature depends on the convection intensity and on the radiogenic heat-source concentration, the amount of water in the mantle is controlled by the degassing-regassing system that also depends on convection intensity and additional processes that are not as related to convection (i.e. depth of serpentinization, degree of partial melting).

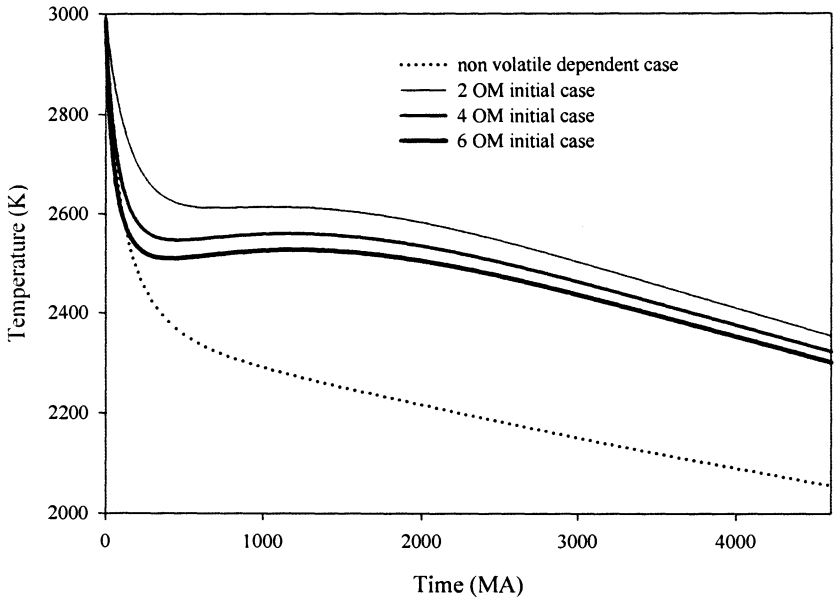

Figure 1.6. Mantle temperature evolution for different initial amounts of water in the mantle and with water cycling in the system compared with the non volatile-dependent case. The non volatile-dependent case runs with a constant 4 OM amount of water throughout the entire evolution. The volatile effect is characterized by enhanced temperature due the relative devolatilization early in evolution and by the sinuousness of the evolution path.

For the cases analyzed, the rapid cooling at the beginning results from intense convection and surface heat loss (Fig. 1.7a) that raises the mantle viscosity (Fig. 1.7d) which in turn slows convection. In the same time, the high value for the convective parameters (like

convective velocity – Fig. 1.7c) produces a very efficient outgassing, which further raises the viscosity (Fig. 1.7b).

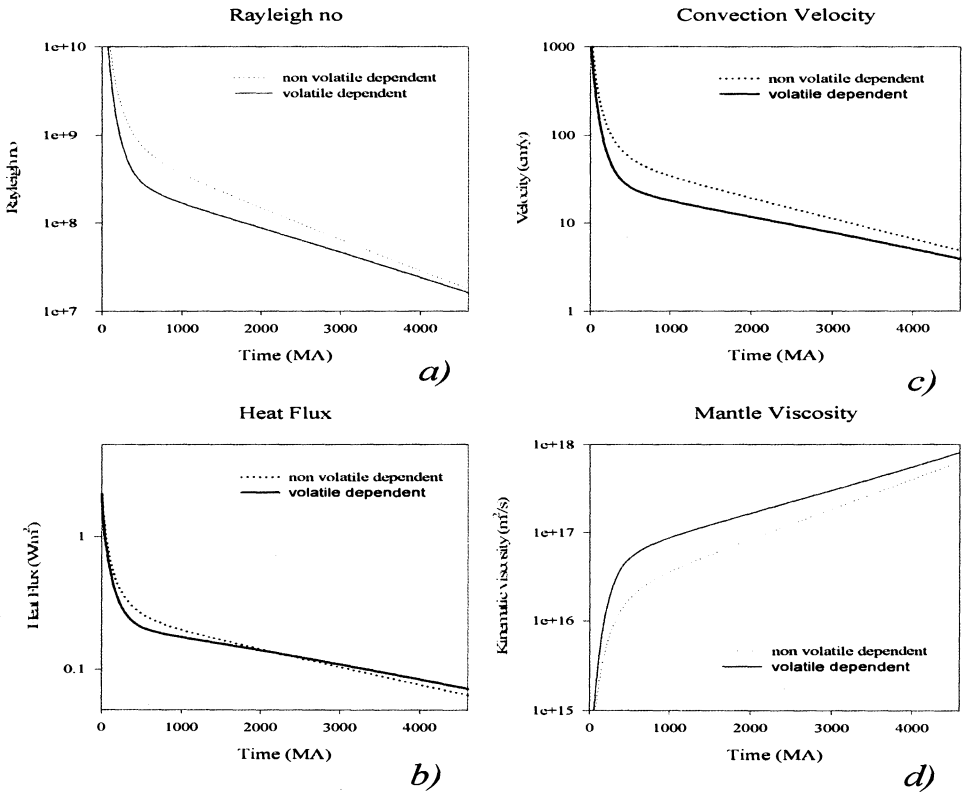

Figure 1.7. Convection parameters evolution. Ra a), heat flux b), convection velocity c) and viscosity d) for a convecting mantle with a coupled volatile cycle system (continuous line) and for the classic uncoupled case (dotted line). These parameters derived from parameterization scaling does not depend greatly on the initial temperature or initial amount of water in mantle but show the importance of the volatile coupling.

The viscosity dependence on the two factors affects the energy flux in the system and produces a relative imbalance of heat that shows as relative high initial Urey ratio (values near 1 on Fig. 1.8). The Urey ratio is defined as the ratio of the heat produced in the system by the radioactive elements to the heat that flows out of the mantle. As the system evolves, the

temperature rebounds and follows its normal trend due to the negative feedbacks of the temperature-viscosity and volatile-viscosity relationships.

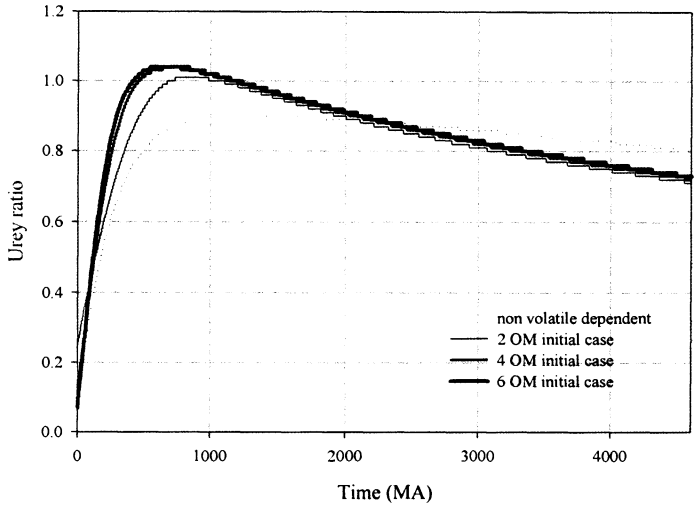

Figure 1.8. Urey ratio evolution for different parameterizations. The volatile dependent parameterization experience a high degassing rate at the beginning of evolution relatively to constant nonvolatile dependent parameterization. This dries out the mantle, increase viscosity, and reduces the heat flow. The condition is characterized by the high Urey ratio during early evolution. Later, the mantle regains some water back through regassing and the enhanced heat flow lower the Urey ratio. During thermal evolution, the increasing level of volatilization tends to raise the Urey ratio slightly but the final value is not significantly affected by the initial amount of volatiles in the mantle.

The three cases analyzed differ in their evolution by displaying a mantle that evolves at different temperature levels. The richer the mantle is in volatiles the colder is its evolution path. The final trends tend to converge to roughly the same temperature as drier mantle run at higher temperature and this makes outgassing less efficient.

Degassing and regassing processes

The magnitude of outgassing and regassing processes is tied to the mantle convection vigor. This connection provides the link for a feedback process to act. As the mantle cools over time, the melt zone thickness shrinks, and the subducted hydrated layer thickens along with the thermal boundary layer (Fig. 1.9). This trend is maintained independent of the initial content of water in the system with only minor differences among runs.

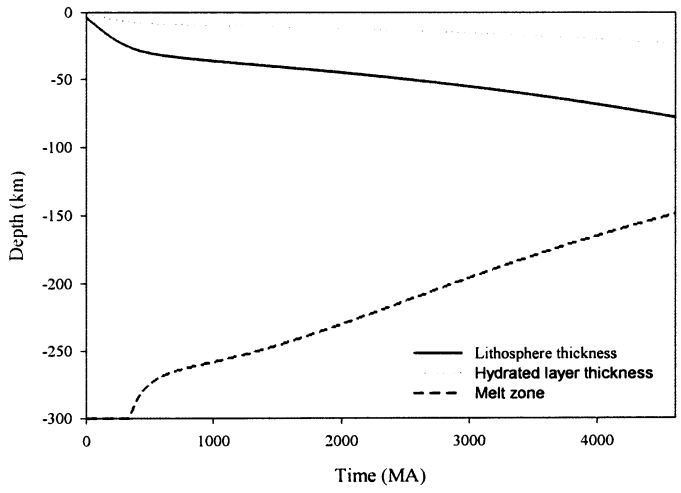

Figure 1.9. Elements of the depth profile evolution including the lithosphere thickness, the melt zone depth and the serpentinized layer thickness. As the mantle cools the melt-zone shrinks and the hydrated layer grows along with the lithosphere thickness. These trends have important implications for the dynamics of the degassed and regassed water fluxes.

As a result, outgassing is predominant early in the thermal evolution and then slowly diminishes with the regassing process gaining efficiency in the later phase when the mantle becomes progressively cooler. Naturally, the balance of volatiles in the mantle reaches a minimum at some point, defined as the tipping point, and then starts increasing with more

water coming into the mantle than leaving it (Fig. 1.10). The position of the tipping point can shift in time depending on the efficiency constants used in volatile cycling module.

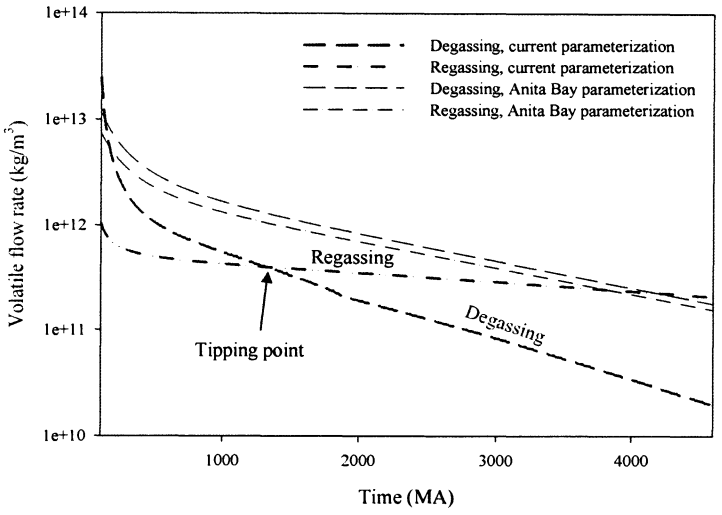

Figure 1.10. Degassing and regassing flow rate evolution for different parameterizations. At some point during evolution, the regassing rate exceeds the degassing and the system switches to overall regassing. We define this moment in time as the tipping point.

The results of variable water content depict a strong negative feedback between volatile content of the mantle and its thermal evolution. The fact that temperature tends to become uniform in time regardless of the amount of initial water reveals this feedback mechanism. Looking at the evolution of the melt-zone thickness and of the thickness of hydrated layer it is expected that a mantle with lower content of water will evolve at higher temperature (case 1 for example) will develop a deeper, melt-zone and will sustain an increased level of outgassing. In the same time, for the regassing process, a hot and dry mantle will develop a thicker boundary layer and as a result, the stability field for serpentine (isotherm) is found at greater depth, which means a larger degree of regassing. This gain therefore tends to

offset the outgassing. This observation, along with the fact that the differences among runs are small, points out that the feedback mechanism cannot be explained based on thickness alone. A more detailed view into the problem can be attained if we plot the thermal evolution of the three cases over the response spectrum of the melting model (Fig. 1.11). We computed the response spectrum by multiplying the amount of water in the partial melt zone with the thickness of the melt zone for an average thermal profile. The outgassed flux depends on the amount of water in the melt and the amount of melt in the melt zone, which varies with the temperature and the bulk composition of water in the mantle.

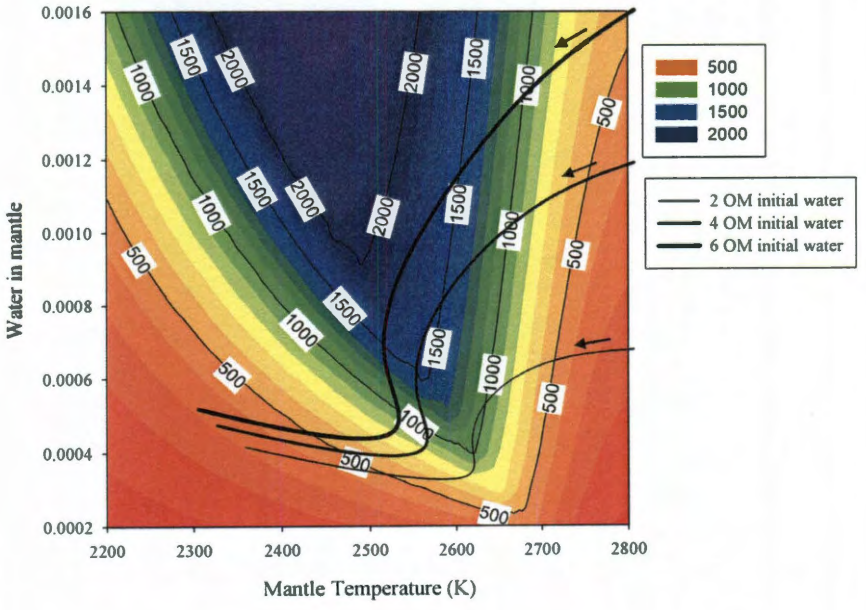

Figure 1.11. Degassing potential spectrum and the evolution of water in mantle vs mantle temperature for three initial conditions. The degassing potential spectrum represents kg of water potentially degassed per kg of mantle per year times the thickness in m of the melt zone. The arrows indicate the direction of evolution of the system in time.

Plots of thermal evolution in temperature – water concentration coordinates illustrate that the mantle with low volatile concentration evolves in the lower end of the spectrum that yield the least amount of outgassing. On the opposite side, the mantle rich in water passes through the higher end of the spectrum and suffers a higher grade of degassing. The net result is that the mantle that starts wet tends to degas more rapidly than if it starts dry, it maintains a lower temperature and the general trend is that the bulk composition of the water in mantle tend to reach the similar levels (Fig. 1.12).

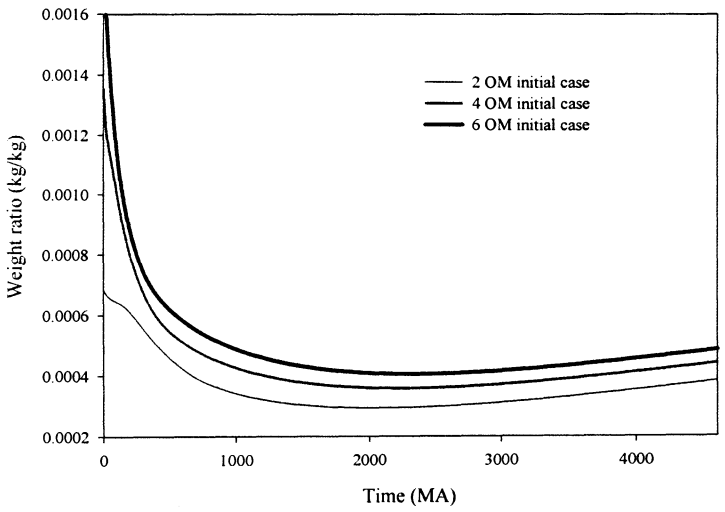

Figure 1.12. Evolution of the water concentration in the mantle for different initial conditions. The strong negative feedback between the volatiles and convection on a mantle with volatile dependent viscosity regulates the amount of water in the mantle reservoir.

This feedback mechanism between volatile content and viscosity is similar to that between temperature and viscosity. Although the feedback is controlled mainly by the outgassing and the melt zone evolution, regassing still plays an important role. It keeps the mantle from being dehydrated, thus reinforcing the feedback mechanism. This is significant

for comparative planetary evolution studies since both pathways of water circulation assume unconditional availability of water to circulate. We have assumed to this point that the surface reservoirs do not become completely consumed. In some cases, water may be lost at the surface due to high atmospheric temperature (like Venus climate) or can be trapped as ice on the continents (like in the case of Mars). Situations like these may lead to imbalances in the convection mechanism that could lead to first order changes in dynamics of a planet.

Efficiency factors analysis

The magnitude of the outgassed and regassed fluxes and the evolution of the water in the mantle represent critical factors that influence the outcome of any simulation performed with volatile dependent parameterization turned on. Among other factors that affect these variables, the efficiency parameters used within the volatile cycle can potentially change the results over a broad range but are largely difficult to constrain directly from data.

We employed our numerical approach to calculate various evolution scenarios with the purpose of constraining a range for the efficiency factors based on models that could mach present day observations. A matrix of different parameter sets were modeled with the efficiency constants sampled at equal intervals between 0.001 and 0.1 for both the degassing and regassing part of the cycle. Final spectrums were calculated by plotting present day values for different parameters obtained at the end of each run on and displayed on a χ_d versus χ_r scale (Fig. 1.13). The model used the same parameterization as presented in tables 1 and 2, with 4 OM initial water in the mantle. By cross correlating these spectrums and intersecting those areas where valid results are obtained we constrained the efficiency factors within a narrow range.

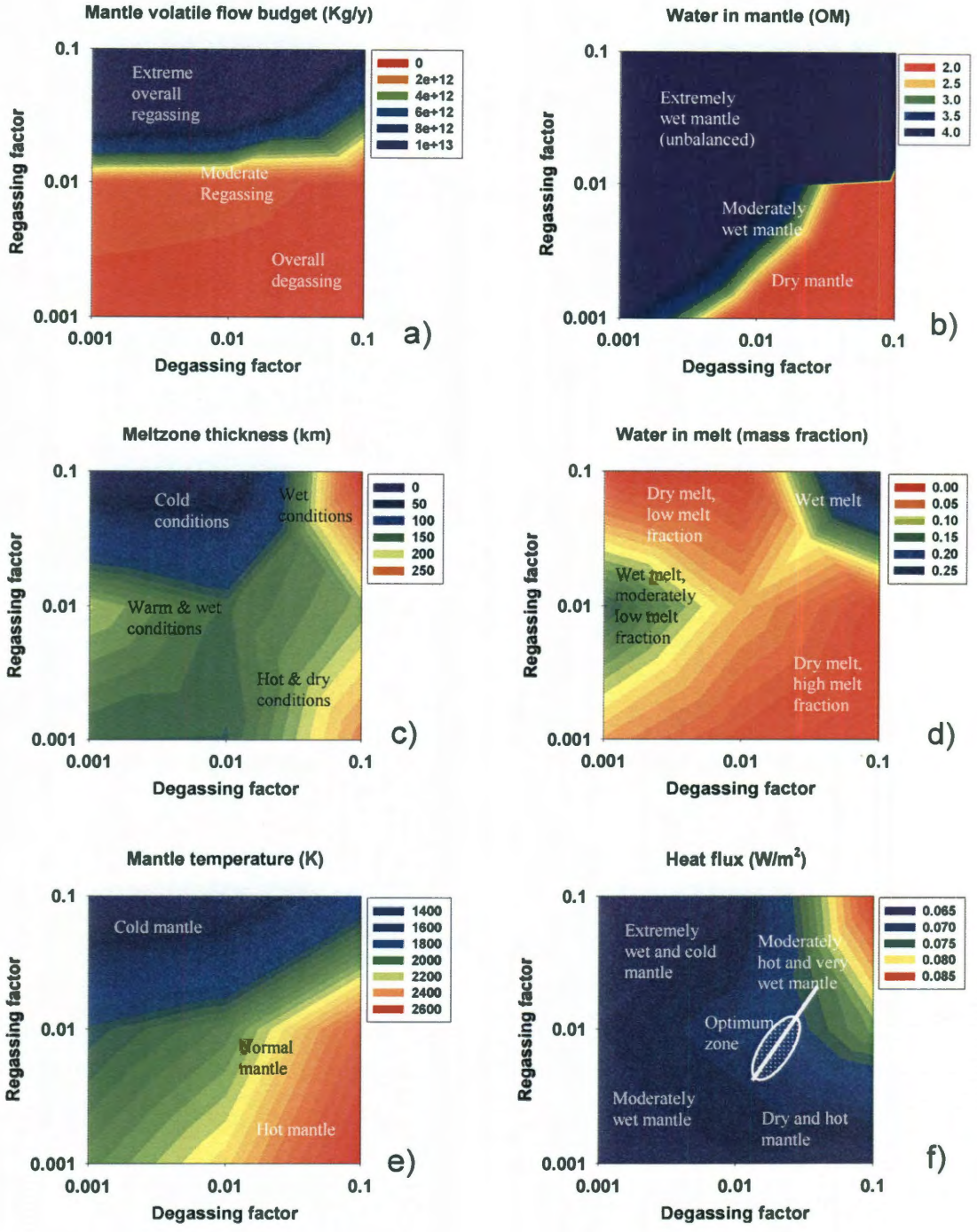

Figure 1.13. Results of the efficiency factor analysis at the end of the run. a) Mantle volatile flow budget. b) Water in mantle. c) Melt zone thickness d) Water in melt. e) Mantle temperature. f) Heat flux.

The first thing that we consider is the difference between degassing and regassing parameterizations. This is illustrated by the spectrum of balanced mantle volatile flow (Fig. 1.13a). It exhibits disequilibrium toward the regassing process. For the same value of efficiency constants there is more water coming into the mantle than water outgassed. However, this does not mean that the regassing process is more effective through the entire run time since the spectrum only represents the condition at the end of the model (i.e. after 4.6 Ga of evolution). Since initially the models starts with 4 OM water in mantle it is reasonable to consider that this is the maximum amount of water to cycle through the system assuming that there is no external source of water in the system. Further, we consider the total amount of water into the mantle spectrum (Fig. 1.13b). Since high regassing efficiency produces an excess of water into mantle reservoir values above 0.01 for χ_r exclude themselves for consideration since they bring more water back than is potentially available at surface because of outgassing, violating the mass balance in the system. In addition, considering the origin of the surface water entirely due to mantle degassing, means that the mantle must remain with about 2.5-3 OM or it could be considered too dry to meet the planetary exosphere constraint. This leaves a narrow band of possible solutions with χ_d ranging between 0.002 and 0.04 and χ_r between 0.001 and 0.01.

The extent of the melt zone (Fig. 1.13c) and the amount of water in the melt extracted (Fig. 1.13d) are two factors that influence the magnitude of degassing. Their distribution function is complex because of the nonlinear dependence on the two principal parameters. We show that a extremely wet mantle still produces a low extent of melting as well as dry melt if the temperature falls below about 1600 K. This situation happens for high regassing numbers and low-to-moderate degassing constant values. However, high temperature but dry mantle

still produces an extensive amount of melt but it is deficient in generating a wet melt able to allow for high amounts of degassing flux. This is significant since this situation occurs for high degassing/regassing ratio in terms of efficiency that would normally yield high-degassed flux. This result explains the relative low influence of the degassing factor compared with the regassing one. In this zone, an increase of degassing constant would not be very effective in increasing the volume of water degassed since there is not enough water in the melt to scale the flux up and increasing the degassing factor even more would raise the temperature even further. Since water in the extracted melt is inverse-proportional with the melt fraction of the extract (Fig. 1.3) then extensive melt is not a favorable condition for the outgassing process since it produces a drier melt. However, outgassing is stimulated in the two moderate zones in the upper right corner that overlap a volatile rich mantle over an extended melt zone and center left side were the relatively lower mantle volatile content is balanced by a warmer thermal state. Both situations are characterized by low melt fraction as the temperature profile and the solidus line both offsets in the same direction as the mantle is cooling and become more volatile-rich toward the upper left corner of the spectrum.

The mantle average temperature displays a linear variation (Fig. 1.13e), increasing in general in the direction that favor outgassing and cooling in the direction that favor regassing. This is a normal trend for the volatile dependent viscosity as volatiles lower the temperature level. Water concentration and temperature of the mantle are the most important factors for the fate of all other derived variables since most of them scale with these two. Heat flux (Fig. 1.13f) tends to increase with the reduction in water cycling efficiency in general (toward upper right corner in spectrum) as this scenario leads to a wet mantle and with relatively high temperature conditions, which ensures lower viscosity and very efficient convection. As we

move toward more extreme conditions that are present for high χ_r ratio and low χ_d, the mantle becomes more volatized but too cold to sustain high heat flux. Higher ends for χ_d with low regassing rate limit the heat flux also as a result of being very dry, although extremely hot. Along with heat flux, a similar variation exhibits also the thickness of the hydrated layer that scales with heat flux but in the opposite direction. High flux develops a high temperature gradient in the lithospheric layer and this reduces the depth of the serpentine stability field. The regassing flux however is smoothed by the opposite effect of convection velocity that increases with heat flux thus compensating partially the reduction in the thickness of the hydrated layer. Since constraints on the present day heat flux can be imposed at about 70 mW/m^2, along with the constraints on the amount of degassing discussed above, we can limit the extent of the efficiency factor variation to a narrow optimum zone described by $\chi_d \sim 0.02 - 0.04$ and $\chi_r \sim 0.003 - 0.01$. Similar results were obtained by using different initial amount of water in mantle.

Implications for planetary evolution

Water concentration in the mantle

Degassing of the mantle is a source for the water that forms the Earth hydrosphere. At the surface, water is stored in the oceans, atmosphere and crustal components like hydrous minerals or even as free water. Part of the initial water was lost through exospheric escape process although the amount was not significant in the case of Earth as it was for Venus for example. To form the present hydrosphere requires that about 1.2 OM of the initial water in mantle was degassed and remained at the surface. We use our model runs for different initial amounts of water in mantle to estimate the initial and final average mantle composition

regarding water subject to the constraint that the present hydrosphere contain 1.2 OM. Three runs were performed for 2, 4, and 6 OM initial water content, and the results display a linear variation of final versus initial composition of water in the mantle (Fig. 1.14). The correlation line has a very gentle slope because of self-regulating capacity of volatile dependent convection and this fact constrain effectively the current values of water content. Interpolating the function, for initial values of ~2.35 OM the final concentration was about 1.15 OM. This scenario satisfies the mass conservation constraint using our parameterization, with a mantle that lost about half of its initial water because of outgassing.

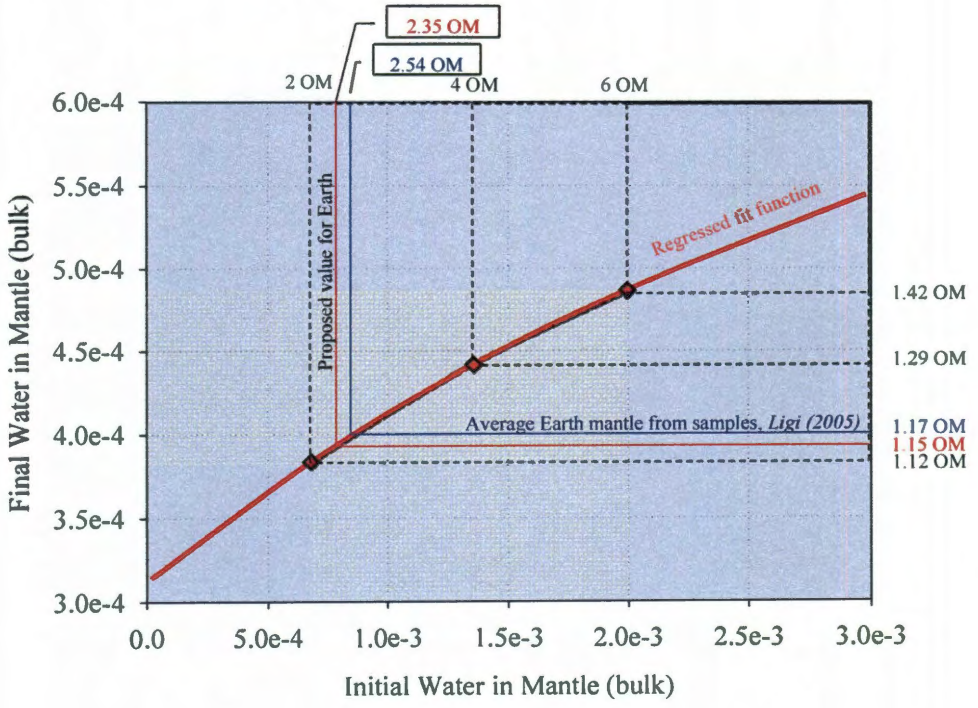

Figure 1.14. Mantle degassing analysis. Initial versus final amount of water in mantle for three test runs along with regressed function. Data presented as mass concentration as well as total water in mantle in ocean masses (OM). The plot is used to estimate present and initial water content in the mantle (red guidelines) by constraining the difference between these two values to mach the amount of water at surface at present. The results are compared with values derived from estimates for water concentration in the mantle based on some samples around the world (blue guidelines).

Sample analysis of upper and lower mantle material correlated with isotopic analysis of the similar compatible elements provide valuable estimates of water content of the mantle (Ligi *et al.* 2005). Normal Mid Ocean Ridge Basalt (MORB) considered as derived from upper mantle have usually low content of water with obtained values around 0.2 wt%. This, for a value of F=0.1 melt fraction and assumed partition coefficient for water of 0.01, yield about 0.02 wt% water in lower mantle. H_2O-rich sources emplaced on oceanic island basalts and considered originating in lower mantle, display higher values between 0.4 and 0.9 wt%. These values yield an average of 0.06 wt% for lower mantle material. Generally, for the whole mantle a rough average 0.04 wt% or $4*10^{-4}$ in absolute wt ratio was assumed. Integrated within the mantle volume this concentration adds an amount of water equivalent to about 1.17 OM, value in decent agreement with the result of our theoretical model (Fig. 1.14). The initial amount of water in this case is about 2.54 OM. There is still active debate regarding the storage capacity of the lower mantle material (Hirschmann 2006) triggered by the apparent contradictions between Icelandic type magma concentration and theoretical storage capacity of the lower mantle minerals. Other authors indicate the existence of a soaked channel at the base of the upper mantle that consist on a hydrous melt interval (Ohtani *et al.* 2004) that has a high capacity to store water and act as a "water filter" (Bercovici and Karato 2003). Regardless of the exact location and heterogeneity of the water concentration in the mantle, the total average value as predicted by our model still satisfy most of the known constraints imposed by the thermal evolution model and the global availability of the water on the planet.

The magnitude of water recycling process and implication for the heat lost

We have shown how efficiency factors that control the flux of volatiles out and back into the mantle could be constrained. However, since efficiency factors represent several

complex causes, their deconvolution in terms of implication for Earth is not a trivial task. A synthesis of current fluxes based on different methods of estimation is possible but still not comprehensive enough to evaluate the evolution of cycling fluxes through Earth history (Litasov and Ohtani 2007). Rough estimation for present day volatile fluxes tend to suggest current mantle condition as characterized by the general trend of volatiles regassing at subduction exceeding degassing at the MOR. Our modeling strongly supports this theory. Estimated fluxes range from 5.1×10^{11} to 1.83×10^{12} kg/y for total water cycled back to the mantle and $2.1\text{-}2.3\times10^{11}$ for water currently degassed at MOR (Peacock 1990; Maruyama 1999; Bounama *et al.* 2001; Jarrard 2003). Our estimates of regassing factor differ from that used by (McGovern and Schubert 1989) since we employed different parameterization for degassing and regassing. Some authors suggest values between 0.06 and 0.3 for the ratio of water that reaches deep mantle, values that depend on the temperature or age of the subducted slab (Rupke *et al.* 2004). Efficiency factors for degassing parameters are even more difficult to obtain because of difficulties to describe the exact geometry and physical properties related to the distribution of magma channel below MOR. Using the results from our efficiency factor analysis runs, we select a conservative path in χ_d vs χ_r space situated within the optimum zone and followed the evolution of the degassing and regassing flow rates (Fig. 1.15). The term conservative refers to the fact that along the path the total mass of water in the mantle is the same for any point on the path. For reference purpose, the path was continued into the non-conservative zone marked by the shaded area.

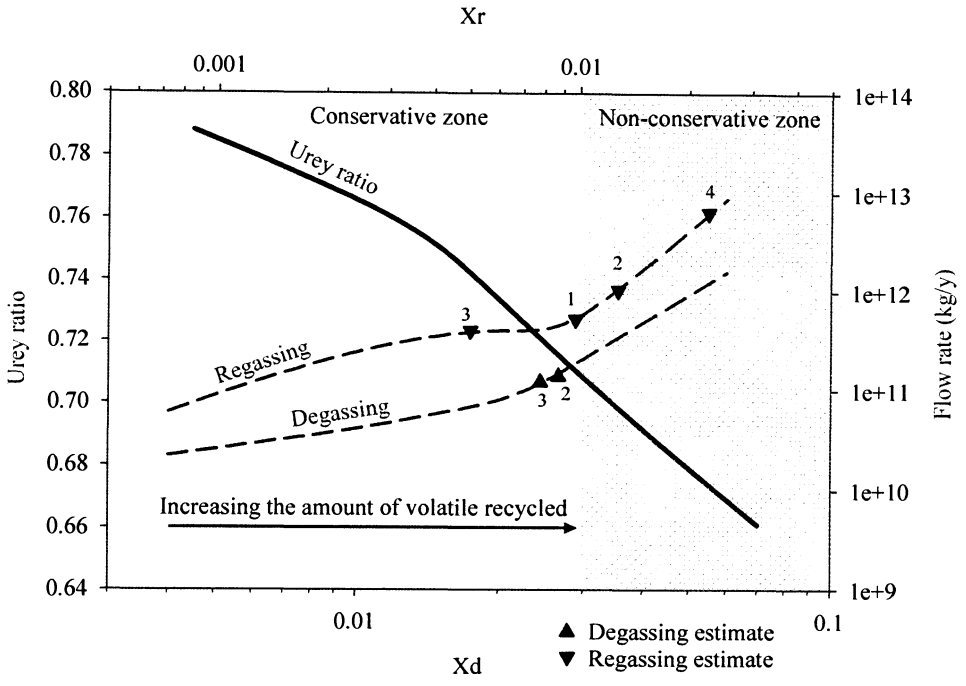

Figure 1.15. Degassing and regassing flow rates for various efficiency factors that ensured constant amount of water in mantle and the Urey ratio along the same path. The degassing and regassing fluxes intercept several estimates of other authors. The regassing rate at the end of the run is invariably greater than the degassing rate pointing to a state of overall rehydration of the mantle at present. The Urey ratio decreases with the amount of water recycled signifying an enhancement of the heat removal efficiency with the magnitude of the recycling process. Estimates are based on 1 – Peacock (1990), 2 – Maruyama (1999), 3 – Bounama et al. (2001), and 4 – Jarrard (2003).

Regassing rate is at any time above degassing ensuring overall recycling of water into the mantle. For comparison, we represented also the estimated values as given by various authors. The trend is to recycle more water as the efficiency factors increase, keeping the mass of water in mantle constant but with increased flow of volatiles both in and out of the mantle. This fact is important not only for the balance of the volatile flows but also for the thermal budget of the planet. As seen on Fig. 1.15 the Urey ratio also varies with the amount of water recycled, decreasing as more water is cycled through the system. This is significant since recent studies propose low values for the present day bulk Earth Urey ratio in the range of about 0.21

– 0.49 (Jaupart *et al.* 2007; Korenaga 2008). Removal of heat is influenced by the amount of regassing and degassing since volatiles affect the viscosity and implicitly the convection intensity. Degassing more volatiles raise the temperature of the mantle reducing the viscosity and more regassing reduces the viscosity further as volatiles are added back to the mantle. The recycling activity of volatiles could therefore be actively used to constrain the thermal state of the planet.

Dynamics of the volatile fluxes during thermal evolution

The evolution of the flow rates through history, recorded variation of the overall flux of volatile not only in term of magnitude but also in term of direction of the overall flow. We calculated the position in time when this situation occurred for different combination of degassing and regassing factors (Fig. 1.16).

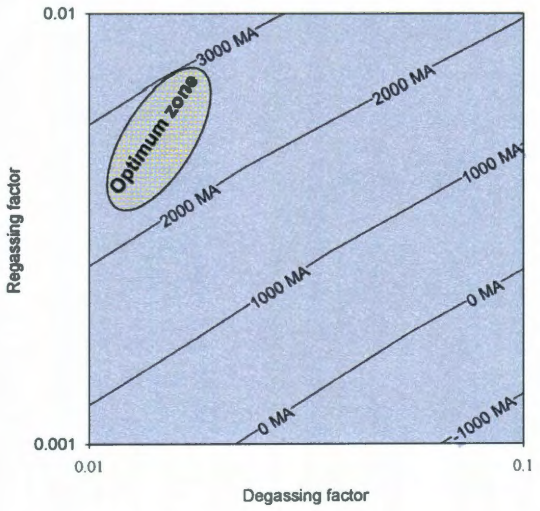

Figure 1.16. Tipping point occurrence. Probable time in (MA) when the volatile flow changed its direction from overall degassing to overall regassing for different combination of degassing and regassing factors. The optimum zone falls between 2000 MA and 3000 Ma.

The area described early as the "Optimum zone" falls between 2 and 3 Ga. This is supportive for the concepts of early massive degassing and formation of the atmosphere in Archean time followed by subsequent cooling. After the tipping point water from the oceans starts to cycle back into the mantle, and this process would predict a relative decrease of sea level through Phanerozoic. The decrease of sea level was better recorded in the last 800 – 600 Ma (Hallam 1992; Maruyama and Liou 2005). Before this, it is difficult to find geological evidence for variations of the sea level.

Conclusions

Our simulations of volatile dependent thermal evolution of planetary mantle aim to better integrate the volatile cycle within the framework of global evolution of Earth through its history. Although the primordial conditions of the planetary evolution is still a subject of great debate, our study revealed that some of the initial settings were rendered less important for the present day condition because complex feedbacks relationships regulate the many parameters of the planetary system. Like in the case of temperature previously known as being regulated by the feedback between its value and the viscosity of the mantle, a similar relationship develop between the amount of water in the mantle and the viscosity. A wet initial mantle would keep its viscosity low and the convection intensity high so the cooling process is enhanced in this case. However, a water-rich mantle has a more extensive melt zone and produces melt with higher concentration in this volatile element and consequently there is more water degassed during evolution in these conditions. A dry initial mantle will reversely tend to preserve more of the initial water. Because the volatile effect is overlapping the temperature effect, the thermal evolution for the volatile dependent mantle convection system is not as dramatic as in the case of nonvolatile dependence. The reason for this resides in the

double dependency of viscosity on temperature and water concentration. The mantle would cool much faster without the water feedback but if water cycle is considered, then rapid cooling of a hot, low viscosity and highly convective mantle is slowed down by the outgassing process that scales with the convection intensity and dry out the mantle. The viscosity is kept relatively high and the convection intensity is lower in this case. In term of thermal efficiencies, we note the effect water cycling on the amount of heat removed by the mantle convection process. The recycling of more water (i.e. increased degassing and regassing fluxes) helps keep the mantle viscosity lower for longer and maintains a greater heat flux per same thermal state of the mantle. Since the heat is produced at the same rate for all the simulations, this effect is well remarked by the decreasing of the Urey ratio as more water is recycled. The decrease recorded by our simulations are from a value of 0.8 to about 0.65 as we increase the degassing and regassing efficiency factors within a certain range. This trend is also satisfying more closely the geochemical models used to constrain the amount of radiogenic elements in the earth mantle.

The water cycle acts to regulate the mantle temperature, and thus buffer the thermal evolution of the planet. This regulatory effect in terms of temperature and water concentration allows us to predict the present day condition with a much greater confidence than the initial conditions. Currently there are many uncertainties regarding the factors that control the outgassing and regassing fluxes. If we have to run the simulations backwards, even a small-assumed error interval for the degassing/regassing efficiency factors would lead to large differences for the predicted values at the time of planet formation. By running several normal simulations with efficiency factors as free parameters, we constrained them by considering only the cases that satisfy all of the present day known condition for several mantle parameters.

Using values ranging from 0.02 – 0.04 for degassing and between 0.003 – 0.01 for regassing we predicted that at present the mantle contain an average value of 1.15 OM of water. The thermal evolution of the planetary mantle also has some important consequences for the dynamics of the volatile process itself. As mantle cooling progresses further the hydrated layer thickens and the volcanic processes associated with the degassing slows down. This inexorably will wet the mantle as the balance of degassing and regassing processes favor rehydration in the later stage of evolution. The fate of the mantle in the near geologic time is thus toward enhancing of its volatilization grade and this could be true as long as plate tectonic would still be active. However, different dynamics of the volatile cycling process on planets with stagnant surface tectonics could lead to different scenario and implications for its thermal evolution. In the next chapter, we will address these implications using a model of mantle convection for a planet that have no active plate tectonics.

Chapter 2

THE EFFECTS OF VOLATILE CYCLING ON PLANETARY THERMAL EVOLUTION FOR TERRESTRIAL PLANETS WITH STAGNANT LID TYPE OF GLOBAL TECTONICS

Introduction

The role of volatiles in regulating the thermal histories of planets is significant considering the effect on mantle viscosity by enhancing the creep regime of mantle material. Additionally, the volatile components like water and CO_2 play a major role in climate system and determine the surface temperature that feeds back in thermal convection of the planetary interior (Phillips *et al.* 2001). Previous studies investigated the thermal evolution of Earth in parallel with its degassing-regassing history and outlined different progression paths according to each change in volatile content attributes (McGovern and Schubert 1989; Franck and Bounama 2001). The most important volatile element studied was water since it is the element most planetary wide cycled. Experimental results indicate that water presence in upper mantle components greatly reduces the viscosity (Chopra and Paterson 1984; Karato *et al.* 1986; Hirth and Kohlstedt 1996) and through a simple negative feedback mechanism this enhances its convective intensity with consequences for further thermal evolution.

However, Earth is characterized by a very original convective mechanism among the terrestrial planets we know to date, as its upper boundary is continuously regenerated and recycled through convection. The rest of the planets are characterized by an immobile surface of various thicknesses that is essentially not participating in the convection process but act as conductive lid on top of the much deeper convective system (Moresi and Solomatov 1998). Such a setting presents a particular mechanism for cooling and degassing that is not directly

scalable from the Earth-like parameterization and is determined largely by the stress regime in the convecting mantle (Solomatov and Moresi 1996) and also by the strength of the lithospheric plate (O'Neill *et al.* 2007a). While the mechanisms and exact trimming of switching between the two regimes for a particular planet are still controversial, it was demonstrated through theory and numeric experiments that a stagnant lid regime is extremely less efficient in transferring heat out of the planetary interior compared with plate tectonics regime (Reese *et al.* 1998). Both stress level and strength are related to the thermal state and water content especially through viscosity connection and hence the complex relation between water and the fate of planets evolution. Another important aspect of the problem comes from the effect of water in generating a melt channel crossed by the convective movement. The formation of the melt channel is the result of the geothermic relationship between peridotite petrology phase and the mantle adiabat (McKenzie 1984; McKenzie and Bickle 1988). The role of water is relevant since it allows the Solidus and Liquidus lines to shift (Hirschmann 2000) thus increasing the amount of melt extract for the same temperature as mantle is wetter. This has implications for the amount of water degassed through intraplate volcanism associated with the extensive melt generation (O'Neill *et al.* 2007b), and with the amount of water remained in mantle (Hirschmann 2006). Partial melting is also affecting compositional layering and buoyancy distribution within the lithosphere and some authors suggest this relation is a critical element that determines a switch in the plate tectonic regime from a stagnant lid to plate tectonics (van Thienen *et al.* 2004). Among other parameters, like gravity, surface temperature and planet size, the water content of the mantle influence the thermal evolution of a planet especially in the early stages.

In this study, we investigate the magnitude and potential implications of the degassing process to the planetary evolution by implementing a parameterization specific to the stagnant lid type of mantle convection, and assimilating a volatile cycling system particular to the lack of lithospheric subduction setting and variable melt-zone degassing.

Model parameterization

The study employs a parameterized mantle convection model coupled with a variable-concentration melting model to derive planetary thermal evolution based on various mantle volatile concentrations. The approach is similar to the one used in previous chapter of this work when we investigated an Earth-like planet with active plate tectonics mechanism at surface (thin lid convection parameterization). However, we extend the investigation to cover the case when the planet is characterized by a cold upper boundary layer. This layer develops a condition characterized by large viscosity contrast between the hot internal mantle and the cold surface (Torrance and Turcotte 1971). In our previous approach although we allowed a time variation for the temperature dependent viscosity the convection scaling assumed an isothermal mantle and the spatial variation was ignored. The current method implements a scaling law for temperature-dependent viscosity derived from a physical analysis of boundary layers that suggests scaling relations for all convective regimes (Solomatov 1995). The analysis considers that the integral viscous dissipation in the system is balanced at any time by the integral mechanical work done by thermal convection per unit time. This type of convective system characterizes all terrestrial planets in our solar system except Earth (Schubert 1978).

We consider a planetary system that has stagnant lid developed on top of a fast convective interior (Fig. 2.1). Since we are using a 1D model, the lateral variations of geometric features are assumed constant and their values are considered as their average over the interval.

The stagnant lid has the thickness of δ_{sl} variable in time and the effective boundary layer below the stagnant lid has the thickness δ_{bl}. Outgassing occurs on top of a melting channel formed as a result of partial melting. The width of this channel is determined by the convective velocity expressed per unit of time and the length was taken a constant value equal with the total length of the present day mid-ocean ridges. Since the convection does not reach the surface, a regassing process that would bring volatiles from surface back to mantle was assumed inexistent.

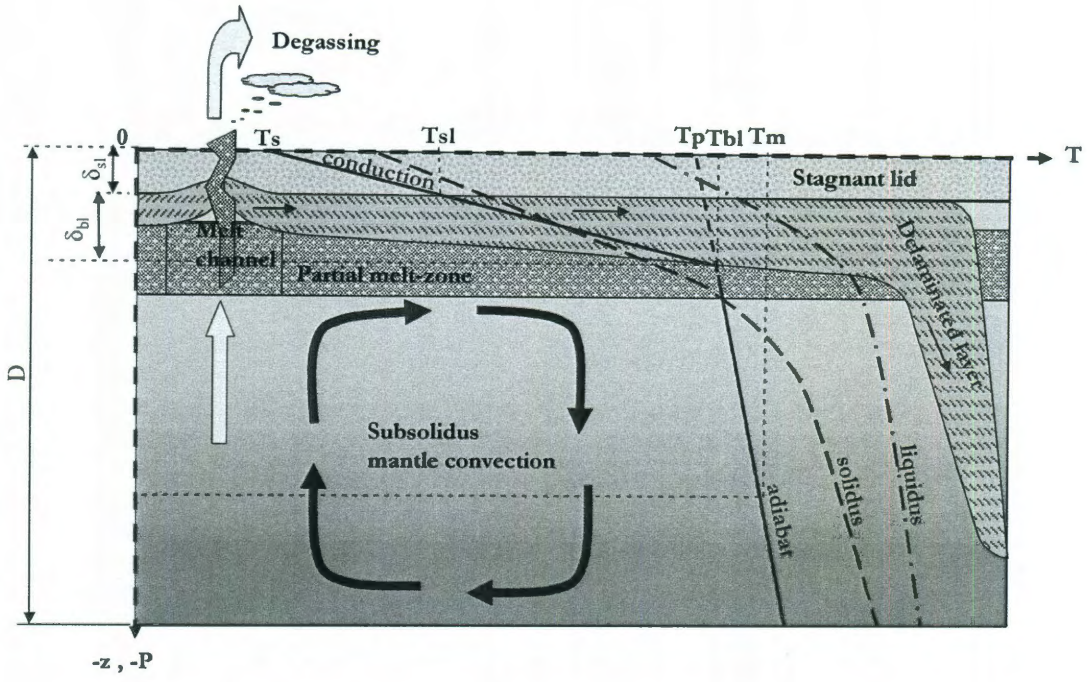

Figure 2.1. Schematic section of the volatile circulation system depicting main fluxes and reservoirs for planetary system with stagnant lid type of convection.

For the stagnant lid, the convective regime is not characterized anymore by only one Rayleigh number. In the stagnant lid region near the surface as the viscosity increases exponentially the effective Rayleigh number falls below the critical value for convection to take

place. This is the theoretical criteria for the establishment of the stagnant lid. The viscosity is exponential of temperature so a linear distribution of temperature in the top boundary layer results in the exponential increase in viscosity toward surface.

$$\eta = \eta_m \exp(-\gamma(T - T_m))$$

where η_m is the viscosity of the hot mantle interior γ is a constant and T_m is the average mantle temperature and T is the temperature where the reference viscosity was calculated.

At some point where the temperature is T_{sl}, the viscosity contrast reaches a critical value for which the instability occurs only in the thin sub-layer near the bottom of the boundary layer that becomes the local boundary layer.

$$\theta_{cr} = \frac{\eta_{sl}}{\eta_m} = \exp(\gamma(T_m - T_{sl}))$$

This new local boundary layer of thickness δ_{bl} characterizes only the active convecting system. The upper limit of this layer thus marks the boundary between the stagnant lid and the convecting mantle. Based on this definition we can observe that this boundary is not defined by a fixed isotherm but by a fixed value of viscosity contrast that is constant for the entire thermal evolution (Grasset and Parmentier 1998). Furthermore, by constraining the viscosity contrast to a predefined value, we were able to calculate the thickness of the stable layer. Several experimental (Davaille and Jaupart 1993) and numerical (Moresi and Solomatov 1995; Manga *et al.* 2001) studies addressed the problem of transient convection beneath a cold surface and they indicate that a stagnant layer develops once the viscosity contrast across the cold thermal boundary layer exceeds about $3*10^3$. Below this strictly conducting lid of variable

thickness, the convection takes place just as would do in the isoviscous case but with the new temperature difference and new scale (Lenardic and Moresi 2003). An effective Rayleigh number characterize the convection in this region:

$$Ra_{eff} = \frac{\rho_m g \alpha (T_m - T_{sl})(D - \delta_{sl})^3}{\eta_i \kappa}$$

where ρ_m is the mantle density, g is gravitational acceleration, α is the coefficient of thermal expansion, κ is the mantle thermal diffusivity and D is the total thickness of the mantle. The effective Rayleigh number scales with the Nusselt (Nu) number by a 1/3 power law and heat-flux out of the mantle is determined from this scaling:

$$q_m = k\frac{(T_m - T_{sl})}{(D - \delta_{sl})} Nu = k\frac{(T_m - T_{sl})}{(D - \delta_{sl})}\left(\frac{Ra_{eff}}{Ra_{cr}}\right)^{\frac{1}{3}}$$

where k is the mantle thermal conductivity, and Ra_{cr} is the critical Rayleigh number for the initiation of convection. In other words, we can define the upper stagnant lid as the layer whose convection intensity is characterized by $Ra => Ra_{cr}$. The mantle temperature is then solved by numerically integrating the differential equation of the energy balance in the system similar to what we did in previous chapter.

In the absence of plate tectonics regime, the mechanism by which the mantle losses its volatile is described by a similar process of unilateral melt-related degassing (Phillips *et al.* 2001). Planets that lack an active plate tectonics system exhibit such a process that involves very active intra-plate volcanism. The parameterization in this case requires that estimation of the volatile flux to be done by using a slightly different method than the case of total

lithospheric recycling. A simple approach is used since there is no unified theory about the mechanisms of lithospheric recycling and volcanism for single plate tectonics regime. We consider the volcanic degassing still proportional with the thickness of melt zone as mentioned above and assuming no major resurfacing event. Volatiles out-gassed originate in this zone, and therefore their flow rate is still proportional to the thickness of the zone and the volatile content of the melt extract. Although spreading centers are absent in this case, we still have to scale the convection velocity along with the length of a proto-spreading axis in order to obtain an estimate of the flow rate of volatiles out-gassed at the intraplate volcanic centers. It is probably true that the degassing efficiency factor χ_d is considerably lower in this case due to thicker and static boundary layer on top of the melt region. The melt zone was determined by calculating the integrated melt in the area situated between the average temperature profile through the mantle and the solidus line (Fig. 2.1). The solidus calculation was based on a wet melting model that produces dynamic solidus and liquidus lines according to bulk volatile concentration in the mantle and the amount of melt extract (Katz *et al.* 2003). The mantle temperature profile is composed from two parts: the adiabatic region between T_m and T_{bl} and the conductive region between T_{bl} and T_s. The topology of the solidus and temperature profile is changing continuously as the mantle evolves in time producing various melting conditions.

The thin lid parameterization follows a model of mantle convection and volatile cycling described in more detail in chapter 1 of this work. The parameters used were set equal to the known values for the present day Earth in order to be able to make comparative analysis of the results.

Temperature and volatile evolution for a planet in stagnant lid state

We analyzed the thermal evolution of an Earth-like planet for different initial volatile content and we concurrently used stagnant and thin lid parameterizations in order to illustrate the differences in thermal evolution path among them. As a reference, we also ran for the stagnant lid cases a set of tests using constant water content and no coupled volatile effect thermal evolution. Variable initial water content was set to 1, 2, 3, 4, and 6 OM. A set of selective results are presented in Fig. 2.2, and it shows differences of about ~100°K among different volatilization states as well as between the two tectonic style parameterizations.

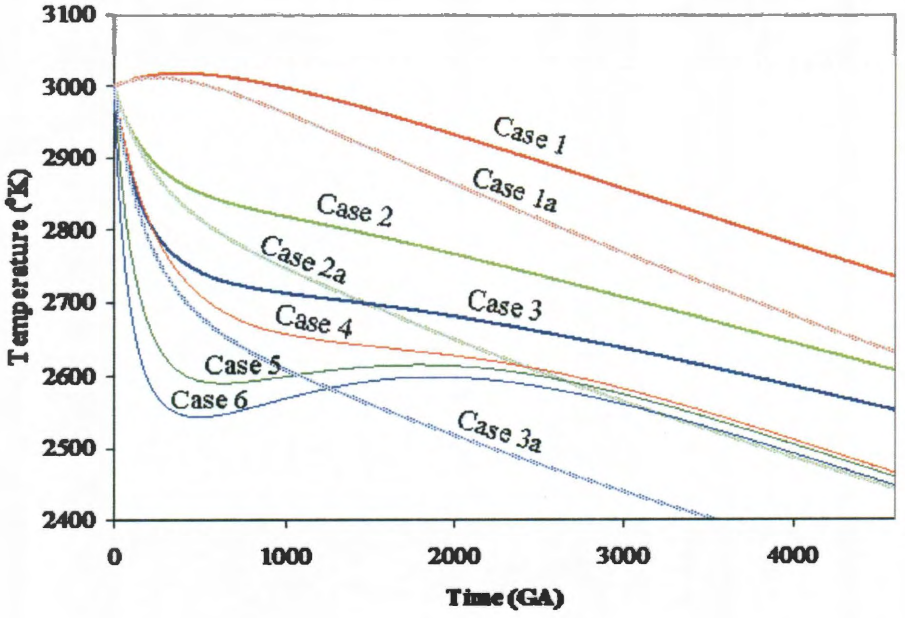

Figure 2.2. Comparative mantle temperature evolution for different tectonic styles and initial volatilization level. Cases 1, 2, and 3 represent the runs for 2, 4, and 6 OM initial volatile level respectively and the stagnant lid parameterization. Cases 1a, 2a, and 3a are the same parameterization but with no volatile model coupled (constant water amount in mantle). Cases 4, 5, and 6 are the runs for 2, 4, and 6 OM initial volatile level respectively and the thin lid parameterization.

The general trend for all runs is the decline of mantle temperature with time, the final cooling rate being almost the same for all runs and regulated by the decay rate of radioactive elements in the mantle. However, they follow different temperature paths as various initial conditions have a pronounced effect especially in the initial phase of evolution when high temperature and vigorous convection act decisively on the outgassing process. The stagnant lid runs display always a higher temperature than their corresponding thin lid evolutions and this is explained by the lower efficiency in removing heat that characterize the stagnant lid setting. The volatile content plays also an important role in establishing the temperature levels of which the mantle run. This attribute affects the viscosity through the negative feedback loop, and it helps along with temperature to regulate the heat flux out of the mantle. It is significant that for some concentration values in a dry mantle (Case 1), the initial trend is to increase the temperature before the cooling stage takes place. The fact is important for the melt condition that is extensive at that stage. When the volatile content is enhanced the temperature follows a decisive cooling trend at the beginning (Case 2 and 3) before a steady state is acquired later in the evolution. The different evolution patterns are liked to the coupling between temperature and volatile content effect in establishing the mantle viscosity. A dry mantle would be too viscous to assure enough heat flow to balance the radiogenic heat produced at time. This would allow the temperature to rise inside and the second effect (viscosity-temperature) would act to keep the viscosity at optimum level. The whole mechanism shows the importance of volatile cycling process and gives dimension to the effect of the volatile amount initially present in the mantle in the fate of its thermal evolution. It is important to note that for some water concentration level the cooling process is in the steady state right from the beginning of the run and remain in steady state through entire thermal evolution. This tipping amount represents the volatile concentration that produces the minimum effect on the heat flux

regulation. The reference cases (1a, 2a, 3a) ran with constant water concentration outlines the effect of outgassing. In these cases the mantle cools better than their outgassed counterpart does since the mantle is always wetter as no regassing is process bring water back in the system.

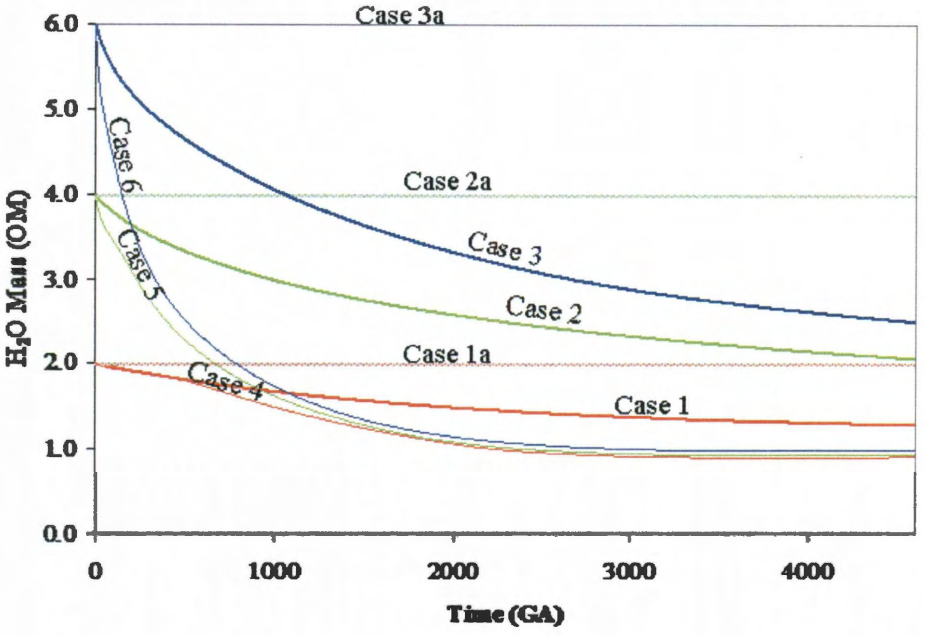

Figure 2.3. The degassing history for the cases analyzed. . Cases 1, 2, and 3 represent the runs for 2, 4, and 6 OM initial volatile level respectively and the stagnant lid parameterization. Cases 1a, 2a, and 3a are the same parameterization but with no volatile model coupled (constant water amount in mantle). Cases 4, 5, and 6 are the runs for 2, 4, and 6 OM initial volatile level respectively and the thin lid parameterization.

Degassing histories are presented in Fig. 2.3. For the stagnant lid cases, the degassing process is less efficient in part due to the presence of the thick lid on top of the convecting system. The stagnant lid thus becomes a barrier not only for the heat but also for the volatiles rich melt ascending to surface. The less efficient mechanism of degassing somehow compensates the absence of a recycling mechanism and allows the mantle to remain wetter

than if would follow a thin lid evolution. However, the water lost cannot be replaced, and this is a limiting factor in regulating the volatile concentration in the mantle. In the case of Earth-like planets, as mantle cools the hydrated layer that is recycled grows, and more water is steadily brought back to the mantle (Rupke *et al.* 2004). This helps keeping the viscosity low enough and the convective vigor still elevated so outgassing and regassing balance better even when the convection intensity decreases. This results in mantle evolving toward the same concentration level in time regardless of the initial condition. For the stagnant lid cases the evolution leave mantle at very different concentration levels for each different initial condition runs.

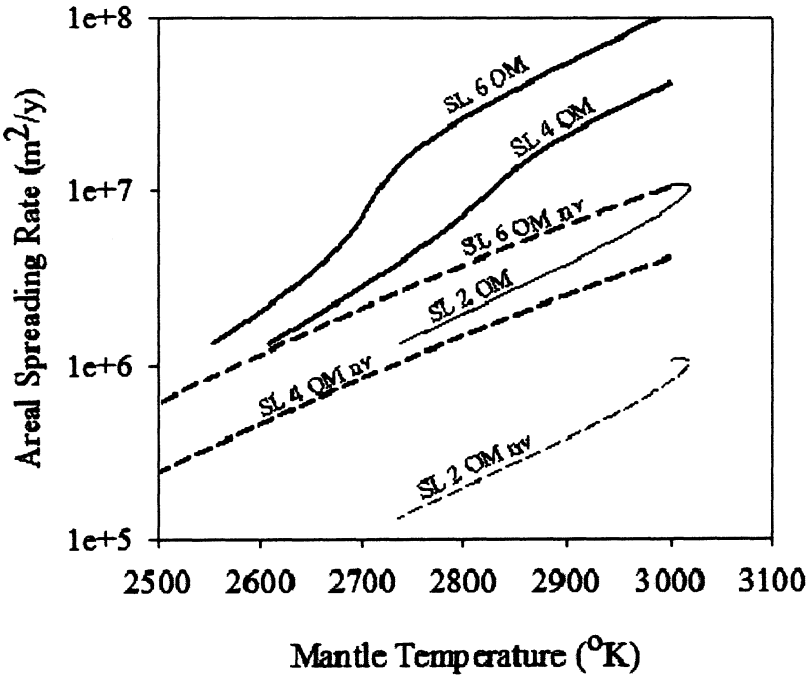

Figure 2.4. Areal spreading rate as a function of temperature. The areal spreading rate controls the degassing and represents the amount of lithospheric surface created by the convective movement per time.

Two main factors determine the magnitude of the outgassing process: the areal spreading rate of the mantle entering the melt zone, and the extent and richness of melt extract in this zone. The areal spreading rate is related to the convection velocity and to the convective vigor in general. It tends to decrease in time along with the temperature (Fig. 2.4) as the convection slows down. If now volatile effect is in place, there is a linear correlation between temperature and the spreading rate. However, the runs that involves outgassing in the stagnant lid case we notice a skewed line that is more pronounced as the mantle is wetter. This could be explained by a process that would allow the convection to run slower for relatively the same temperature. This fact is not so obvious since the feedback relation would adjust the temperature up if the convection slows down. Based on the nature of feedback relationship that includes the volatile effect, the explanation would involve a phenomenon of enhanced degassing that dry out the mantle faster than predicted by the spreading rate. Thus, we arrive at the second factor that determines the outgassing, the extent and quality of the melt zone.

The melting process under the stagnant lid presents some specific characteristics and we derived a melt potential spectrum for an average stagnant lid setting on top of which we plotted three evolution paths corresponding to volatile contents of 2 OM, 4 OM and 6 OM initial condition (Fig 3.5).

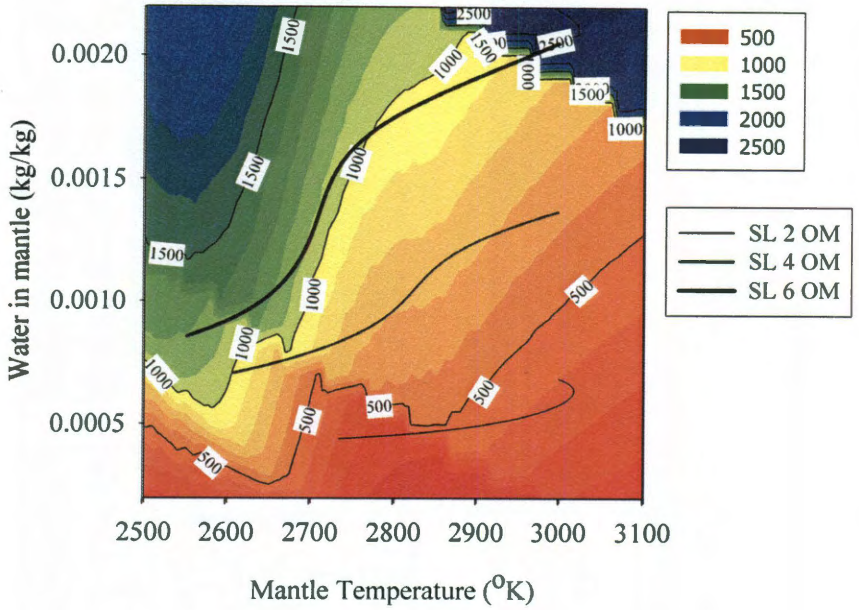

Figure 2.5. The degassing potential as a function of melt channel thickness and melt fraction volatiles content. The spectrum scale represents kg of water per kg of melt extract times melt zone thickness. Overlapped are three evolution paths in Temperature-Concentration coordinates.

The spectrum was calculated by running the melt model for a matrix of mantle temperature/volatile concentration sets ($T_{m(i)}$, $c_{m(j)}$) and then interpolating the results. The melt model corresponds to mantle convecting below an average 50 km thick stagnant lid. The spectrums for melt fraction (F), water in melt fraction (X_{H2O}) and melt thickness (L_{melt}) were then overlapped by multiplication in order to obtain an integrated outgassing potential. We can now trace the evolution paths in T_m-c_m coordinates for the cases selected and notice when they encounter a high outgassing potential. The low concentration 2 OM curve evolves mostly over the dry area and the outgassing is therefore limited and controlled by the spreading rate. Most of the volatiles are lost at the beginning when spreading is rapid and then steady but at low rate with no major change in conditions. The dry mantle in this case generates a lot of melt but the

extract is depleted in volatile so overall there is not much water available for outgassing. As opposed, the wet run (6 OM) at some point crosses the high potential area (green) which causes an enhancement in the outgassing rate accelerating the depletion in volatile and in turn adjusts the viscosity so that mantle convection slows down relative to temperature. The evolution of 4 OM run falls somehow in between, therefore we can conclude that the effect increase with volatile bulk composition in the mantle. As results from Fig. 2.5, the outgassing potential varies with mantle temperature increasing with bulk composition of volatiles and slightly decreasing with temperature. While direct correlation with the bulk composition is expected, as more water in mantle would make more water available to enter the melt phase, the relation with the temperature more concealed. As the temperature raises the fraction of melt in the melt zone increases, but due to fractionation of water in the melt (water preferentially accumulates in the melt phase) the water concentration in the melt extract is progressively reduced.

Implications for planetary evolution

Based on the parameterized runs mentioned earlier we compiled a comparative analysis of the evolution models that quantify in relative terms the effect of mantle volatilization degree on the planetary cooling and degassing efficiency (Fig. 2.6). The cooling efficiency was calculated as a percentage of the initial mantle temperature of the temperature difference between the initial and final conditions. Similarly, degassing efficiency represents the percentage of the water lost during the run to the initial value.

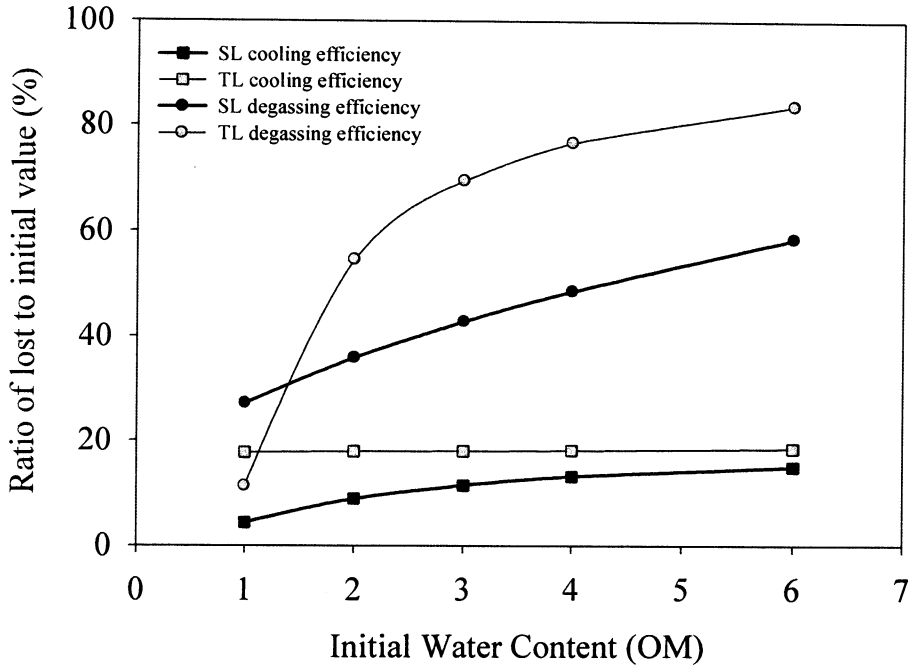

Figure 2.6. Cooling and degassing efficiency for stagnant lid and thin lid parameterization respectively. Plots represent the percentage of temperature and amount of water lost to their initial value.

The cooling effect in the case of thin lid evolutions proved not to be much affected by the amount of water initially in the mantle. At the end of the runs, the efficiency stabilizes invariably to about 18%. The stagnant lid however, is affected in a definitive manner as more volatiles present initially increases the cooling efficiency. This supports the idea that plate tectonics have a much greater potential to self regulate its thermal evolution than convective systems with a stagnant lid on top. By having the ability to recycle some of the water back into the mantle, thin lid systems can adjust their viscosity faster to optimize the heat flux and bring the system closer to the steady state condition. In terms of degassing efficiency, both systems experience an increase in efficiency with the initial volatilization degree. The plot shows that thin lid condition is greatly affected by the initial volatilization of the mantle. The stagnant lid

case although missing a regassing mechanism, is more conservative in terms of water lost during evolution.

Beyond the comparative analysis, it is important to consider the potential role of volatile concentration and degassing on the eventual transition between the two states. The transition could be considered stress activated, although a definitive consistent mechanism is yet to be developed. We traced the normalized viscous stress (Fig. 2.7) and found that stagnant lid cases are in a noticeable lower stress state than the thin lid cases. While the self-regulating capacity of the thin lid condition bring the stresses to a common level regardless of the initial amount of volatiles, the stagnant lid cases are strongly affected by the volatilization condition and they effectively never come to the same level during the length of the run.

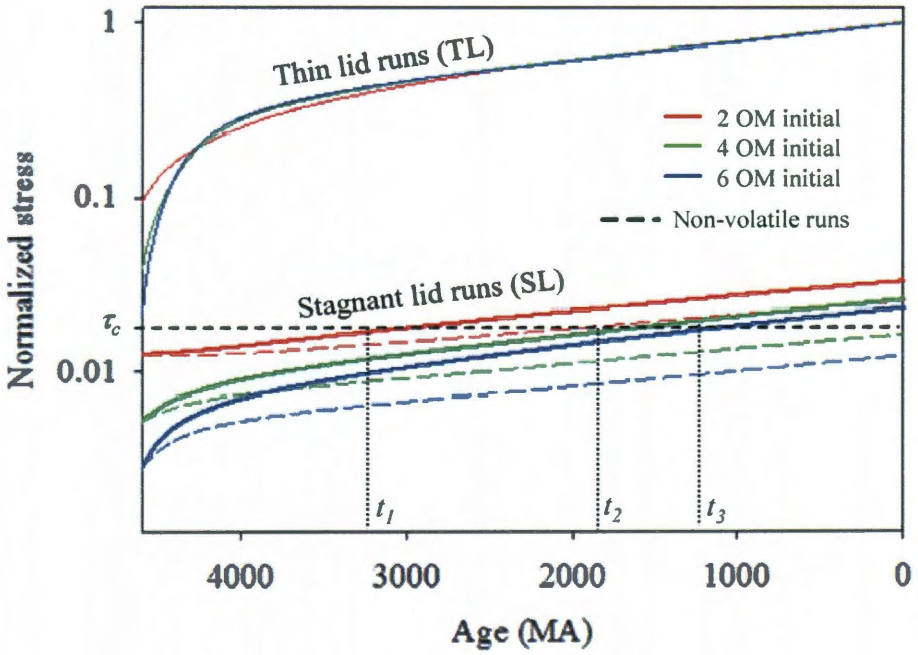

Figure 2.7. Normalized viscous stress evolution and the potential switch in the tectonic regime.

If we assume an arbitrary critical level for stress τ_c, that would be required to transition the stagnant lid to active plate tectonics then the resulting timing of which such an event would occur varies greatly from one run to the other (t_1, t_2, t_3). If planets that appear different today have started their evolution in similar conditions, then their degassing history or the availability of water during their formation could have been played the key role in their tectonic evolution fate.

Conclusions

Terrestrial planetary systems that fully recycle only a part of their lithosphere have not only a specific mechanism for heat removal but also a particular way to cycle their volatiles. The outgassing process is manifested by large-scale volcanism at surface and is a one-way only process during normal evolution of the planet. Since the convective system of its mantle is situated under a stagnant lid that covers the entire surface of the planet, the recycling of the surface volatiles is possible only during a major resurfacing event. This possibility was not considered in our simulations. Although recycling is absent, the water is preserved in the mantle for a longer time due to sluggish convection and slower outgassing rate through the thicker lithosphere as compared with an Earth-like planet where degassing at the mid-ocean ridges occur near the surface. The stagnant lid cases appear therefore to remain during their evolution wetter than the thin lid cases that started with the same initial condition. Thin lid systems recycle their volatiles, and the thermal evolution in this case is well regulated by them. The strong negative feedback that develops between mantle viscosity and volatile concentration bring the system to a similar state fast and regardless on other parameters. Since the stagnant lid systems tend to keep their volatiles longer, their evolution is heavily affected by the presence and amount of these volatiles at the time of formation. If assuming that the stress

level play the critical role in transition from stagnant to thin lid tectonic style as suggested by many authors, then the volatile content in the mantle can largely control the timing of this switch. We found that a doubling of initial volatile content for example could delay the transition with more than 1000 MA in our test runs. Water turns to be a critical element not only for life on a planet but also for the life of the planet itself.

Chapter 3

EARTH'S EVOLVING STRESS STATE AND THE PAST, PRESENT, AND FUTURE STABILITY OF CRATONIC LITHOSPHERE

Introduction

Cratons are sections of continental lithosphere that have remained stable over geologic time scales. They are associated with fast seismic anomalies extending 200-300 km in depth, an observation interpreted to indicate thick cratonic lithosphere (Grand 1987; James *et al.* 2001). Diamond inclusions within kimberlites indicate that the lithosphere of several cratons was as thick in the Archean as it is at present (Boyd *et al.* 1985; Bell and Blenkinsop 1987). This suggests that both cratonic crust and deep cratonic lithosphere can remain stable over long time scales in the face of vigorous mantle convection.

From a broad-brush perspective, the role of cratons in the super-continent cycle has generally been seen as one of focusing deformation during supercontinent dispersal. The stability of cratonic lithosphere can focus deformation to mobile belts that border cratons (Smith and Mosley 1993). This, in turn, can lead to a tendency for supercontinents to rift apart along sutures that follow mobile belts and avoid cratons (Vink *et al.* 1984).

In detail, the role of specific cratons within the super continents cycle is more enigmatic. The Sino Korean craton provides a case type example (Rogers and Santosh 2006). Not only does this craton stand out in terms of highlighting outstanding issues related to the role of cratons in supercontinent history but it also stands out for being the best studied example of a craton that has experienced geologically recent decratonization and lithospheric loss (Menzies *et al.* 1993; Gao *et al.* 2002; O'Neill *et al.* 2008).

Craton stability requires that the agents that cause tectonic deformation are buffered from cratons and/or that cratonic lithosphere is resistant to deformation. The latter is achieved if the strength of cratonic lithosphere is sufficient to overcome the stress levels generated by the agents of tectonic deformation (continental collision, delamination, rifting, and subduction). Quantifying the conditions that allow for craton stability has been an active subject of research (Jordan 1978; Pollack 1986; Manga and O'Connell 1995; Doin *et al.* 1997; Lenardic and Moresi 1999; Lenardic *et al.* 2000; Lenardic *et al.* 2003; Ritzwoller *et al.* 2004; Sleep 2006). Dominantly, these investigations have focused on the properties of cratonic crust and lithosphere (i.e., relative cratonic strength and buoyancy). In terms of mantle variations over time, the general thought has been that more vigorous mantle convection in the past would have made cratonic stability more difficult to achieve. For this reason, the geologically recent decratonization and lithospheric loss documented in North China is viewed as surprising (Menzies *et al.* 1993; Gao *et al.* 2002; O'Neill *et al.* 2008).

Recent decratonization could reflect a change in the properties of cratonic lithosphere (e.g., hydration induced weakening (Li *et al.* 2008). Our intent is not to argue against this possibility but instead to show that the evolution of mantle convection makes the recent geologic era less conducive to craton stability than the geologic past. Thus, any weakening is more likely to lead to craton instability at present than it was in the past. This may seem to run counter to the intuitive notion that more vigorous mantle convection in the Earth's past would have made stability more difficult to achieve. However, the dominant factor leading to greater convective vigor in the Earth's past is a lower mantle viscosity (Tozer 1972; Davies 1980). We have previously shown how a lower mantle viscosity, due to increased mantle temperature, can lower convection induced stress levels (Lenardic *et al.* 2008). The theory developed in that

paper addressed the issue of whether a runaway greenhouse effect on Venus could have lead to a level of mantle heating that shut down plate tectonics. Although this application is very different from addressing stress levels due to mantle cooling over geologic time, the main idea carries over: Lower viscosity dominates in the scaling of mantle stress. The theory of Lenardic et al. (2008) cannot be directly carried over to the cooling of the Earth's mantle, as the temperature change is not imposed from the atmosphere above as for the Venus case but results from the cooling of the mantle over time as internal heat sources decay. We will show, however, that this difference does not effect the general conclusion that a hotter mantle can be associated with lower levels of convective stress. From this starting point, we will argue that mantle convection induced stress levels increase from the past to the present and that this leads to a greater potential of craton deformation.

Mantle stress

Increased convective vigor in the Earth's past does not imply increased stress levels. Although not explicitly noted, this statement is supported by thermal history models (Davies 1980; Schubert *et al.* 1980). These models are based on a parameterized convection approach. Theoretical scalings are used to relate mantle heat flow to convective vigor, expressed in terms of a Rayleigh number, Ra (the ratio of thermal buoyancy forces driving convection to viscous resistance and thermal diffusion). The heat flow scales as Ra^{β} where, for classic thermal history models, the scaling exponent, β, is taken to be 1/3. Plate velocity, v, scales as $Ra^{2\beta}$ and convective stress scales as $\mu v/d$, where μ is the viscosity of the mantle and d is a length scale comparable to mantle depth (Turcotte and Oxburgh 1967; Turcotte and Schubert 1982). The Rayleigh number scales as the inverse of mantle viscosity, which decreases exponentially with temperature (Kohlstedt *et al.* 1995). Decreasing internal heat production over geologic time will

cause the Rayleigh number to decrease and, as a result, velocities will decrease. However, the decrease in internal temperatures will increase viscosity. For a vigorously convecting system with a strongly temperature-dependent rheology, like the Earth's mantle, the change in viscosity can outweigh the change in velocity and convective stress would then increase over geologic time.

To demonstrate that lower convective stress in the Earth's past is inherent in classic thermal history models, we reproduced a case from Schubert et al. (1980) using the parameter values those authors found to generate a thermal history most consistent with the data constraints available to them at that time. The predicted convective stress over time is shown in Fig. 3.1 (for subsequent comparisons we have normalized the stress to the model predicted present day value).

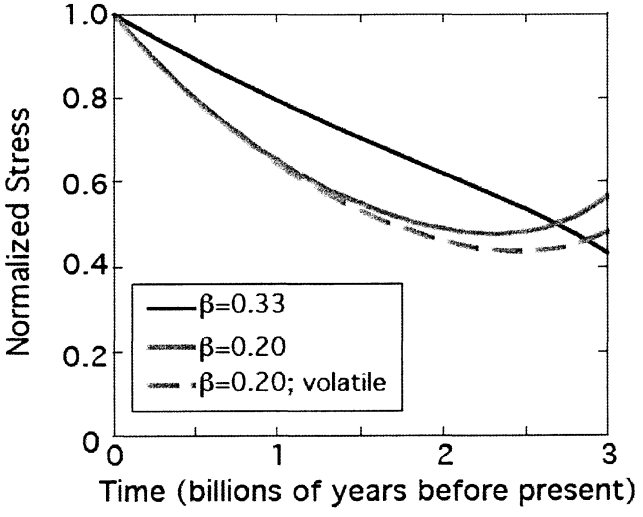

Figure 3.1. Normalized stress evolution from parameterized thermal history models.

A re-evaluation of thermal history constraints, in particular the ratio of present day mantle heat flow to internal heat production, lead to classic thermal history models being questioned (Christensen 1984; Conrad and Hager 1999). Specifically, it was argued that the scaling exponent used in the classic models, i.e., a β value of 1/3, was too high to allow models to match data constraints. In Fig. 3.1 we show that using a lower scaling exponent does not change our qualitative conclusion that convective mantle stress is higher in the modern era than it was in the geologic past.

A factor that could alter viscosity, in addition to temperature, is water. In Fig. 3.1 we also show the results of a thermal history calculation that allows for water degassing and regassing following the approach of McGovern and Schubert (1989). As per that study, mantle viscosity depends on temperature and water content, although for the water dependence we have used a more recent parameterization based on the increased number of rheologic studies exploring the effects of water on mantle viscosity (Li *et al.* 2008). The enhancement of declining stress in the Earth's past, when volatile (water) dependent rheology is included, is due to mantle degassing outweighing regassing during the early evolution of the model. This causes an added stiffening of the mantle over time, which augments that due to mantle cooling. The greater increase of viscosity over time leads to a greater increase in convective stress. This qualitative conclusion was robust for a range of varied model parameters (Sandu and Lenardic 2008) and is consistent with an alternative modeling approach that explored the effects of water cycling on planetary evolution.

Rather then relying exclusively on a parameterized approach, mantle stress levels can also be explored with numerical simulations that directly solve the coupled conservation of mass, momentum, and energy equations associated with mantle convection. Fig. 3.2a shows a

representative simulation. A visco-plastic rheology is employed (Moresi and Solomatov 1998), which permits weak zones to form in regions where a critical yield stress is reached. These zones are model analogs for plate boundaries. They allow the otherwise cold, and hence high viscosity, upper boundary layer to partake in convective overturn and cool the interior mantle. The yield stress for all simulations is set low enough to maintain a plate tectonic-like mode of convection as characterized by the surface velocity shown above the thermal field in Fig. 3.2a.

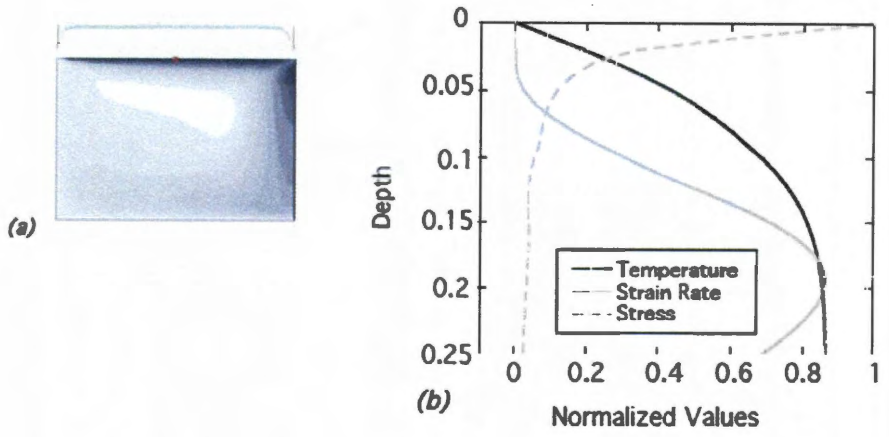

Figure 3.2. (a) Left: Thermal field from a numerical simulation. Dark tones are cold. The light regions in the upper corners of the image signify regions of plastic failure. To make the image, the plastic failure zones where overlaid onto the thermal field and a slight level of transparency was employed. The horizontal surface velocity is shown above the thermal field image. (b) Near surface depth profiles of temperature, the second invariant of the strain rate tensor, and the second invariant of the stress tensor from the simulation of (a).

The numerical code used to solve the model equations (Moresi *et al.* 2003) allows for the tracking of temperature, velocity, stress, and strain rate versus depth profiles. Fig. 3.2b shows representative profiles at the near surface of the modeling domain from the central region of a simulation, i.e., away from plate margin zones. The temperature profiles allow us to track the average thickness of the thermal boundary layer, a model analog of the thermal

lithosphere. An analog of the mechanical lithosphere can also be defined as the region were near surface strain rates are relatively low (Fig. 3.2b). The average stress, over the mechanical and/or thermal lithosphere, can also be tracked. Notice in Fig. 3.2b that the exponential temperature-dependence of mantle viscosity leads to stresses being concentrated in a near-surface stress skin (Fowler 1993). For this reason, we will report averages over the mechanical lithosphere as a measure of mantle convection generated, near-surface stress levels.

Fig. 3.3 shows the effects of increased internal heating on stress levels. The bottom heated Rayleigh number defined for the basal viscosity value is 10^6 and the activation temperature allows for a five order of magnitude viscosity variation across the mantle. The heating ratio is the internal heating Rayleigh number divided by the bottom heating Rayleigh number (Lenardic and Kaula 1996).

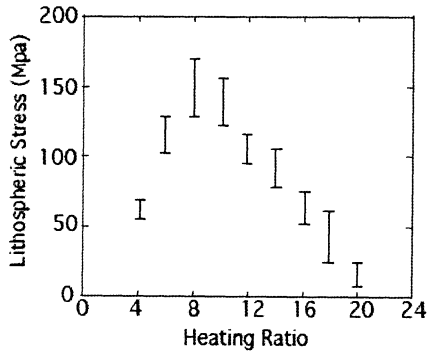

Figure 3.3. Average of the second stress invariant within the mechanical lithosphere from several numerical simulation with variable degrees of internal heating. The range of stress over the temporal evolution of each simulation, after it had reached statistically steady state, is shown.

The simulations were first run to a statistically steady state such that the bulk internal temperature was not increasing or decreasing over time. From there, any individual simulation

was run for several mantle overturns during which stress levels were tracked. The range of average lithospheric stress is plotted for each simulation. To dimensionalize results, the system depth was assumed 3000 km, thermal diffusivity to be 10^{-6} m^2/s, and the surface viscosity to be 10^{27} Pas. Increasing the heating ratio causes the internal mantle temperature to increase and, as a result, the internal viscosity to decrease. This causes velocities to increase. For relative low degrees of convective vigor, the increased velocity dominates in determining the stress scaling (Fig. 3.3 for heating ratios less than 8). However, once the level of mantle convection becomes sufficiently vigorous the reduction in viscosity outweighs the velocity effect and stress levels decrease with increased internal heating. The cross-over occurs at an internally heated Rayleigh number, defined for the viscosity at the base of the system, of $8x10^6$. This is less than estimates of the Earth's present day Rayleigh number (Turcotte and Schubert 1982).

Convective vigor can increase not only by increasing the degree of internal heating but also by increasing the bottom heating Rayleigh number. An increase in the core-mantle boundary temperature in the past, and the associated decrease in basal viscosity, would lead to this. This effect can be modeled in our simulations by holding the surface Rayleigh number fixed and increasing the activation temperature of mantle viscosity (this leads to lower internal and basal viscosity and, hence, increased convective vigor). Fig. 3.4 shows how this affects stress levels in our simulations. The heating ratio is set to 8 for all simulations.

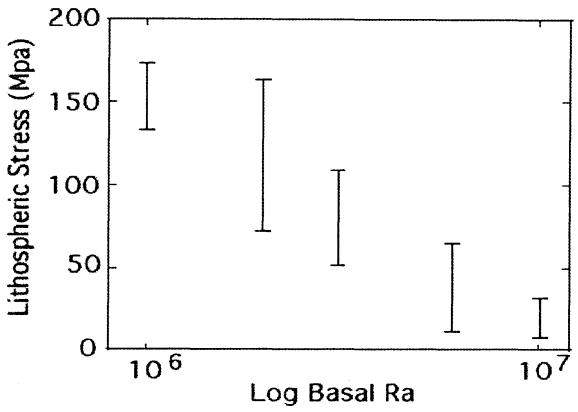

Figure 3.4. Average of the second stress invariant within the mechanical lithosphere from several numerical simulations with variable bottom heated Rayleigh numbers. The Rayleigh numbers are defined for the viscosity at the base of the convecting mantle. The range of stress over the temporal evolution of each simulation, after it had reached statistically steady state, is shown.

Again, the effect of lower internal mantle viscosity dominates the stress scaling and stress levels decrease with increased convective vigor. This qualitative trend was robust for variations of the lithospheric yield stress and it has previously been shown that even in the limit where the yield stress is so high that the mantle convects in a stagnant lid regime, convective stress still decreases with increasing mantle Rayleigh numbers (O'Neill *et al.* 2007c).

Craton to mantle coupling

The previous section argued that mantle stress levels have increased over geologic time. Cratonic lithosphere immersed in the mantle can thus experience enhanced stress but this does not mean it will necessarily deform. Cratons can resist increased deformation potential through their strength associated with a high relative viscosity.

The question of how much greater the effective viscosity of cratonic lithosphere must be relative to the mantle in order to resist deformation has been addressed via an energetic balance argument (Lenardic and Moresi 1999). The essence of the argument was that if the energy that would be dissipated in deforming cratonic lithosphere in the thermally convecting mantle is greater than the energy dissipated in the whole of the mantle, then cratonic lithosphere can be considered effectively non-deformable. This led to a scaling relationship for the critical viscosity ratio between cratonic lithosphere and bulk mantle required to decouple cratons from mantle deformation (mantle convection generated stress would still be transmitted into cratons but deformation, strain rate, would not be). Numerical simulations confirmed the predicted scaling trends and the combined energetic theory and simulations lead to the conclusion that the critical viscosity ratio was between 100-1000. The analysis did not consider the potential that the viscosity of cratonic lithosphere relative to the mantle could increase in the Earth's past due to differential cooling between continents and the bulk mantle.

One factor that can increase the relative viscosity of cratonic lithosphere is dryness relative to the mantle (Pollack 1986). Another factor is temperature, i.e., cooler cratonic relative to oceanic geotherms can increase the relative viscosity of cratonic lithosphere. The temperature difference between cratonic lithosphere and bulk mantle over time depends on the thermal adjustment time of continental lithosphere relative to the bulk of the mantle. The thermal adjustment time of cratonic lithosphere is considerably greater than that of oceanic lithosphere and is comparable to the time scale of secular mantle cooling associated with decaying radiogenic heat sources (Michaut and Jaupart 2007; Michaut *et al.* 2009). Further, a range of numerical simulations and parameterized models (Davies 1979; Ballard and Pollack 1988; Lenardic 1998), together with scaling theory (Lenardic *et al.* 2005; Lenardic *et al.* 2006;

Grigné *et al.* 2007), have shown that the mantle heat flux into continental regions changes slowly relative to total mantle heat flux as convective vigor increases (i.e., the ratio of mantle heat flux from oceanic relative to continental regions increases in the Earth's past). The long thermal adjustment time of cratonic lithosphere and the partitioning of mantle heat flux between continental and oceanic regions over time collectively suggest that the temperature of cratonic lithosphere has changed slowly relative to that of the bulk mantle.

The temperature difference between cratonic lithosphere and the bulk mantle is not the only factor that contributes to its relative strength nor is it likely the dominant factor that provides long-term tectonic stability for many of the Earth's cratons. However, the temperature effect combined with high cratonic viscosity due to dryness and a relatively high yield stress can provide long term stability within a vigorously convecting mantle (Lenardic *et al.* 2003). The differential cooling between cratons and the bulk mantle means that one of the factors that allow cratons to resist deformation, in the face of increasing stress over time, is declining over time. Thus, a change in one of the other factors that contribute to stability, e.g., rehydration of a craton, is more likely to lead to decratonization under modern geologic conditions than it would be under Proterozoic or Archean conditions.

Discussion and Conclusions

Increasing mantle stress over geologic time (Section 2) together with a decreased viscosity contrast between the mantle and deep continental lithosphere (Section 3) favor an enhanced decratonization potential from the Archean to the present. Fig. 3.5 shows results from a numerical simulation suite that supports this conclusion (O'Neill *et al.* 2008). The simulations allow for sections of continental lithosphere to be immersed within a convecting mantle.

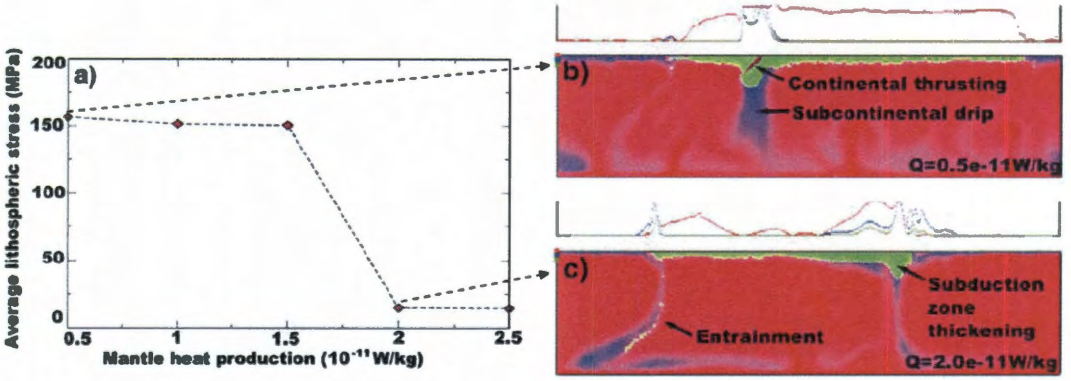

Figure 3.5. (a) Average cratonic stress levels from numerical simulations that allow continental cratons to drift within a convecting mantle. Temperature and composition fields from two of the simulations are shown in (b) and (c) (Continental lithosphere is shown as light green).

The mantle rheology allows for plate like behavior as discussed in Section 2. The rheology of continental lithosphere is of the same form but allows for an increased effective viscosity to mimic dehydration. Laboratory experiments suggest that the maximum viscosity increase between a dehydrated section of lithosphere and hydrated mantle is a factor of 100 (Hirth and Kohlstedt 1996). For cratonic lithosphere the value can be dynamically lowered by rehydration due to, for example, water release from a flat subducting slab below a continent

(Li *et al.* 2008). The strengthening-factor for continental lithosphere in the simulations of Fig. 3.5 is ten, which mimics partially rehydrated lithosphere. For the levels of internal heating appropriate for Archean conditions (Fig. 3.5c), the weakened lithosphere does deform but the level is relatively mild and the lithosphere is not disrupted across its entire thickness. In contrast, under cooler present day conditions (Fig. 3.5b) through-going shear zones form in the continental lithosphere. The cooler conditions are associated with a higher mantle viscosity which leads to greater mantle stress levels and greater stress transmitted into continental sections.

We can summarize our main lines of argument as follows. For so long as the Earth's mantle is in the vigorous convection regime, mantle stress levels will increase with mantle cooling, i.e., with geologic time. Thick sections of continental lithosphere, cratonic roots, have a longer thermal relaxation time than the convecting mantle that will cause temperature differences between the roots and the mantle to decay over time. This will cause a decrease in the viscosity variation between roots and the mantle and an increase in the degree of viscous coupling. Both these factors increase the potential of decratonization over time but are not sufficient to cause instability if cratons are sufficiently dry such that dehydration induced strengthening can resist mantle stresses. Flat subduction below continents can lead to a rehydration and associated weakening of of cratonic lithosphere. The likelyhood that this type of weakening would cause decratonization increases for increased mantle stress and increased root to mantle coupling. The implication is that cratonic lithosphere was more stable in the Earth's past than it is in the geologic present or future (again, for so long as the vigor of mantle convection remains in the relatively high Rayleigh number limit).

For the super continent cycle our arguments suggest that over the most recent cycle of assembly and dispersal, specific cratons may, depending on the level of rehydration they experienced, become unstable. Thus, a generic role for all cratons, in terms of focussing deformation, may not hold and individual cratons may have progressively more unique roles in super continent history. At a larger scale, a changing level of background mantle stress could effect the lifetime of super continents over geologic time. Lower stress levels in the past could allow super continents themselves to remain stable over longer time frames in the geologic past. The specific prediction this leads to is that the time scale between the assembly and dispersal of super continents should be longer in the Earth's past.

Chapter 4

VOLATILES IN THE ATMOSPHERE, THE CLIMATE FEEDBACKS AND THE IMPLICATIONS FOR SURFACE TEMPERATURE

Introduction

The surface temperature of planetary bodies is determined by a multitude of intricate factors of both internal and external origin, and its value is further implicated deterministically in many aspects of a planetary system. At the first sight, its calculation at the entire planetary scale is the normal output of any simple or more complex Global Circulation Model (GCM). Various models are presented and deployed currently to address aspects of the present day climate on Earth and the potential perturbation that can arise from human interaction. A special attention has been paid in recent years to the problem of global warming because of greenhouse gas emissions due to human activity and this problem bolstered the research in many fundamental aspects of climatology. Current interest tends to focus mainly on radiative factors affecting climate and especially on CO_2 as a perturbing element. The problem with such models is that they are not easy transferable to other planetary bodies and is even hard to use them to study past conditions on our planet (Zeebe *et al.* 2009).

Determination of surface temperature is important for understanding the general heat budget of a planetary body. The intensity of mantle convection is affected by the temperature at the surface and convection models always operate with an assumed value on their upper boundary (Schubert *et al.* 1979). The intensity of convection that increases normally with surface being colder is determining the temperature of the interior according to the energy balance condition in the system. A link between surface temperature and the temperature in the interior of the planet is thus established. The climate driven temperature change of the

interior also affects the mantle viscosity and, according to boundary layer theory, the viscous stress that plays a fundamental role in determining the style of global planetary tectonics (Solomon *et al.* 1999). Scaling theories are developed to quantify the temperature variation necessary to trigger transitions in the plate tectonics regimes as a function of the yield stress of the planetary lithosphere (Lenardic *et al.* 2008). A reversed mechanism is also possible, planetary interior is conditioning the surface temperature through convection-related volcanic degassing processes. It is thought that volcanism is responsible for pumping important amounts of volatile in the atmosphere and many of them have the potential of enhancing the surface temperature through the greenhouse effect. A coupled approach to the problem of planetary thermal evolution is therefore desirable, and hence the interest for the climate modeling in the geodynamic perspective (Phillips *et al.* 2001).

In this study, we investigate the factors that are linked to planetary interior and have the potential of changing the surface temperature. We also analyze the feedback relationships among these factors and attempt to quantify the magnitude of these feedbacks. The results will be used to test the long-term climate stability of some terrestrial planets like Earth and Venus and evaluate some hypotheses regarding the early faint Sun paradox as it was defined in Sagan and Chyba (1997).

We used a highly parameterized, grey radiative-convective model that takes the solar flux and the amount of CO_2 in the atmosphere as forcing parameters and the amount of water as being in pure feedback relationship with the surface temperature. The approach is obviously based on several simplifications but the model needs to be robust enough to allow scalability on different planets. In addition to this, more complex multidimensional GCM are not

necessary more suitable to study the fundamentals of global scale climate change and, are too sensitive to uncertain parameterization of sub-grid scale physics (Somerville *et al.* 1974).

The radiative-convective equilibrium in atmosphere has been studied for long time (Manabe and Strickler 1964), but many areas of the problem are still subject to passionate debate even today. The water vapor feedback mechanism for example has been investigated mostly in the context of purely radiative forcing induced by the increasing of the CO_2 in the atmosphere (Doherty and Newell 1984; Raval and Ramanathan 1989; Kasting 2005a). Most of the problems arise when attempting to describe the water vapor distribution in atmosphere. A very common formulations is to assume a fixed humidity distribution (Manabe and Wetherald 1967) and use it to determine the radiative temperature equilibrium profile. Such formulation however prevents much water vapor feedback to be included in the system aside from the strict dependency of the maximum vapor pressure on the temperature. It was also noted that the feedback mechanisms should allow for the temperature gradient change (Held and Soden 2000), and this is normally a function of humidity profile variation.

The model parameterization

Overview

The model employed in this study is a highly parameterized, 1D vertical, coupled energy-mass balance model. It calculates the vertical distribution of temperature and several other variables like the water vapor distribution. The composition of the atmosphere consist of five components: three greenhouse neutral components (N_2, O_2, and Ar), and two greenhouse active components (CO_2 and H_2O) in variable quantities. The concept of coupled mechanism is applied to the water vapor present in the atmosphere since this amount is conditioned by the

temperature, derived from the energy balance and in turn, it affects the energy balance, as water vapor is a powerful greenhouse gas. Water also affects the convection in the atmosphere as the processes of evaporation and condensation alter the equilibrium temperature lapse rate.

Since the model is designed to study the planetary evolution on a long scale, the R-C model computes the most probable thermodynamic equilibrium state of the climate, regardless of the path to reach that state. However, it should be noted that in reality the climate is never in equilibrium but we promote this concept to quantify the global average values for the parameters we solve, considering that the system always move toward this equilibrium state. In addition, this approach provides us with the necessary assumption required to apply several parameterizations used in the model. Otherwise this state could be computed asymptotically from an initial value condition (Manabe and Strickler 1964). The radiative-convective equilibrium state is defined as the statistical equilibrium condition that establishes in the global atmosphere in the absence of large-scale dynamical forcing although interaction between these two components can produce fluctuations of this condition (Randall *et al.* 1994). Baroclinic instability can also divert the system from equilibrium by moving air and moisture laterally even before a vertical equilibrium is established. Physically, an atmosphere in local thermodynamic equilibrium (LTE) implies that the variation of net heat flux with altitude is null:

$$\frac{d\Phi_{net}}{dz} = \frac{d(\Phi_{up} + \Phi_c - \Phi_{down})}{dz} = 0$$

where Φ_{net} is the net IR flux, Φ_{up} is the upwelling IR flux, Φ_c is the convective flux, and Φ_{down} is the downwelling IR flux. The radiative fluxes can be retrieved by numerically

integrating the Schwarzschild's equation or by using analytical expression for each component (Lorenz and McKay 2003). The flowchart of the model calculations is presented in Fig. 4.1.

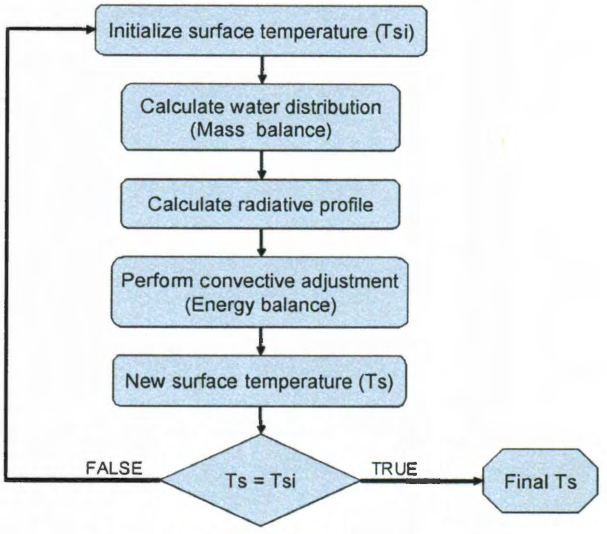

Figure. 4.1 Flowchart of the model calculations. The computation scheme consists in assuming an initial value for the surface temperature and performing an iterative test on the final value after each step of energy and mass balance calculations. The final solution is determined when the difference between initial and final value fall within a predetermined error interval.

The two main components of R-C climate system are the radiative equilibrium profile and the convective adjustment. The two are in a closed relationship since they share several parameters regardless of the solution chosen to solve them. Our approach is to solve the radiative profile for a predefined adiabatic convective profile, and then recalculate the new equilibrium adiabatic profile until they coincide. Numerically, this involves solving for the equilibrium profile using the common parameters resulted from the radiative balance calculation and initial surface temperature assumption. The new surface temperature is then compared with the initial one and the loop is repeated until the difference falls bellow a predefined value, usually 0.2 K that represents the precision of the model. The scheme is

convergent for normal climate, i.e. no runaway greenhouse condition is initiated. In the case of runaway divergent condition, the model performs the calculation until all the water available at surface is consumed into the atmosphere and the greenhouse effect is thus stabilized. The convection algorithm uses an energy balance model to perform the surface temperature adjustment and calculates the temperature profile using a predefined temperature gradient. Since the water vapor condenses in the process altering the energy balance, a correction is applied by using a moist adiabatic gradient instead of the dry adiabatic gradient. The temperature profile is represented therefore by the unique solution of the integral of the energy balance equation.

Radiative equilibrium

For the simple, grey, radiative-convective model and clear sky condition the equation of radiation transfer in the atmosphere has been solved analytically using a two stream approximation (Eddington approximation) and showed little difference from the exact solution (Goody and Yung 1989). This parameterization resolves the radiative temperature profile in atmosphere as a function of optical thickness by constraining outgoing long wave net flux at the top of the atmosphere to mach incoming shortwave solar net flux as a boundary condition. However, the solution presents a temperature discontinuity at the surface-atmosphere interface since the surface emits radiation only upward whereas any of the atmospheric layer emit in both directions. Like many authors, we ignored this discontinuity assuming that in a convective, moist atmosphere convective mixing and surface evaporation rapidly annihilate it. The radiative temperature profile thus becomes:

$$T_r(z) = \sigma T_e^4 \left(\frac{1}{2} + \frac{3}{4} \tau(z) \right)$$

where τ represents the optical thickness frequency integrated over infrared domain, σ is the Stefan-Boltzmann constant and T_e is the effective radiating temperature corresponding to planetary averaged incoming solar flux and specific albedo. In the atmosphere, the upwelling and downwelling radiative fluxes are calculated by integrating the radiative intensity over the two semispherical domains. As stated earlier, because of thermodynamic equilibrium condition, the divergence of the flux is zero at any altitude. At the top of the atmosphere, the heat flux leaving the planet needs to conserve the total planetary radiation budget. For the grey model, this implies the frequency integrated source function (Stefan-Boltzmann) should mach the incoming surface received shortwave radiation flux. Some authors use the incoming shortwave radiation flux as a free parameter to calibrate the model at a given surface temperature (Lindzen *et al.* 1982; Kasting 2005a). The incoming radiation depends on the solar constant for the planet's orbit and the planetary albedo. For the Earth this value inferred from satellite observations is about 1366 W/m^2 and the planetary albedo is about 0.3. The net flux at the surface is then about 240 W/m^2 , value averaged over the entire surface of the planet (Stephens *et al.* 1981). The above-mentioned equality applied for Earth condition give T_e = 254^K. The radiative energy budget thus vanishes relative to this temperature baseline at infinity:

$$\int_0^\infty \rho_a(z) c_p (T_r(z) - T_e) dz = 0$$

where ρ_a is the air density, c_p is the dry air heat capacity and z is the altitude. An effective radiating temperature is calculated for any planetary condition as:

$$T_e = \left(\frac{S_0(1-A)}{4E_s\sigma} \right)^{\frac{1}{4}}$$

where S_0 is the solar constant, A is the planetary albedo and E_s is the surface emisivity (usually equal to 1). In addition to this, at the top of the atmosphere we can define the skin temperature as:

$$T_0 = 2^{-\frac{1}{4}} T_e$$

These two values are important parameters that characterize the radiative condition of the planet since they are independent on the optical thickness of the atmosphere.

Optical thickness

The radiative balance equilibrium temperature is subsequently calculated as a function of the optical thickness of the atmosphere. The optical thickness of the atmosphere τ at any point of altitude is a measure of the amount of radiation that is absorbed (or scattered) by the layer of atmosphere between that point and a point situated at the top of the atmosphere where the air is thin enough to consider $\tau = 0$ measured along the vertical path ds. Resulting from integration of the Beer-Lambert law, the optical thickness is linear with the density and for the grey atmosphere (Wildt 1966; Sagan 1969) is calculated as:

$$\tau = \int_{s=z}^{\infty} \kappa \rho(s) ds$$

where κ is the mass absorption coefficient of the absorbing medium, and ρ is its density. An analytical solution for this integral is obtained for hydrostatic distribution of pressure with constant equivalent scale height (isothermal atmosphere) by solving the above integral assuming an exponential decay of density (pressure) with altitude z. For our two-component system, the optical thickness becomes:

$$\tau(z) = \frac{1}{T(z)}\left(\frac{\kappa_{CO2}}{R_{CO2}} P_{CO2} e^{-\frac{z}{H_{CO2}}} + \frac{\kappa_{H2O}}{R_{H2O}} P_{H2O} e^{-\frac{z}{H_{H2O}}}\right)$$

where T is the temperature at altitude z, κ_{CO2} and κ_{H2O} are the mass absorption coefficients for CO_2 and H_2O respectively, P_{CO2} and P_{H2O} are the partial pressures of CO_2 and H_2O at the surface, H_{CO2} and H_{H2O} represent the pressure scale height of the two components, and R_{CO2} and R_{H2O} are the specific gas constants for carbon dioxide and water respectively.

For the normal non-grey planetary atmosphere the temperature structure are usually resolved by calculating the net infrared fluxes for each of the small frequency intervals in which the infrared domain is divided. The net infrared flux is then obtained by integrating the monochromatic flux distribution over the entire domain (Pollack 1969b; Pollack 1969a). Current databases exist that contain all the parameters required to compute the observed peaks in the absorption spectra for each individual components (Rothman *et al.* 2009). Several models have been proposed to parameterize the absorption function (Vardavas and Carver 1984; Chou 1992) in the infrared domain, as well as for incoming solar radiation (Lacis and Hansen 1974). It is also known that aside from the individual band absorption, a pressure induced continuum absorption also exist especially for the water vapor component (Roberts *et al.* 1976; Barton 1991). A grey atmosphere assumes that the equivalent mass absorption coefficients produce the same net flux distribution in the atmosphere. Since their values are not derived from integration over the spectral domain, we assign their value from calibration of the total radiative flux.

The convective adjustment

Application of the first law of thermodynamics to a parcel of air that moves vertically through an atmosphere found in hydrostatic equilibrium gives the dry adiabatic lapse rate (DALR) as follows:

$$\Gamma_D = \frac{g}{c_p}$$

where g is the acceleration of gravity. This represents the rate of change of temperature with altitude characteristic to atmospheres with no condensable components. In the case when such a component is present, like is the case for water on Earth, the latent heat resulted from condensation of vapors present in atmosphere alter the adiabatic condition of the ascending air. By rewriting the first principle and integrating the Clausius-Clapeyron equation it can be shown (Curry and Webster 1999) that the lapse rate in a moist atmosphere become the Moist Adiabatic Lapse Rate (MALR):

$$\Gamma_M = \frac{dT}{dz} = \Gamma_D \frac{\left(1 + \frac{\lambda_{wv}\mu}{R_{air}T}\right)}{\left(1 + \frac{\lambda^2{}_{wv}\mu}{c_p R_{H2O} T^2}\right)}$$

where λ_{wv} is the latent heat of vaporization for water, μ is the average specific humidity (water vapor mixing ratio) at the surface, R_{air} is the specific gas constant for the air and T is the temperature of the air in the parcel. We used here the term "moist adiabat" that refer to a wet atmosphere but still unsaturated. The reason is to make distinction between a moist profile that has a constant average lapse rate based on unsaturated humidity profile and the saturated

adiabat that is derived from a profile that assumes saturation at any point and referred by most authors as "Saturated Adiabatic Lapse Rate" (SALR). Since the specific humidity for the saturation profile is variable with altitude due to water vapor pressure scaling differently with altitude than dry air, results that saturated lapse rate varies also with altitude. For the present Earth atmosphere, the average lapse rate that yields from this formula is about 9.8 K/km for DALR and 6.6 K/km for SALR. Some R-C models use a fixed lapse rate in calculation and most of the time is the saturated lapse rate. This parameterization has been compared with observed data for one or both hemispheres (Somerville *et al.* 1974; Yang and Smith 1985) and found in good agreement, although discussion can be done regarding whether the saturated value is suitable to characterize the whole atmosphere.

The conventional method to apply a convective adjustment is derived from a stability analysis of the air motion relatively to a critical lapse rate. A correction is usually applied whenever the radiative profile exceeds the critical lapse rate, which is typically taken as the DALR or SALR. Since the radiative temperature equilibrium profile produces a variable potential temperature with altitude, the convective stability is considered established when mixing of the atmosphere in the convective region produces an uniform potential temperature (Ramanathan and Coakley Jr. 1978).

Our convection scheme is based on the assumption that along the vertical atmospheric profile the energy balance is conserved, since the process itself only redistributes the heat and there are no sources or sinks of heat in the atmosphere. Since condensation of water vapors does create a source of heat, by using the moist lapse rate instead of dry lapse rate it should include the adjustment. The convective movement removes heat from the lower atmosphere and deposits it in the upper troposphere but conserving the total heat in the system (Fig. 4.2).

The integral of the energy on the vertical profile for a specific adiabatic gradient thus vanishes at the tropopause:

$$\int_{z=0}^{z=Z_{tropo}} \left(\rho c_p (T_r(z) - T_{rc}(z))\right) dz = 0$$

where $T_r(z)$ and $T_{rc}(z)$ are the temperatures as a function of altitude for radiative (R) and radiative convective (R-C) equilibrium respectively, and Z_{tropo} is the height of the tropopause. The troposphere is then defined as the atmospheric layer in which convection occurs, and delimited between surface and the tropopause level. In order to solve numerically for the integral a boundary condition is required, and this is taken as the temperature continuity condition at the tropopause:

$$T_r(Z_{tropo}) = T_s - \Gamma_M Z_{tropo} = T_{rc}(Z_{tropo})$$

where T_s is the temperature at the surface.

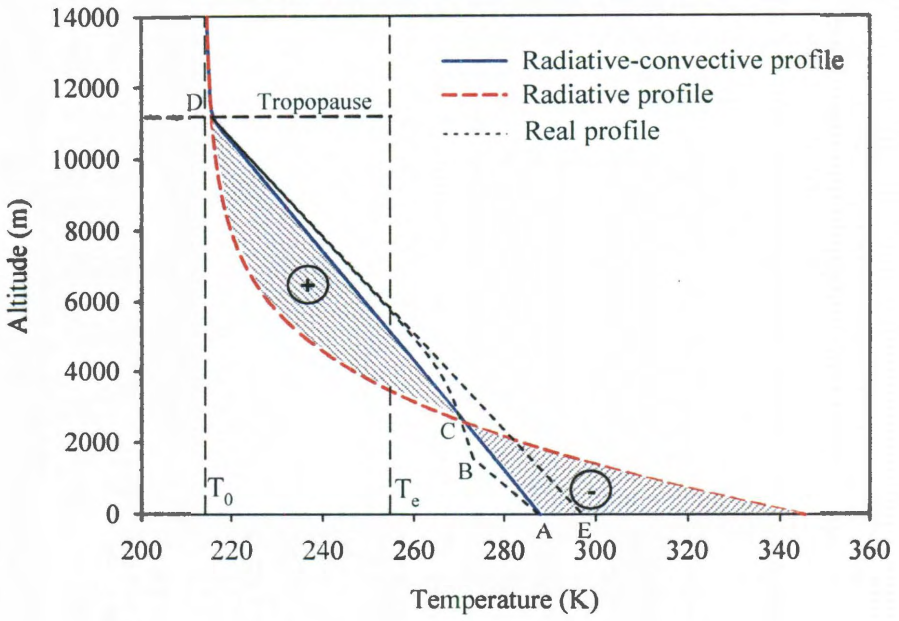

Figure 4.2. Radiative and convective profiles for Earth Atmosphere. The A-B-C-D-E trajectory represents the transformation suffered by a parcel of air as is circulated by convection.

This scheme proves to be very stable too. If, for example, a forcing element attempt to displace the profile to the right by increasing the surface temperature without changing any radiative parameter, then this would result in lifting of the tropopause level, increasing the convective motion and cooling back the surface. Our scheme would become unbalanced by extending the negative area and the solution would be searched to the left (at lower temperature). The reverse is happening when the forcing is pushing the system to the left with the solution being sought to the right.

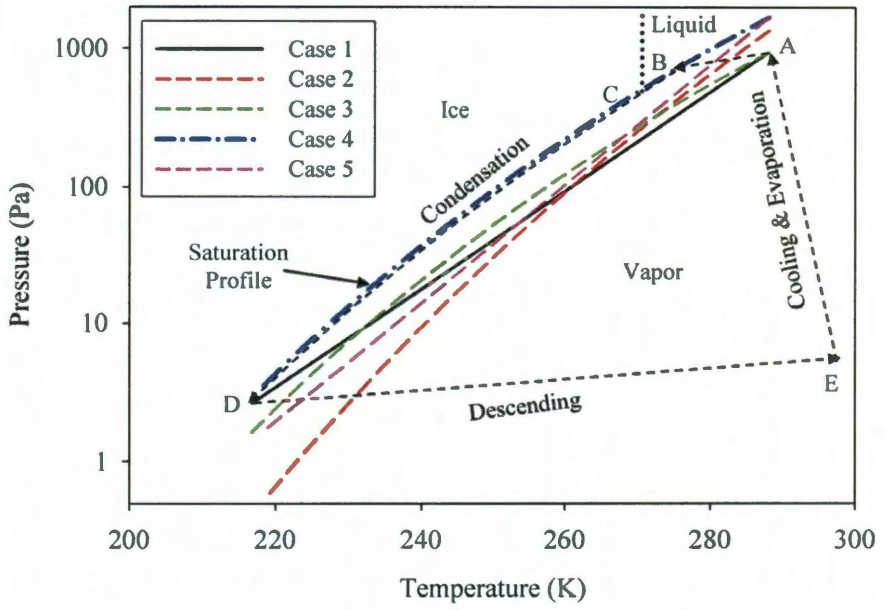

Figure 4.3. Different scaling parameterization for water vapor distribution in atmosphere. Case 1: fixed scale (current model); Case 2: Fixed profile (Manabe, S. and R. T. Wetherald (1967)); Case 3: Fixed relative humidity – 50%; Case 4: Fixed Relative humidity – 100% (Kasting, J. F., J. B. Pollack, et al. (1984)); Case 5: Scaled specific humidity (Sellers 1973; Stephens and Greenwald 1991). Dashed line represent the transformation of the air parcel as it is circulated by convection.

Since the convective profile is just a statistical average as defined early then the real motion of the parcel is slightly different. In Fig. 4.2 the thin dashed line show an example of a real trajectory of an unsaturated parcel as it is circulated by the convective movement. The translation from point A to point B is forced along a dry adiabat until saturation condition occurs (point B known as the Lifting Condensation Level). From that point the lifting is happening along the saturation profile B-D (see Fig. 4.3 for the same circuit in P-T coordinates) and at point C the convection become free (Level of Free Convection) as temperatures from that point exceeds those of surrounding air (A-D adiabat) and thus lower density assures the lifting force (Zdunkowski and Bott 2004). From D the parcel descends

along the dry adiabat and reaches the surface in point E, hotter than it left because the differences in potential temperature between dry and saturated adiabat. The excess heat is resulted from latent heat of condensation, so as the parcel moves horizontally the evaporation process absorb the excess heat cooling the parcel and raising its humidity content along D-A line. From A, the cycle is repeated and as long as the unstable C-D region is present, the convective motion is sustained.

Water vapor distribution

Water vapors in the atmosphere causes the largest natural greenhouse effect (Houghton 2005) and therefore its amount and distribution is extremely important for the radiative energy balance. Uncertainties associated with humidity values and distribution can inflict about 1-1.5% inaccuracy in calculated outgoing radiance at the tropopause level (Gutzler 1993), comparable with the effect equivalent to doubling the CO_2 in the atmosphere. However, it is difficult to estimate the amount of water vapors in the atmosphere, and the parameterization of the water vapors effects on climate it is still under development. In general, for a well-mixed gas found in hydrostatic equilibrium in an isothermal atmosphere the pressure scales exponentially with altitude:

$$P_X(z) = P_{X0} \exp(-\frac{z}{H_X})$$

where $P_X(z)$ is the partial pressure of the component X at altitude z, P_{X0} is the pressure at a predefined level (usually $P_{X0} = PX(0) =$ surface pressure of component X), and H_X is the scale height of component X. From the hydrostatic balance equation and ideal gas law the scale height is:

$$H_X = \frac{R_X T}{g}$$

with R_X the specific gas constant, T is the isothermal temperature (taken in general as surface temperature). The scale height for CO_2 is about 5 km and for the whole atmosphere is about 7 km. If water vapor would move in a dry zone (below the saturation pressure) then we would be able to predict its distribution using the same formula, and its distribution would scale with altitude at about H_{H2Odry} = 12 km like is the case of some hot and dry planets (Venus for example). However, conditions in the Earth atmosphere where liquid water (or ice) is present at surface in equilibrium with the vapors display a different distribution with altitude than in total vapor condition, scale height being reduced to about 2 km. The reason for this reduction resides in water lost to condensation during the convective motion, as the raising unsaturated air parcel reach the maximum vapor pressure line and start condensing back the water to surface. The first estimate we can make is that its distribution with altitude is best calculated from the saturation profile. However, since convective motions mixes air both vertically and laterally, the fully saturated condition are rarely met so other relation must be sought to better approximate the vertical humidity profile. Although this profile is highly required to solve accurately the radiative balance in atmosphere, the condensation process is happening through a rather complicated mechanism and an analytical solution is difficult to predict. A qualitative observation we can make is that most of the water vapor in the atmosphere is concentrated in the lower part of the troposphere, air at high altitudes being highly depleted in moisture.

Empirical relations have been used by several authors to describe the humidity profile and used to calculate the convective adjustment for simple or more complicated models. Some

of them used fixed relative humidity profile that scales with total atmospheric pressure using a relation introduced by Manabe and Wetherald (1967). Although this represents the actual observed average profile, it has no physical support and is thus difficult to transfer to other planets or include it in highly variable models. Other approach was to assume a complete saturation for some interval (Kasting 2005a), relation based on physical properties of water and suitable to study hot and moist planets but not relevant for current conditions on Earth for example since 100% saturation would imply the absence of convective mixing. Finally, a model that describes the vertical profile of specific humidity as a simple power law that scales with total pressure has been used in several climate models (Sellers 1973; Stephens and Greenwald 1991; Zhou and Cess 2001). This is also subject to the same drawbacks as in the case of the fixed relative humidity profile. All of them could also yield problems when surface available water dries up and the atmosphere become depleted in water, although total pressure still does not change.

In order to overcome some of the problems mentioned earlier we used a scaling that confers more flexibility in terms of temperature variation and availability of water:

$$H_{H2O} = \frac{T_s - T_0}{\Gamma_M \log\left(\frac{P_{H2O}(T_{tropo})}{P_{H2O}(T_s)}\right)}$$

where T_s is the temperature at surface, Γ_M is the moist adiabatic lapse rate, $P_{H2O}(T_{tropo})$ is the vapor pressure at the tropopause (equal to saturation pressure at that same level), and $P_{H2O}(T_s) = P_{H2Os}$ is the vapor pressure at surface. This relation also satisfies the continuity

condition at the tropopause, since it reaches saturation at that level and since the stratosphere above is considered in saturation state. The distribution of partial pressure of water vapors with temperature is depicted in Fig. 4.3 along with the previously mentioned alternative scaling. The pressure-altitude and temperature-altitude relationship are derived from the corresponding scaling for pressure and temperature distribution respectively. Table 4.1 presents also different parameters obtained by running the model using each of these parameterizations along with the calibrated value for κ_{H2O} required by each run to obtain the same surface temperature. Results varies significantly, usually all other parameterizations providing more water to the atmosphere than our standard case (Case 1) requiring in turn to chose a lower value for κ_{H2O}.

Param	κ_{H2O}	P_{H2Os}	rh_s	H_{H2O}	Γ_M	Z_{tropo}	$M_{WVtropo}$	$\mu_{WVtropo}$	Reference
Case	*(cm²/g)*	*(Pa)*		*(m)*	*(°K/km)*	*(km)*	*(kg/m2)*	*(kg/kg)*	
Case 1	2.88	938	0.5	1871	6.47	11.2	13.8	1.37	Current model
Case 2	2.68	1350	0.8	1600	5.79	12.7	19.5	1.69	Manabe, S. and R. T. Wetherald (1967)
Case 3	2.54	938	0.5	1815	6.47	11.3	15.9	1.58	
Case 4	1.13	1687	1	2191	5.37	13.4	34.5	2.95	Kasting, J. F., J. B. Pollack, et al. (1984)
Case 5	1.91	1687	1	1870	5.37	13.6	24.7	2.04	(Sellers 1973; Stephens and Greenwald 1991)

Table 4.1. Results of the test runs.

Since any distribution profile represents a statistical average, the transformation suffered by an air parcel as it is cycled by the convective movement is more complicated in reality, and Fig. 4.3 display the same real convective cycle of a moving parcel as depicted in T-ζ coordinates in Fig. 4.2.

Model assumptions and calibration

Parameterization of the radiative properties of the atmosphere employed by the current model does not include a component that addresses the cloud physics. Although clouds are important for the radiative balance of a planet, their modeling and net feedback effect are still controversial issues. We chose instead to use the albedo parameter as a mean to test different conditions that would be affected by cloudiness. Among the five-component atmosphere we assumed, the one that is missing is ozone and this is relevant for the Earth radiative balance. However, it is not present in any other planet we know in significant quantity. Methane is also absent but since we are mostly interested in studying water vapor feedbacks we can substitute methane by assuming more CO_2 instead.

As mentioned earlier, the radiative parameters κ_{CO2} and κ_{H2O} need to be evaluated from calibration points. A two-point calibration would be sufficient unless temperature dependence is also considered. Since Venus presents a high surface temperature condition compared to Earth, it would be impossible to model Venus atmosphere using the same value of mass absorption coefficients as in the case of Earth. Absorption coefficients have the properties of increasing with both partial pressure of the gas itself (self broadening) and atmospheric pressure overall generated by the increased collision among molecules, and a inverse dependence on temperature (Bignell 1970; Kuhn *et al.* 2002; Aldener *et al.* 2005). A linear negative dependence of absorption coefficients on temperature has been used. Since we focus primary on those effects on convection in the atmosphere most of the conclusions refer to the troposphere, assuming a simple asymptotic temperature layer above the troposphere. The short wave heating and the ozone layer in the case of Earth was ignored. The model was calibrated by solving for the absorption coefficients of CO_2 and H_2O vapor first by setting

the model to give 288^{K} at surface with 300 ppm CO_2 and a relative humidity of 0.5 (standard condition) and then by requiring that surface temperature increase with 1.2 K for doubling the amount of CO_2 (Hansen *et al.* 1981). The temperature dependence was linearly extrapolated as to intercept Venus 735 K surface condition with 90.1 bar CO_2 and a relative humidity of 0.0001 in absolute mass ratio.

The water vapor feedback and climate stability

Importance of the chosen model

When studying the feedbacks relations of any complex system like climate it is important to be able to quantify the effect of any factor independently from each other. Observational data would be less significant without suitable methodology that permits deconvolution of the mechanisms that produced the overall result, and more important when a model is set up to provide predictions about future evolution of the system. Feedback relations are analyzed in this study on forward modeling approach with a definite level of simplification in order to enable us to focus on certain aspects of the water vapor feedbacks in relation with the temperature change of the planet's surface.

The model introduced by Manabe and collaborators (Manabe and Strickler 1964; Manabe and Wetherald 1967) addressed the nonradiative component of upward fluxes by constraining the lapse rate to remain below a predefined value. As observed from their lapse rate parameterization, this is affected by the vapor-mixing ratio and consequently we expect that tropospheric lapse rate varies with temperature since humidity varies also with temperature. In order to understand the feedback effects the model employed here addresses this variation. The convective parameterization maintains only the energy balance fixed but

otherwise it allow the lapse rate to vary freely correlated with the humidity content parameters and indirectly with other factors that affect them.

Density distribution and self-inflicted temperature feedback effect

Before we attempt to asses the feedback effect resulting from changes of the amount of water vapor in the atmosphere because of temperature variation, we considered first the feedback effect of water vapor and other greenhouse gases distribution variation with temperature. We run the Earth model for two extreme different temperatures of 288 K and 388 K (just as present day temperature of Earth would forcibly be increased by 100 K). First, we run a reference case that reproduces standard Earth condition with CO_2 = 300 ppm, and P_{H2O} = 900 Pa, calibrated for temperature at the surface = 288 K. Then by increasing the surface relative humidity, we let just enough water in the atmosphere so that the new equilibrium temperature at surface becomes 388 K. Finally, we kept the surface temperature at this level and we forced the partial pressure of water back to its initial value of 900 Pa, but we preserved the scaling (distribution lapse rate) from its 388 K level in order to separate the virtual effect of scaling only.

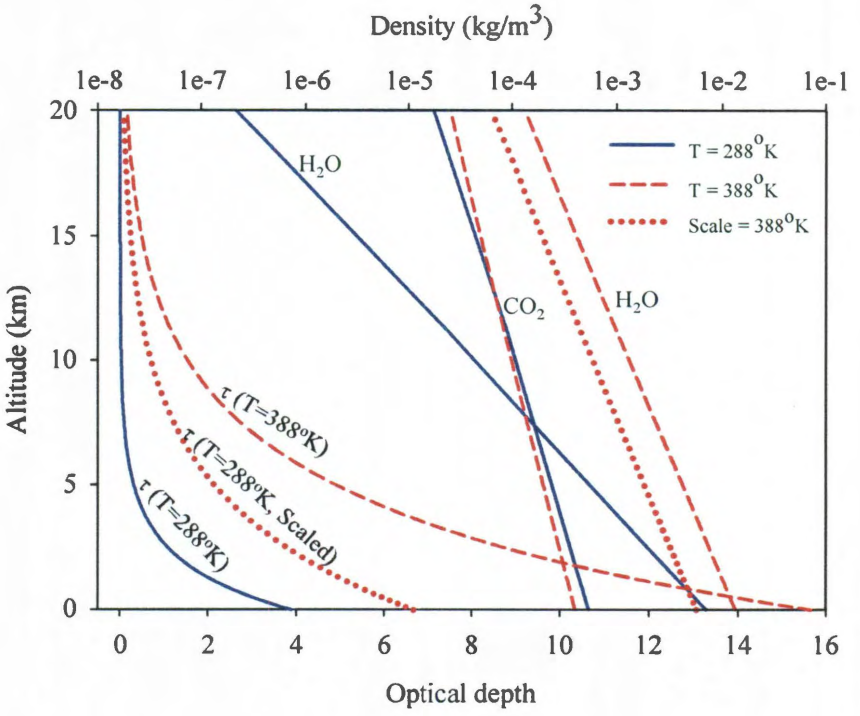

Figure 4.4 The effect of temperature increase on the distribution of greenhouse gases in atmosphere and the consequence on the infrared optical thickness profile.

The results presented in Fig. 4.4 depict the density profiles for these runs and the corresponding variation of the optical depth for each case. For a normal dry gas, like CO_2 in our case, a change in temperature will tend to redistribute the pressure and mass according to the scaling law presented earlier. Since pressure at the surface does not change in order to conserve the total mass, an increase in temperature would reduce the density of gas near surface but the distribution in altitude would follow a much gentle slope (decrease slower with altitude). In the case of condensable gas, like water vapor the pressure and density increases with temperature since the saturation pressure increase in the same direction but also the scaling increase too, and this was the case in the second test run. In the last test we subtracted the effect of the pressure increase so the water vapor display a pseudo-dry distribution effect

with density decrease near the surface and being redistributed in altitude. In any case, the overall effect would be the redistribution of the radiative absorption source in altitude. Although the convective mixing will moderate the extremity of the effect, this redistribution would cause the atmosphere to increase the infrared emission at higher altitude where it is colder. In order to balance the flux, the surface temperature needs to increase. Using the Stefan-Boltzmann relation, this corresponds to an additional 4.5 W/m^2 for each 1 K temperature increase. The corresponding infrared optical depth curves also shift to the higher values as the atmosphere become thicker in altitude. This self-inflicted feedback is a result of temperature increase alone regardless of the forcing element that leads to this raise. It is therefore included in the overall feedback effect.

Atmospheric composition and change in heat capacity effect

An increase of the amount of a greenhouse gas other than water is expected to alter the radiative balance and increase the surface temperature. A positive feedback effect between water vapor and temperature would lead to an increased amount of water vapor in the atmosphere too. Aside from this effect, it would be interesting to consider what other implications the increase of dry greenhouse component would have for the water vapor mass. The total amount of precipitable water in the atmosphere (water vapor content) is given by integrating the average mixing ratio with altitude. Since the water is lost in the precipitation process as it is moving upward by convection, it is expected that the total amount of water that is left in the troposphere be somehow conditioned by the amount of water lost to precipitation. In order to determine the amount of water lost we have to integrate the mixing ratio variation with altitude multiplied by the amount of dry air in the parcel. As a parcel of wet air is displaced upward, it follows an adiabatic transform and latent heat is released as the water

condenses out of the vapor in the parcel. Theoretically, by writing the first principle it is possible to define the amount of water lost in this process:

$$d\mu_w = \frac{c_p dT - gdz}{\lambda_{wv}} = \frac{c_p}{\lambda_{wv}}(\Gamma_D - \Gamma_M)dz$$

where $d\mu_w$ is the mixing ratio variation. We tested the model by increasing the amount of CO_2 from the reference point of 300 ppm to 3000 ppm but forcing the surface temperature to stay the same in order to disregard the temperature change effect, and isolate the composition effect only. The results presented in Table 4.2 display a small variation but the trend is toward reducing the amount of water in the troposphere. This is caused by two facts that act simultaneously. First is the result of adding more dry mass to the atmosphere. The mixing ratio of water drop as drier component is added and the overall precipitated water increase since it scales with the total dry amount in the parcel. The second effect is that it changes the average heat capacity of atmosphere and consequently the lapse rates. Since CO_2 has a heat capacity smaller than that of average atmosphere (for Earth-like conditions), then it will reduce the average atmospheric c_p and consequently increase the lapse rates. This means that a parcel will experience a higher temperature variation per altitude gain and consequently there will be more water condensed and removed from the parcel volume. The atmosphere is therefore drier and this is expressed by lower optical thickness of water column at surface. Normally this would produce a small cooling effect but a steeper lapse rate will move the convective equilibrium toward higher surface temperature and this would compensate somehow the radiative effect. For small variation in greenhouse component, the effect could be therefore neglected, but when large amount of greenhouse gas is added to the system (like a simulated evolution from Earth-like climate conditions to Venus-like conditions), it could be

significant as the imbalance between convective and radiative components deepens. In addition, such a transformation would pose even more complexity since the CO_2 heat capacity is highly variable with temperature. For the Venus-like conditions for example it could record the reverse of the above effect since at some point would become higher than the atmospheric average c_p.

c_{CO2} (ppm)	DALR (K/km)	MALR (K/km)	H_{H2O} (km)	M_{H2O} (kg/m^2)	μ_{H2O} (g/kg)	M_{H2O} prec (kg/m^2)	M_{H2O} prec ct LR (kg/m^2)	τ^{H2O}_{surf}
300	9.669	6.475	1871	13.843	1.328	2.8645	6.1594	3.871
3000	9.671	6.483	1869	13.826	1.322	2.8650	6.1666	3.866

Table 4.2. Parameters of the pure temperature feedback effect.

From Table 4.2 also is important to observe the large difference between the amount of water required to precipitate in order maintain the observed lapse rate, and the amount of water precipitated by using that lapse rate. The discrepancy is caused by the assumption we made (like most of the authors that used 1D models) that the lapse rate is constant with altitude. Since we were interested only in the amount of precipitable water that affects the radiative balance the assumption was acceptable. However, in order to balance the whole amount of water cycled through the convective motion a model that employ a full hydrologic cycle is required (Ramanathan 1981; Rennó *et al.* 1994). An important observation here is that water extracted from vapor phase is assumed to precipitate to surface, and does not contribute to radiation balance any more since the model does not implement any cloud parameterization. However, in reality the condensed water can form clouds, which in fact do contribute to the radiation balance (Lindzen *et al.* 1982); and since rain can re-evaporate before reaching the

surface, the radiative effect of water may be underestimated, unless we assume that the cloud-albedo effect balance it.

Feedback definition

The overall feedback effect of the water vapor is of paramount importance for determination of the stable equilibrium temperature. As we defined early, the equilibrium surface temperature is attained when the amount and distribution of water in the atmosphere generates the exact amount of heat flow at the top of the atmosphere to balance the incoming solar energy. This balance is complicated by the fact that water eventually crosses the phase boundary limits and absorbs or release heat in the convective process fact that alters the adiabatic lapse rate. Convection in the atmosphere is sustained by the temperature difference between the hot surface and cold upper atmosphere providing the lapse rate of the purely radiative equilibrium is steeper than the adiabatic one. The convective process itself controls the amount of water through the hydrologic cycle and hence the feedback effect is established. If an equilibrium point defined by a pair of $(T_{s0}, P_{H2O}(T_{s0}))$ is attained it is assumed that the climate would continue to remain in that point indefinitely as long as the forcing elements are constant. When any forcing element displaces the climate from this equilibrium with an amount ΔT_{force} then the new surface temperature become:

$$T_{s1} = T_{s0} + \Delta T_{force}$$

Since the new temperature is not characterized by the same amount of water vapor $(P_{H2O}(T_{s0}))$ the vapor pressure changes and raise the temperature further (positive feedback effect) adding its elementary feedback factor f_{H2O} :

$$T_{s2} = T_{s1} + f_{H2O}\Delta T_{force}$$

This situation repeats iteratively and the overall gain is then:

$$\Delta T_{feed} = \Delta T_{force} \sum_{n=0}^{\infty} f_{H2O}^{n} = \Delta T_{force} \frac{1}{1 - f_{H2O}}$$

From this relation is evident that f_{H2O} has to be less than 1 for the series to converge otherwise the runaway condition is established. However, the real value of f_{H2O} is probably the most debated aspect in climatology, and an analytic relation for its parameterization is difficult to derive due to the multitude of factors that contribute additively to the overall result (Lindzen 1994).

Water vapor content and radiative-convective feedback

We assessed the equilibrium condition for different levels of forcing element by running the model with a fixed set of CO_2 amount of in the atmosphere of Earth-like planet and recording the equilibrium points for variable amount of water vapor (Fig. 4.5). The CO_2 for each run was 300, 30000, and 300000 ppm. The partial pressure of water vapor at surface was gradually increased and the resulting equilibrium surface temperature for each run was obtained. In Fig. 4.5 along with the surface radiative-convective equilibrium temperature, also plotted was the radiative equilibrium temperature. This is not a real measurable temperature in a convective atmosphere but a theoretical one, and signifies what would be the surface temperature in the absence of convection for the same column of greenhouse gases and incoming solar radiation. Initially, we performed a test run assessing only the radiative equilibrium condition for a climate system with no convective adjustment and a relative humidity of 100%. This test case proves a highly sensitive climate to temperature and vapor

content because of steep exponential increase of water vapor saturation pressure with temperature versus more linear dependence of surface radiative temperature with surface water vapor partial pressure (Fig. 4.5). A consequence of this rigid condition there is only one point that is in an equilibrium state where the vapor pressure is the same as saturation pressure of the radiative surface temperature. The Earth would be in runaway state if the convection would be absent. However, when convection is present, the air mass is circulated at high altitude, and moist air as it raises it loses some of its water through precipitation and therefore the average amount of water vapor in atmosphere is reduced. This reduction reduces the radiative effect, and the theoretic radiative surface temperature is reduced compared with the no convection regime. The surface temperature thus becomes the radiative-convective equilibrium temperature. The convection process enables the climate to converge toward this equilibrium point due to its dual effect: By reducing the amount of water in atmosphere for the same surface temperature and by cooling the atmosphere for a defined amount of water vapor (convective shift).

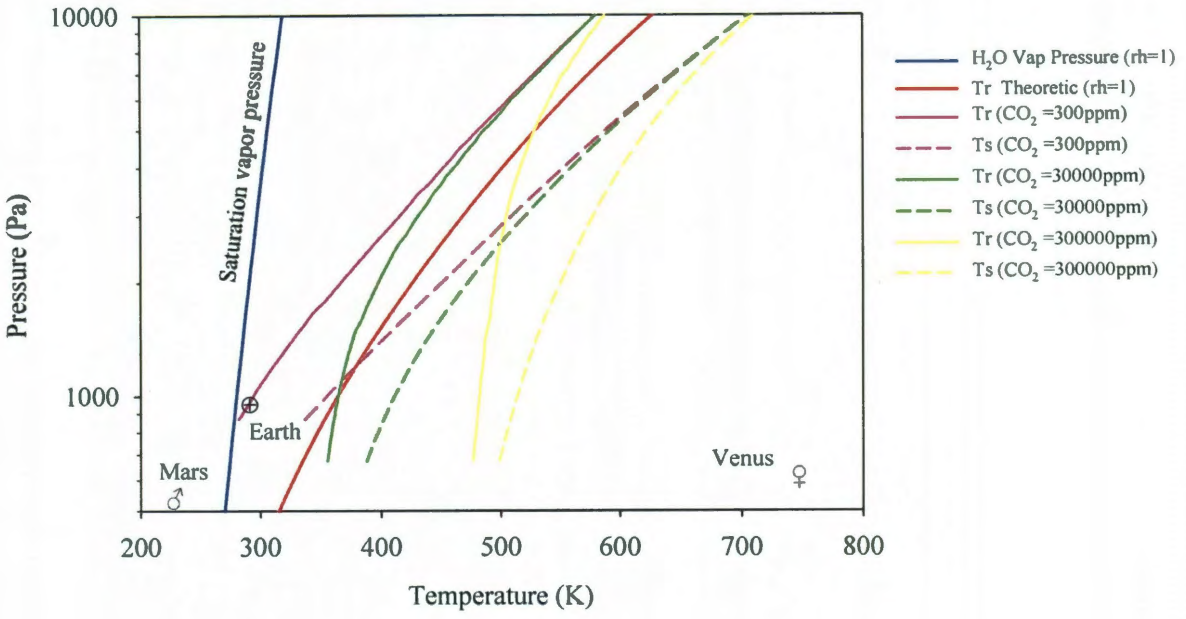

Figure 4.5. The radiative and radiative-convective surface temperature equilibrium profiles for a saturated atmosphere, and moist atmosphere. The moist atmosphere was calculated for three concentration of CO2 in order to simulate different forcing condition: 300ppm, 30000ppm and 300000ppm.

This convergence is sustained by a negative feedback effect since any weakening of convection would initiate radiative cooling on top of the atmosphere and increased temperature along with accumulation of more moisture at the surface with the consequence of making the lapse rate steeper. Both, the increased temperature difference between surface and top of the atmosphere and a steeper lapse rate are enhancing factors for the convection process that ultimately restores the convection intensity. The reverse processes occur if convection amplifies locally. The radiative-convective equilibrium curves presented in Fig. 4.5 tend to converge as the temperature increase. Regression analysis on the presented radiative-convective equilibrium states for different amount of CO_2 found that solutions converge toward a line described by the following equation:

$$P_{H2O} = 130 \cdot e^{0.0075 \cdot T}$$

The convergence illustrates the overwhelming radiative effect of water vapor for higher temperature that makes the CO_2 influence irrelevant. For comparison, the position of Mars and Venus in terms of their surface temperature and partial pressure of water vapor are displayed along with that of the Earth. Both Venus and Mars atmosphere contain less water than Earth but while Venus high surface temperature is sustained by huge amount of CO_2, Mars climate is in glacial state.

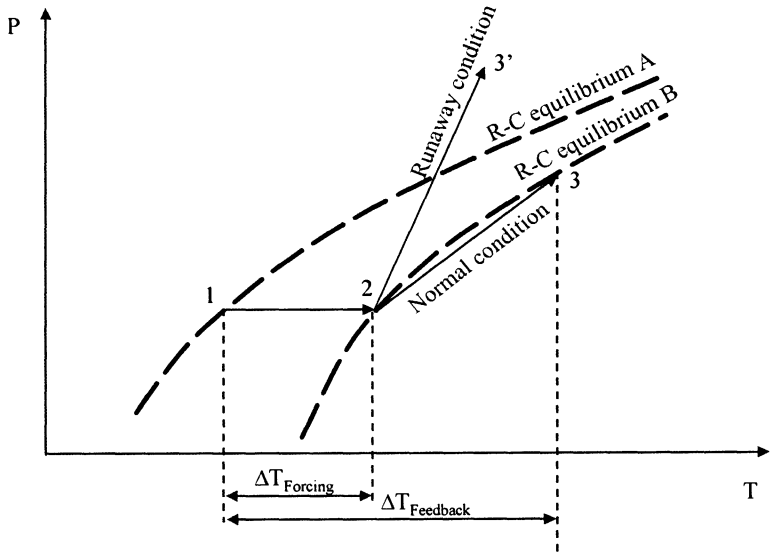

Figure 4.6. Feedback reaction for water vapor for a transformation between two equilibrium states. The variation of the water vapor amount with temperature needs to be smaller than the equilibrium line variation in order for the system stabilize at some point. Otherwise a "runaway condition" is established.

The equilibrium line for Earth crosses the saturation curve if temperature is dropped by ~15 K. Beyond that point the climate is predicted to be in a collapsed state, most of the

water is removed from the atmosphere to form ice and the temperature drop significantly to near its effective radiating value with the only greenhouse effect resulted from CO_2. This is a possible path to Mars condition although the Earth higher incoming solar radiation would prevent the surface temperature to drop below 254 K . Assuming a forced displacement from an equilibrium curve because of a forcing element effect from point 1 on the equilibrium curve A to point 2 on the equilibrium curve B (Fig. 4.6), the system responds by adding the water vapor feedback effect and move the equilibrium further at point 3. From the above definition of the feedback effect, we have for example the feedback due to the amount of CO_2 increase:

$$\frac{\Delta T_{feed}}{\Delta P_{CO_2}} = \frac{\Delta T_{force}}{\Delta P_{CO_2}} \frac{1}{1 - f_{H_2O}}$$

for small variation and ignoring the shortwave absorption of water vapor it has been demonstrated (Held and Soden 2000) that the water vapor elementary feedback is described by:

$$f_{H_2O} = -\frac{\partial \Phi}{\partial P_{H_2O}} \cdot \frac{\partial P_{H_2O}}{\partial T} \Big/ \frac{\partial \Phi}{\partial T}$$

where for simplification Φ is represented by the net flux, and P_{H2O} and T are represented by their surface values. Since the equilibrium curves are in fact numerical solution of the differential equation of the net flux equality:

$$\Phi(P_{H_2O}(T)) = \Phi(T(P_{H_2O})),$$

the flux variation function can be retrieved from the equilibrium calculation. By rearranging the terms and eliminating the flux variable, the relation becomes:

$$f_{H_2O} = -\frac{\partial P_{H_2O}}{\partial T} \Big/ \left(\frac{\partial P_{H_2O}}{\partial \Phi}\bigg|_{EQ} \cdot \frac{\partial \Phi}{\partial T}\bigg|_{EQ} \right) = -\frac{\dfrac{\partial P_{H_2O}}{\partial T}}{\dfrac{\partial P_{H_2O}}{\partial T}\bigg|_{EQ}}$$

the stability condition being:

$$\begin{cases} f_{H_2O} < 0 \rightarrow \text{normal condition} \\ f_{H_2O} \geq 0 \rightarrow \text{runnaway condition} \end{cases}$$

Visually, this implies that the variation of vapor pressure with temperature in the convective system (transformation from 2 to 3 in Fig. 4.6) to be less than the slope of the radiative-convective equilibrium curve calculated by the model, in order for the normal condition to be in effect. When this condition is satisfied, the vapor pressure eventually intercepts the equilibrium line and the system stabilizes at that point (point 3); otherwise, the pressures "run away" from the equilibrium line, and will never intercept it again. Since we have shown early that in a non-convective system the equilibrium is difficult to attain at high temperatures a consequence of this observations is that for atmospheres at relatively high temperature the convection process in the atmosphere is the principal element that stabilizes the climate.

Assuming a known value for the water vapor feedback, the response of the climate system to the forcing element variation can then be calculated. In practice, this is not easy to attain due to the complexity and heterogeneity of the water vapor accumulation and circulation in atmosphere. While most authors agree that the partial pressure of water increase with the surface temperature (positive feedback), an exact quantitative relation that describe this dependence has not been developed yet. The partial pressure of water vapor is however related

to the maximum (saturated) value and this is in exponential grow relation with temperature. As we have shown early, the real vapor pressure is reduced by the convection as some of the water precipitates in the process and the atmosphere is assumed being well mixed. The total water in the atmosphere is related then to the evaporation rate and an approximate relation (aerodynamic method (Harbeck Jr. 1962)) has been successfully used to calculate regional-scale evaporation and the influence of wind on the evaporation rate (Neelin *et al.* 1987):

$$Q_{H2O} = \rho_w C_M u(P_{H2Osat}(T_s) - P_{H2Odry})$$

where Q_{H2O} is the evaporation flux, ρ_w is the density of liquid water, C_M is the mass diffusion coefficient of water, u is the convecting air velocity, P_{H2Osat} is the saturated water vapor pressure, and P_{H2Odry} is the water vapor partial pressure of the incoming airflow after it was depleted by circulating through troposphere. This amount of water resulted from evaporation is then mixed with the descending dry air in a boundary layer near the surface that is fed by the convection regime and mixed within the troposphere. The result of this mixing determines the average surface partial pressure and relative humidity. A parameterization of this process is far more complex but a simple scaling relation can be derived from this mixing theory. Assuming the partial pressure of dry air equal to zero the partial pressure of water is then proportional with evaporation flux divided by the flux of the dry air:

$$P_{H2O} \sim K_P \frac{u(P_{H2Osat}(T_s))}{uD_{bl}} \sim K_P \frac{(P_{H2Osat}(T_s))}{Z_{tropo} Ra(T_s)^{-\frac{1}{3}}}$$

where K_P is a proportionality constant, D_{bl} is the thickness of the mixing boundary layer, Z_{tropo} is the thickness of the troposphere and Ra is the Rayleigh number that is equivalent with the intensity of convection. The Ra number more precisely depend on the difference

between surface temperature and the temperature at top of the atmosphere but normally due to steepness of the radiative profile the top temperature stay close to the T_0 as surface temperature increase. The evaporation-convection interaction plays thus a crucial role in the establishment of the relative profile of the water in atmosphere. Increasing the surface temperature due to changes in forcing condition eventually lead to increased evaporation but also increased convection intensity, which in turn increase precipitation and influx of dry air. A balance among this processes condition the evolution of surface vapor pressure with temperature but an exact quantification is yet to be developed in climatology before a more accurate evaluation of water vapor feedback can assessed.

Implications for planetary climate stability

Since climate evolution models require estimation of magnitude of the water vapor feedback effect and we are yet to develop an accurate parameterization of this process, we analyze here the possible scenarios for climate equilibrium conditions. A paradox that continues to puzzle the planetary climatologists today is the apparent contradiction between the expected surface temperatures calculated for past solar radiation (Sagan and Chyba 1997; Kasting 2005a) and the values interpreted from paleoclimatic evidences especially for Earth and Mars (Pollack 1979). According to current stellar evolution models, the Sun was less bright in the geologic past and its intensity evolved from about 70% at 4.7 GA to present day value (Gough 1981). The evidences for ancient climate are sparse but they suggest that for an extended period during Archean for example surface temperatures was in the range of 55-85°C (Kasting and Ono 2006). A similar problem poses the Martian climate for example. Several explanations have been proposed and models that attempt to interpret the past climate generally assumes an increased amount of CO_2 in the atmosphere of early Earth (Kasting

2005a) and Mars (Pollack *et al.* 1987; Yokohata *et al.* 2002). Although this can provide a good physical explanation, geochemical models that includes a carbonate cycle (Franck *et al.* 2001) have found the CO_2 theory unsatisfactory (Lasaga *et al.* 2001; Sleep and Zahnle 2001; Kasting 2005a). Other models consider amonia as a source of enhanced greenhouse (Sagan and Mullen 1972), or methane (Pavlov *et al.* 2000; Kasting 2005b). In the case of Mars a innovative model that explain the early warming as a result of infrared scattering by CO_2 ice clouds have also been proposed (Forget and Pierrehumbert 1997). In this study, we investigate the possibility of enhanced water vapor in atmosphere to contribute to the warming effect and ensure the stability of climate.

It was recognized that impact-generated heat released during the accretion of terrestrial planets could produce a steam atmosphere over a magma ocean that would be sufficient to maintain a runaway greenhouse condition at the surface of the planet (Zahnle *et al.* 1988; Segura *et al.* 2002). Although the Hadean is generally assumed a hot period, some recent evidences suggest the climate was nevertheless mild enough to accommodate surface liquid water at least since 4.4 GA (Valley *et al.* 2002). Among these hypotheses, is worth considering the conditions that would preserve a stable and warm climate in the spite of reduced solar radiation, but based instead on the increased amount of water vapor in the atmosphere. Assuming the initial heat of planetary formation constrained the amount of water vapor in atmosphere to produce along with other greenhouse gases the moderate-warm climate, we calculated using our model the amount of water in atmosphere that is required to maintain the climate in equilibrium for a given surface temperature. As solar intensity increases, the amount of water in atmosphere is reduced, possibly due to increased convective intensity that would speed up the hydrologic cycle, but the exact mechanism is yet to be investigated. We limit here

in calculating a series of equilibrium temperature profiles that satisfy the solar luminosity constraint and give a temperate climate using a different amount of water vapor as greenhouse enhancement factor. The evolution of climate is then considered a succession of equilibrium states, as any change in forcing conditions would shift the profile to a new equilibrium state.

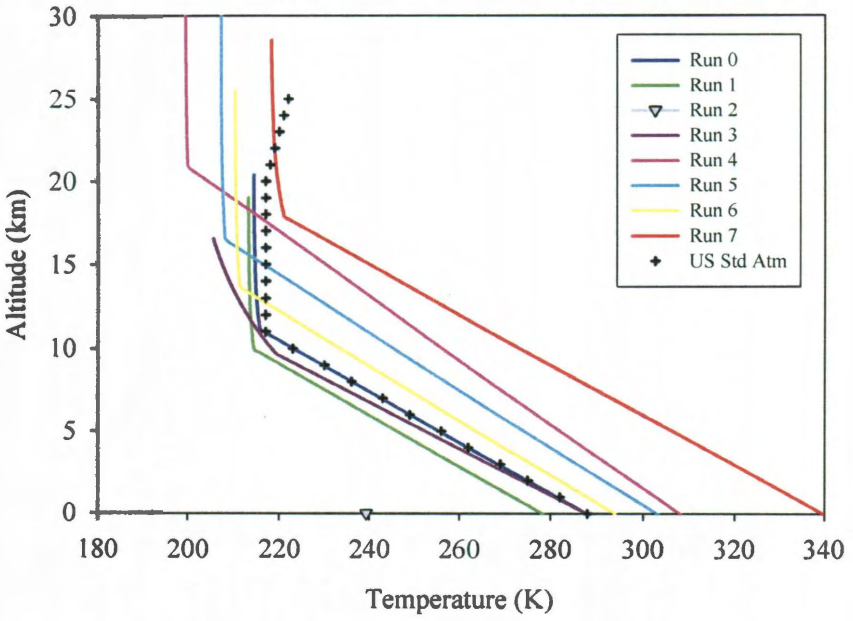

Figure 4.7. Earth variable parameter conditions runs. Run 0: Current normal Earth. Run 1: Earth condition for limited reduced solar luminosity. Run 2: Primordial Earth, solar luminosity is reduced with 25% (1024 W/m2), surface temperature 239 K; Run 3: Solar luminosity for primordial Earth and the amount of CO2 was increased to 11000ppmv and water vapor pressure was 900 Pa to obtain the current surface temperature of 288 K. Run 4: Primordial Earth luminosity CO2 was reduced to 1500 ppmv and water vapor pressure was increased to 2240 Pa. Run 5: Solar luminosity to 1200 W/m2 CO2 was reduced to 750 ppmv and water vapor pressure was established to 1560 Pa. Run 6: Solar luminosity to 1266 W/m2 CO2 was reduced to 470 ppmv and water vapor pressure was established to 1236 Pa. run 7: Profile for increased solar luminosity (1466 W/m2). Illustrates the role of water vapor in balancing other forcing elements.

The runs start with a reference case for both Earth and Mars that tests the current condition on both planets (Run 0 on Fig. 4.7 and Fig. 4.8 respectively). The plots contain also average temperature profiles from standard models or measurements. For Earth the U.S. Standard Atmosphere 1976 is displayed and for Mars the profiles from three missions are plotted. Our model calculates about 13.7 kg of precipitable water in an atmospheric column with area equal to unity for an average relative humidity of 56%. The calculations are performed only up to the tropopause, assuming that above that level water is present only in very small quantity. The solution to equilibrium condition would be a P-T curve as we showed earlier, unless constrained by a set value of relative humidity to a single point. Since a full solution that can solve the relative humidity would involve the feedback parameterization and a full hydrologic cycle, solutions difficult to implement in a 1D model, we considered fixed relative humidity values to derive the climate profile. The only assumption we made when selecting the relative humidity value is that its variation relatively to reference model is inverse proportional to the convection intensity and therefore with temperature variation. If solar luminosity is reduced by ~2% to 1336 W/m^2 (Run 1) the surface temperature drop to 278 K and the amount of atmospheric water would be reduced to 11.9 kg/m^2, assuming the rest of the greenhouse gases remain the same. This would correspond to wide-scale glacial conditions. In the next run (Run 2), we assumed primordial Earth condition, solar luminosity is reduced with 25% (1024 W/m^2) and the surface temperature became 239 K. Water is virtually absent from atmosphere, adiabatic lapse rate exceed the radiative rate freezing the convection and Earth becomes a snowball, warmed only by the CO_2 assumed at present day value. This is the paradox situation. Further, keeping the solar luminosity for primordial Earth, we increased the amount of CO_2 to 11000 ppmv (Run 3) in order to simulate a present day surface temperature of 288 K in the condition of reduced solar luminosity and about the same amount of water in

atmosphere (12.2 kg/m^2 using the same relative humidity as in reference model). In run 4 assuming the luminosity of primordial Earth, CO_2 was set to 1500 ppmv and water vapor partial pressure was increased to 2240 Pa. The amount of water in this case was 38 kg/m^2 and 40% relative humidity. Surface temperature stabilizes at 308 K, the climate is warm enough to allow for liquid water at surface, and yet cold enough to prevent run away condition. In run 5 and run 6 solar luminosity was increased from 1200 W/m^2 to 1266 W/m^2 and CO_2 was successively reduced from 750 ppmv to 470 ppmv to simulate two intermediate steps in solar and planetary evolution. The climate attained two corresponding stable conditions with surface temperatures of 303 K and 294 K respectively. The necessary water was 25.8 kg/m^2 and 19 kg/m^2 for a relative humidity at about 40%. In the last run we tested a Gaia like scenario with solar luminosity increased to 1466 W/m^2. The question here was to determine at what level we should reduce the water in atmosphere to keep the climate in a stable condition. Increased solar radiation will push the temperatures up and this will raise dramatically the amount of water evaporated to 27 kg/m^2. The relative humidity needs to be reduced to as low as 5% in order to stabilize the climate system around 340 K.

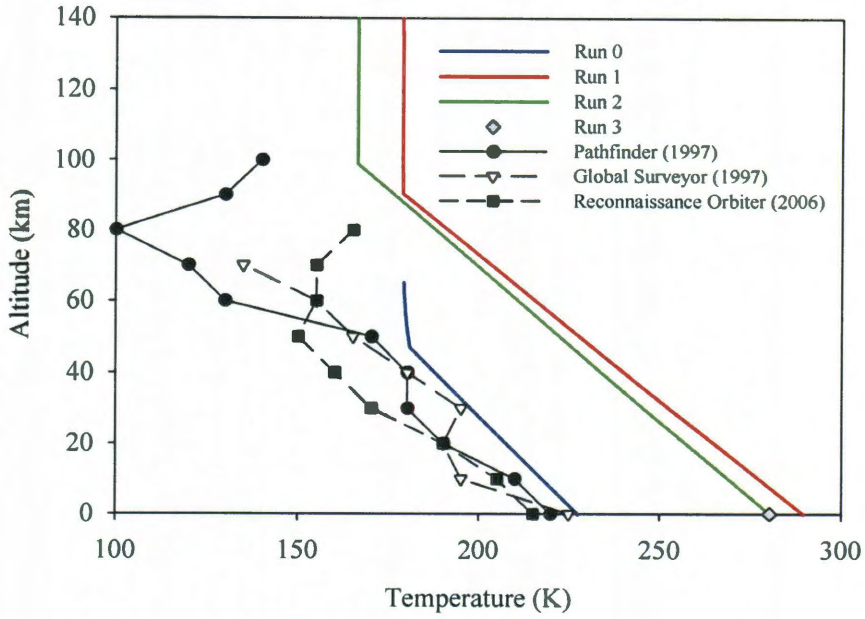

Figure 4.8. Mars variable parameter conditions runs. Run 0. Current mars profile. Run 1: Mars with 470 Pa water vapor would have Earth temperature. Run 2: Mars with reduced solar luminosity could still attain surface temperatures suitable for the presence of liquid water if vapor pressure could be established at ~800 Pa. Run 3: Same solar luminosity (less 25% of today – 442 W/m2) but the liquid water condition are obtained by increasing the amount of CO2 4 times today value with no water vapor increase.

In the case of Mars the situation is complicated by the fact that little water is present in atmosphere, at present the planet is in a run away glaciation state. In addition, average surface temperatures in the order of 220 K are near the CO_2 phase boundary for its partial pressure. Phenomenon like CO_2 snow and CO_2 ice clouds common on the planet greatly affect the radiative balance. A warm early Mars that accommodates surface liquid water would require increased amount of greenhouse gases to heat up the atmosphere. It has been demonstrated that only a dual CO_2-H_2O atmosphere would have been unable to warm up the climate from its glacial state in the early history of planet in condition of reduced solar luminosity (Squyres and Kasting 1994). The quest for answer of possible heat sources being underway we used the

same approach like in the case of Earth to estimate the amount of water vapor in the atmosphere that would ensure climate stability assuming a source of heat was available to raise that water in air. Among possible such sources, impact generated heat would be the principal suspect, and some suggest that up to 16 m equivalent precipitable water could be injected into atmosphere by largest impactors (Segura *et al.* 2002). Most of this quantity is subsequently precipitated but some would probably remain in atmosphere longer, and in this case could provide the necessary buffer for climate stability. In addition to primordial climate paradox, new evidences suggest the presence of liquid water near surface in more recent times and hence the possibility of warmer climate not far away in time. Our simulations found that about 30 kg/m^2 would ensure Earth like condition at Mars surface with an atmosphere having the present level of CO_2 and about 25% relative humidity (Run 1). This is a very large quantity representing roughly 100 times the present level of water vapor, and this was obtained without considering the increase of albedo because of changes in cloudiness. In run 2 and 3 we considered the primordial Mars solar condition (less 25% of today – 442 W/m^2) and we calculated two extreme solutions to obtain surface temperatures suitable for the presence of liquid water. If water is considered the only extra source of greenhouse warming (Run 2) then its vapor pressure should reach about 800 Pa or the equivalent of 43 kg/m^2 precipitable water. In run 3 we have the same solar luminosity but the liquid water condition are obtained by increasing the amount of CO_2 only. About 4 times of today's value of CO_2 is required and in both cases a surface temperature of 280 K was attained.

Conclusions

We focused our attention in addressing the role of water vapor in planetary climate stability and on some aspects of the feedback relationship among water temperature and other greenhouse components. We developed a one dimensional grey radiative-convective climate model and investigated various scenarios through numeric simulations. The model is based on simple physics principles but the aim was to be easy applicable to various planetary environments. The nature of water element to be near its phase transition in the normal Earth environment, poses many challenges for its feedback parameterization. A similar problem we have for the CO_2 in the Martian atmosphere. Numeric simulations showed that changing the average atmospheric temperature alone induces its own feedback effect that adds to the overall effect. Implementation of a full hydrologic cycle is desirable in order to implement a reliable feedback parameterization. In term of climate stability water vapor could represent an important function in planetary warming in condition of a reduced incoming solar luminosity, a similar effect to that experienced by planets in our solar system in the geologic past. Its role is often overlooked due to the concept that it is difficult to accumulate in the atmosphere in the absence of other forcing elements. However, if early during planetary evolution primordial heat was able to evaporate significant quantity of water our simulation indicate that a wet atmosphere associated with other greenhouse components could ensure a relatively stable climatic condition that challenges the early faint sun paradox.

CONCLUDING REMARKS AND FUTURE RESEARCH PERSPECTIVES

We conclude that volatiles plays an important role in regulating many parameters involved in thermal evolution of planets. We used simple one dimension parameterized models to run different scenarios that proved robust enough to address some of the fundamental aspects of volatile cycle through planetary systems. In order to understand also some topological relationship among factors involved in this cycle or the geometric variation of attributes full 2D and 3D models are highly desirable. The presence of the melt zone below the lithosphere turns out to have a critical influence on the degassing rates and it could play an important role in the transition mechanism that can switch the tectonic style through controls on the buoyancy of the lithospheric lid. Further research can involve a more complex petrological model in order to quantify the partial melt zone and address the problem of water trapping mechanism and multiple layer convection based on mineralogical phase boundaries. Both mantle and climate systems strongly need to involve a CO_2 cycle that added to the water could provide better understanding of the volatile cycle, and may uncover further implications.

REFERENCES

Aldener, M., S. S. Brown, et al. (2005). "Near-IR absorption of water vapor: Pressure dependence of line strengths and an upper limit for continuum absorption." Journal of Molecular Spectroscopy **232**(2): 223-230.

Ballard, S. and H. N. Pollack (1988). "Modern and ancient geotherms beneath southern Africa." Earth and Planetary Science Letters **88**(1-2): 132-142.

Barton, I. J. (1991). "Infrared continuum water vapor absorption coefficients derived from satellite data." Appl. Opt. **30**(21): 2929-2934.

Bell, K. and J. Blenkinsop (1987). "Nd and Sr isotopic compositions of East African carbonatites: Implications for mantle heterogeneity." Geology **15**(2): 99-102.

Bercovici, D. and S.-i. Karato (2003). "Whole-mantle convection and the transition-zone water filter." Nature **425**(6953): 39-44.

Bignell, K. J. (1970). "The water-vapour infra-red continuum." Quarterly Journal of the Royal Meteorological Society **96**(409): 390-403.

Bolfan-Casanova, N. (2007). "Fuel for Plate Tectonics." Science **315**(5810): 338-339.

Bounama, C., S. Franck, et al. (2001). "The fate of Earth's ocean." Hydrol. Earth Syst. Sci. **5**(4): 569-576.

Boyd, F. R., J. J. Gurney, et al. (1985). "Evidence for a 150-200-km thick Archaean lithosphere from diamond inclusion thermobarometry." Nature **315**(6018): 387-389.

Carter, N. L. and H. G. Ave'Lallemant (1970). "High Temperature Flow of Dunite and Peridotite." Geological Society of America Bulletin **81**(8): 2181–2202.

Chopra, P. N. and M. S. Paterson (1984). "The role of water in the deformation of dunite." J. Geophys. Res. **89**(B9): 7861–7876.

Chou, M.-D. (1992). "A Solar Radiation Model for Use in Climate Studies." Journal of the Atmospheric Sciences **49**(9): 762-772.

Christensen, U. R. (1984). "Heat transport by variable viscosity convection and implications for the Earth's thermal evolution." Physics of The Earth and Planetary Interiors **35**(4): 264-282.

Conrad, C. P. and B. H. Hager (1999). "The thermal evolution of an Earth with strong subduction zones." Geophys. Res. Lett. **26**(19): 3041-3044.

Curry, J. A. and P. J. Webster (1999). Thermodynamics of Water. Thermodynamics of Atmospheres and Oceans, Academic Press: 96-127.

Davaille, A. and C. Jaupart (1993). "Transient high-Rayleigh-number thermal convection with large viscosity variations." J. Fluid Mech. **253**: 141-166.

Davies, G. F. (1979). "Thickness and thermal history of continental crust and root zones." Earth and Planetary Science Letters **44**(2): 231-238.

Davies, G. F. (1980). "Thermal Histories of Convective Earth Models and Constraints on Radiogenic Heat Production in the Earth." J. Geophys. Res. **85(B5)**: 2517-2530.

Doherty, G. M. and R. E. Newell (1984). "Radiative effects of changing atmospheric water vapour." Tellus Series B **36**: 149-162.

Doin, M.-P., L. Fleitout, et al. (1997). "Mantle convection and stability of depleted and undepleted continental lithosphere." J. Geophys. Res. **102**(B2): 2771-2787.

Forget, F. and R. T. Pierrehumbert (1997). "Warming Early Mars with Carbon Dioxide Clouds That Scatter Infrared Radiation." Science **278**(5341): 1273-1276.

Fowler, A. C. (1993). "Boundary Layer Theory and Subduction." J. Geophys. Res. **98**(B12): 21997-22005.

Franck, S. and C. Bounama (1995a). "Effects of water-dependent creep rate on the volatile exchange between mantle and surface reservoirs." Physics of the Earth and Planetary Interiors **92**(1): 57-65.

Franck, S. and C. Bounama (1995b). "Rheology and volatile exchange in the framework of planetary evolution." Advances in Space Research **15**(10): (10)79-(10)86.

Franck, S. and C. Bounama (2001). "Global water cycle and Earth's thermal evolution." Journal of Geodynamics **32**(1): 231-246.

Franck, S., W. von Bloh, et al. (2001). "Limits of photosynthesis in extrasolar planetary systems for earth-like planets." Advances in Space Research **28**(4): 695-700.

Gao, S., R. L. Rudnick, et al. (2002). "Re-Os evidence for replacement of ancient mantle lithosphere beneath the North China craton." Earth and Planetary Science Letters **198**(3-4): 307-322.

Goody, R. M. and Y. L. Yung (1989). Atmospheres in radiative equilibrium. Atmospheric Radiation: Theoretical Basis, Oxford University Press: 388-421.

Gough, D. O. (1981). "Solar interior structure and luminosity variations." Solar Physics **74**(1): 21-34.

Grand, S. P. (1987). "Tomographic Inversion for Shear Velocity Beneath the North American Plate." J. Geophys. Res. **92**(B13): 14065-14090.

Grasset, O. and E. M. Parmentier (1998). "Thermal convection in a volumetrically heated, infinite Prandtl number fluid with strongly temperature-dependent viscosity: Implications for planetary thermal evolution." J. Geophys. Res. **103**(B8): 18171-18181.

Grigné, C., S. Labrosse, et al. (2007). "Convection under a lid of finite conductivity: Heat flux scaling and application to continents." J. Geophys. Res. **112**(B8): B08402.

Gutzler, D. S. (1993). "Uncertainties in Climatological Tropical Humidity Profiles: Some Implications for Estimating the Greenhouse Effect." Journal of Climate **6**(5): 978-982.

Hallam, A. (1992). Phanerozoic Sea-Level Changes, Columbia University Press.

Hansen, J., D. Johnson, et al. (1981). "Climate Impact of Increasing Atmospheric Carbon Dioxide." Science **213**(4511): 957-966.

Harbeck Jr., G. E. (1962). A practical field technique for measuring reservoir evaporation utilizing mass-transfer theory. Prof. Paper, US Geol. Surv.: 101–105.

Held, I. M. and B. J. Soden (2000). "Water vapor feedback and global warming." Annual Review of Energy and the Environment **25**(1): 441-475.

Hirschmann, M. M. (2000). "Mantle solidus: Experimental constraints and the effects of peridotite composition." Geochemistry Geophysics Geosystems **1**(10): 1-26.

Hirschmann, M. M. (2006). "Water, Melting, and the Deep Earth H_2O Cycle." Ann. Rev. Earth Planet. Sci. **34**: 629-653.

Hirth, G. and D. L. Kohlstedt (1996). "Water in the oceanic upper mantle: implications for rheology, melt extraction and the evolution of the lithosphere." Earth and Planetary Science Letters **144**(1-2): 93-108.

Houghton, J. (2005). "Global warming." Rep. Prog. Phys. **6**: 1343-1403.

James, D. E., M. J. Fouch, et al. (2001). "Tectospheric structure beneath southern Africa." Geophys. Res. Lett. **28**(13): 2485-2488.

Jarrard, R. D. (2003). "Subduction fluxes of water, carbon dioxide, chlorine, and potassium." Geochemistry Geophysics Geosystems **4**(5): 8905.

Jaupart, C., S. Labrosse, et al. (2007). Temperatures, Heat and Energy in the Mantle of the Earth. Treatise on Geophysics. S. Bercovici, Elsevier **vol. 7: Mantle dynamics:** 253-303.

Jordan, T. H. (1978). "Composition and development of the continental tectosphere." Nature **274**(5671): 544-548.

Karato, S.-I. (1989). Defects and plastic deformation in olivine. Rheology of Solids and of the Earth. S.-I. Karato and M. Toriumi. Oxford, Oxford University Press: 176-208.

Karato, S.-I., M. S. Paterson, et al. (1986). "Rheology of Synthetic Olivine Aggregates: Influence of Grain Size and Water." J. Geophys. Res. **91**(B8): 8151–8176.

Karato, S.-I. and P. Wu (1993). "Rheology of the Upper Mantle - a Synthesis." Science **260**(5109): 771-778.

Kasting, J. F. (2005a). "Methane and climate during the Precambrian era." Precambrian Research **137**(3-4): 119-129.

Kasting , J. F. (2005b). "Methane and climate during the Precambrian era " Precambrian Research **137**: 119-129.

Kasting , J. F. and S. Ono (2006). "Palaeoclimates: the first two billion years." Phil. Trans. R. Soc. B **361**: 917-929.

Katz, R. F., M. Spiegelman, et al. (2003). "A new parameterization of hydrous mantle melting." Geochemistry Geophysics Geosystems **4**(9): 1-19.

Kawamoto, T. and J. R. Holloway (1997). "Melting temperature and partial melt chemistry of H2O-saturated mantle peridotite to 11 gigapascals." Science **276**(5310): 240-243.

Kerr, R. M. (1996). "Rayleigh number scaling in numerical convection." Journal of Fluid Mechanics Digital Archive **310**: 139-179.

Kohlstedt, D. L. (2006). "The Role of Water in High-Temperature Rock Deformation." Reviews in Mineralogy and Geochemistry **62**(1): 377-396.

Kohlstedt, D. L., B. Evans, et al. (1995). "Strength of the lithosphere: Constraints imposed by laboratory experiments." J. Geophys. Res. **100**(B9): 17587-17602.

Korenaga, J. (2008). "Urey ratio and the structure and evolution of Earth's mantle." Reviews of Geophysics **46**: 1-32.

Kuhn, T., A. Bauer, et al. (2002). "Water vapor continuum: absorption measurements at 350 GHz and model calculations." Journal of Quantitative Spectroscopy and Radiative Transfer **74**(5): 545-562.

Lacis, A. A. and J. Hansen (1974). "A Parameterization for the Absorption of Solar Radiation in the Earth's Atmosphere." Journal of the Atmospheric Sciences **31**(1): 118-133.

Lasaga, A. C., D. M. Rye, et al. (2001). "Calculation of fluid fluxes in Earth's crust." Geochimica et Cosmochimica Acta **65**(7): 1161-1185.

Lenardic, A. (1998). "On the partitioning of mantle heat loss below oceans and continents over time and its relationship to the Archaean paradox." Geophysical Journal International **134**(3): 706-720.

Lenardic, A., A. M. Jellinek, et al. (2008). "A climate induced transition in the tectonic style of a terrestrial planet." Earth and Planetary Science Letters **271**(1-4): 34-42.

Lenardic, A. and W. M. Kaula (1996). "Near-surface thermal/chemical boundary layer convection at infinite Prandtl number - Two-dimensional numerical experiments." Geophysical Journal International **126**(3): 689-711.

Lenardic, A. and L. Moresi (2003). "Thermal convection below a conducting lid of variable extent: Heat flow scalings and two-dimensional, infinite Prandtl number numerical simulations." Physics of Fluids **15**(2): 455-466.

Lenardic, A., L. Moresi, et al. (2000). "The role of mobile belts for the longevity of deep cratonic lithosphere: The Crumple Zone Model." Geophys. Res. Lett. **27**(8): 1235-1238.

Lenardic, A. and L. N. Moresi (1999). "Some thoughts on the stability of cratonic lithosphere: Effects of buoyancy and viscosity." J. Geophys. Res. **104**(B6): 12747-12758.

Lenardic, A., L. N. Moresi, et al. (2005). "Continental insulation, mantle cooling, and the surface area of oceans and continents." Earth and Planetary Science Letters **234**(3-4): 317-333.

Lenardic, A., L. N. Moresi, et al. (2003). "Longevity and stability of cratonic lithosphere: Insights from numerical simulations of coupled mantle convection and continental tectonics." J. Geophys. Res. **108**(B6): 2303.

Lenardic, A., M. A. Richards, et al. (2006). "Depth-dependent rheology and the horizontal length scale of mantle convection." J. Geophys. Res. **111**(B07404): 1-13.

Li, Z.-X. A., C.-T. A. Lee, et al. (2008). "Water contents in mantle xenoliths from the Colorado Plateau and vicinity: Implications for the mantle rheology and hydration-induced thinning of continental lithosphere." J. Geophys. Res. **113**.

Ligi, M., E. Bonatti, et al. (2005). "Water-rich basalts at mid-ocean-ridge cold spots." Nature **434**: 66-69.

Lindzen, R. S. (1994). "Climate Dynamics and Global Change." Annual Review of Fluid Mechanics **26**(1): 353-378.

Lindzen, R. S., A. Y. Hou, et al. (1982). "The Role of Convective Model Choice in Calculating the Climate Impact of Doubling CO2." Journal of the Atmospheric Sciences **39**(6): 1189-1205.

Litasov, K. D. and E. Ohtani (2007). Effect of water on the phase relations in Earth's mantle and deep water cycle. Advances in High-Pressure Mineralogy. E. Ohtani, GSA. **421:** 115-156.

Lorenz, R. D. and C. P. McKay (2003). "A simple expression for vertical convective fluxes in planetary atmospheres." Icarus **165**(2): 407-413.

Mackwell, S. J., D. L. Kohlstedt, et al. (1985). "The Role of Water in the Deformation of Olivine Single Crystals." J. Geophys. Res. **90**(B13): 11,319–11,333.

Manabe, S. and R. F. Strickler (1964). "Thermal equilibrium of the atmosphere with a convective adjustment." J. Atmos. Sci. **21**: 361-385.

Manabe, S. and R. T. Wetherald (1967). "Thermal Equilibrium of the Atmosphere with a Given Distribution of Relative Humidity." Journal of the Atmospheric Sciences **24**(3): 241-259.

Manga, M. and R. J. O'Connell (1995). "The tectosphere and postglacial rebound." Geophys. Res. Lett. **22**(15): 1949-1952.

Manga, M., D. Weeraratne, et al. (2001). "Boundary-layer thickness and instabilities in Bénard convection of a liquid with a temperature-dependent viscosity." Physics of Fluids **13**(3): 802-805.

Maruyama, S. (1999). "Leaking water into the Earth " EOS! Transactions, American Geophysical Union **80**(Fall Meeting Abstract): U31B-06.

Maruyama, S. and J. Liou (2005). "From Snowball to Phaneorozic Earth." International Geology Review **47**(8): 775-791.

McGovern, P. J. and G. Schubert (1989). "Thermal evolution of the Earth: effects of volatile exchange between atmosphere and interior." Earth and Planetary Science Letters **96**(1): 27-37.

McKenzie, D. (1984). "The generation and compaction of partially molten rock." J. Petrol. **25**: 713--765.

McKenzie, D. and M. Bickle (1988). "The volume and composition of melt generated by extension of the litosphere." Journal of Petrology **29**: 625-679.

McKenzie, D., J. Jackson, et al. (2005). "Thermal structure of oceanic and continental lithosphere." Earth and Planetary Science Letters **233**(3-4): 337-349.

Mei, S. and D. L. Kohlstedt (2000). "Influence of water on plastic deformation of olivine aggregates 2. Dislocation creep regime." J. Geophys. Res. **105**(B9): 21,471–21,481.

Menzies, M. A., W. Fan, et al. (1993). "Palaeozoic and Cenozoic lithoprobes and the loss of >120 km of Archaean lithosphere, Sino-Korean craton, China." Geological Society, London, Special Publications **76**(1): 71-81.

Michaut, C. and C. Jaupart (2007). "Secular cooling and thermal structure of continental lithosphere." Earth and Planetary Science Letters **257**(1-2): 83-96.

Michaut, C., C. Jaupart, et al. (2009). "Thermal evolution of cratonic roots." Lithos **109**(1-2): 47-60.

Mitrovica, J. X. and A. M. Forte (2004). "A new inference of mantle viscosity based upon joint inversion of convection and glacial isostatic adjustment data." Earth and Planetary Science Letters **225**(1-2): 177-189.

Moresi, L., F. Dufour, et al. (2003). "A Lagrangian integration point finite element method for large deformation modeling of viscoelastic geomaterials." Journal of Computational Physics **184**(2): 476-497.

Moresi, L. and V. S. Solomatov (1998). "Mantle convection with a brittle lithosphere: thoughts on the global tectonic styles of the Earth and Venus." Geophysical Journal International **133**(3): 669-682.

Moresi, L. N. and V. S. Solomatov (1995). "Numerical investigation of 2D convection with extremely large viscosity variations." Physics of Fluids **7**(9): 2154-2162.

Neelin, J. D., I. M. Held, et al. (1987). "Evaporation-Wind Feedback and Low-Frequency Variability in the Tropical Atmosphere." Journal of the Atmospheric Sciences **44**(16): 2341-2348.

O'Neill, C., A. M. Jellinek, et al. (2007a). "Conditions for the onset of plate tectonics on terrestrial planets and moons." Earth and Planetary Science Letters **261**(1-2): 20-32.

O'Neill, C., A. Lenardic, et al. (2007b). "Melt propagation and volcanism in mantle convection simulations." J. Geophys. Res. **112**.

O'Neill, C., A. Lenardic, et al. (2007c). "Episodic Precambrian subduction." Earth and Planetary Science Letters **262**(3-4): 552-562.

O'Neill, C. J., A. Lenardic, et al. (2008). "Dynamics of cratons in an evolving mantle." Lithos **102**(1-2): 12-24.

Ohtani, E., K. Litasov, et al. (2004). "Water transport into the deep mantle and formation of a hydrous transition zone." Physics of The Earth and Planetary Interiors **143-144**: 255-269.

Olson, P. and G. M. Corcos (1980). "A boundary layer model for mantle convection with surface plates." Geophysical Journal of the Royal Astronomical Society **62**(1): 195-219.

Pavlov, A. A., J. F. Kasting, et al. (2000). "Greenhouse warming by CH_4 in the atmosphere of early Earth." J. Geophys. Res. **105**: 11,981–11,990.

Peacock, S. M. (1990). "Fluid Processes in Subduction Zones." Science **248**(4953): 329-337.

Phillips, R. J., M. A. Bullock, et al. (2001). "Climate and interior coupled evolution of Venus." Geophysical Research Letters **28**(9): 1779-1782.

Pollack, H. N. (1986). "Cratonization and thermal evolution of the mantle." Earth and Planetary Science Letters **80**(1-2): 175-182.

Pollack, J. B. (1969a). "A nongray CO_2-H_2O greenhouse model of Venus." Icarus **10**(2): 314-341.

Pollack, J. B. (1969b). "Temperature structure of nongray planetary atmospheres." Icarus **10**(2): 301-313.

Pollack, J. B. (1979). "Climatic change on the terrestrial planets." Icarus **37**(3): 479-553.

Pollack, J. B., J. F. Kasting, et al. (1987). "The case for a wet, warm climate on early Mars." Icarus **71**(2): 203-224.

Ramanathan, V. (1981). "The Role of Ocean-Atmosphere Interactions in the CO2 Climate Problem." Journal of the Atmospheric Sciences **38**(5): 918-930.

Ramanathan, V. and J. A. Coakley Jr. (1978). "Climate Modeling Through Radiative-Convective Models." Rev. Geophys. **16**(4): 465–489.

Randall, D. A., Q. Hu, et al. (1994). "Radiative-convective disequilibrium." Atmos. Res. **31**: 315-327.

Raval, A. and V. Ramanathan (1989). "Observational determination of the greenhouse effect." Nature **342**(6251): 758-761.

Reese, C. C., V. S. Solomatov, et al. (1998). "Heat transport efficiency for stagnant lid convection with dislocation viscosity: Application to Mars and Venus." J. Geophys. Res. **103**(E6): 13643-13657.

Rennó, N. O., K. A. Emanuel, et al. (1994). "Radiative-convective model with an explicit hydrologic cycle 1. Formulation and sensitivity to model parameters." J. Geophys. Res. **99(D7)**: 14,429–14,441.

Ritzwoller, M. H., N. M. Shapiro, et al. (2004). "Cooling history of the Pacific lithosphere." Earth and Planetary Science Letters **226**(1-2): 69-84.

Roberts, R. E., J. E. A. Selby, et al. (1976). "Infrared continuum absorption by atmospheric water vapor in the 8-12-micrometer window." Applied Optics **15**(9): 2085-2090.

Rogers, J. J. W. and M. Santosh (2006). "The Sino-Korean Craton and supercontinent history: Problems and perspectives." Gondwana Research **9**(1-2): 21-23.

Rothman, L. S., I. E. Gordon, et al. (2009). "The HITRAN 2008 molecular spectroscopic database." Journal of Quantitative Spectroscopy and Radiative Transfer **110**(9-10): 533-572.

Rupke, L. H., J. P. Morgan, et al. (2004). "Serpentine and the subduction zone water cycle." Earth and Planetary Science Letters **223**(1-2): 17-34.

Sagan, C. (1969). "Gray and nongray planetary atmospheres structure, convective instability, and greenhouse effect." Icarus **10**(2): 290-300.

Sagan, C. and C. Chyba (1997). "The Early Faint Sun Paradox: Organic Shielding of Ultraviolet-Labile Greenhouse Gases." Science **276**(5316): 1217-1221.

Sagan, C. and G. Mullen (1972). "Earth and Mars: Evolution of Atmospheres and Surface Temperatures." Science **177**(4043): 52-56.

Sandu, C. and A. Lenardic (2008). "The effects of volatile cycling on planetary thermal evolution (Abstract)." EOS Trans. AGU, fall meeting supl. **89**.

Schmidt, M. W. and S. Poli (1998). "Experimentally based water budgets for dehydrating slabs and consequences for arc magma generation." Earth and Planetary Science Letters **163**(1-4): 361-379.

Schubert, G. (1978). "Subsolidus convection in the mantles of terrestrial planets." Annual Review of Earth and Planetary Sciences **7**: 289-342

Schubert, G., P. Cassen, et al. (1979). "Subsolidus convective cooling histories of terrestrial planets." Icarus **38**(2): 192-211.

Schubert, G., D. Stevenson, et al. (1980). "Whole planet cooling and the radiogenic heat source contents of the Earth and Moon." J. Geophys. Res. **85**(B5): 2531–2538.

Schubert, G., D. L. Turcotte, et al. (2001). Boundary Layer Theory. Mantle Convection in the Earth and Planets, Cambridge University Press: 350-361.

Segura, T. L., O. B. Toon, et al. (2002). "Environmental Effects of Large Impacts on Mars." Science **298**(5600): 1977-1980.

Sellers, W. D. (1973). "A New Global Climatic Model." Journal of Applied Meteorology **12**(2): 241-254.

Sleep, N. H. (2006). "Mantle plumes from top to bottom." Earth-Science Reviews 77(4): 231-271.

Sleep, N. H. and K. Zahnle (2001). "Carbon dioxide cycling and implications for climate on ancient Earth." J. Geophys. Res. **106**.

Smith, M. and P. Mosley (1993). "Crustal heterogeneity and basement influence on the development of the Kenya Rift, East Africa." Tectonics **12**(2): 591-606.

Solomatov, V. S. (1995). "Scaling of temperature- and stress-dependent viscosity convection." Physics of Fluids 7(2): 266-274.

Solomatov, V. S. and L. N. Moresi (1996). "Stagnant lid convection on Venus." J. Geophys. Res. **101**(E2): 4737-4753.

Solomon, S. C., M. A. Bullock, et al. (1999). "Climate Change as a Regulator of Tectonics on Venus." Science **286**(5437): 87-90.

Somerville, R. C. J., P. H. Stone, et al. (1974). "The GISS Model of the Global Atmosphere." Journal of the Atmospheric Sciences **31**(1): 84-117.

Squyres, S. W. and J. F. Kasting (1994). "Early Mars: How Warm and How Wet?" Science **265**(5173): 744-749.

Stephens, G. L., G. G. Campbell, et al. (1981). "Earth Radiation Budgets." J. Geophys. Res. **86**: 9739–9760.

Stephens, G. L. and T. J. Greenwald (1991). "The Earth's Radiation Budget and Its Relation to Atmospheric Hydrology 1. Observations of the Clear Sky Greenhouse Effect." J. Geophys. Res. **96**: 15,311–15,324.

Stevenson, D. J., T. Spohn, et al. (1983). "Magnetism and thermal evolution of the terrestrial planets." Icarus **54**(3): 466-489.

Thompson, A. B. (1992). "Water in the Earth's upper mantle." Nature **358**(6384): 295-302.

Torrance, K. E. and D. L. Turcotte (1971). "Thermal convection with large viscosity variations." Journal of Fluid Mechanics Digital Archive **47**(01): 113-125.

Tozer, D. C. (1972). "The present thermal state of the terestrial planets." Phys. Earth Planet. Interiors **6**: 182-197.

Turcotte, D. L. and E. R. Oxburgh (1967). "Finite amplitude convective cells and continental drift." Journal of Fluid Mechanics Digital Archive **28**(01): 29-42.

Turcotte, D. L. and G. Schubert (1982). Geodynamics: Applications of Continuum Physics to Geological Problems, John Wiley and Sons, New York.

Ulmer, P. and V. Trommsdorff (1995). "Serpentine stability to mantle depths and subduction-related magmatism." Science **268**(5212): 858.

Valley, J. W., W. H. Peck, et al. (2002). "A cool early Earth." Geology **30**(4): 351-354.

van Thienen, P., N. J. Vlaar, et al. (2004). "Plate tectonics on the terrestrial planets." Physics of The Earth and Planetary Interiors **142**(1-2): 61-74.

Vardavas, I. M. and J. H. Carver (1984). "Solar and terrestrial parameterizations for radiative-convective models." Planetary and Space Science **32**(10): 1307-1325.

Vink, G., W. Morgan, et al. (1984). "Preferential Rifting of Continents: A Source of Displaced Terranes." J. Geophys. Res. **89**(B12): 10072-10076.

Wildt, R. (1966). "The greenhouse effect in a gray planetary atmosphere." Icarus **5**(1-6): 24-33.

Yang, S.-K. and G. L. Smith (1985). "Further Study on Atmospheric Lapse Rate Regimes." Journal of the Atmospheric Sciences **42**(9): 961-966.

Yokohata, T., M. Odaka, et al. (2002). "Role of H_2O and CO_2 Ices in Martian Climate Changes." Icarus **159**(2): 439-448.

Zahnle, K. J., J. F. Kasting, et al. (1988). "Evolution of a steam atmosphere during earth's accretion." Icarus **74**(1): 62-97.

Zdunkowski, W. and A. Bott (2004). Atmospheric energetics of the hydrostatic equilibrium. Thermodynamics of the Atmosphere, Cambridge University Press: 226-233.

Zeebe, R. E., J. C. Zachos, et al. (2009). "Carbon dioxide forcing alone insufficient to explain Palaeocene-Eocene Thermal Maximum warming." Nature Geosci.

Zhou, Y. and R. D. Cess (2001). "Algorithm development strategies for retrieving the downwelling longwave flux at the Earth's surface." J. Geophys. Res. **106**: 12,477–12,488.

APPENDIX A

Numeric implementation of model

Part 1. Program diagram

MAIN Module

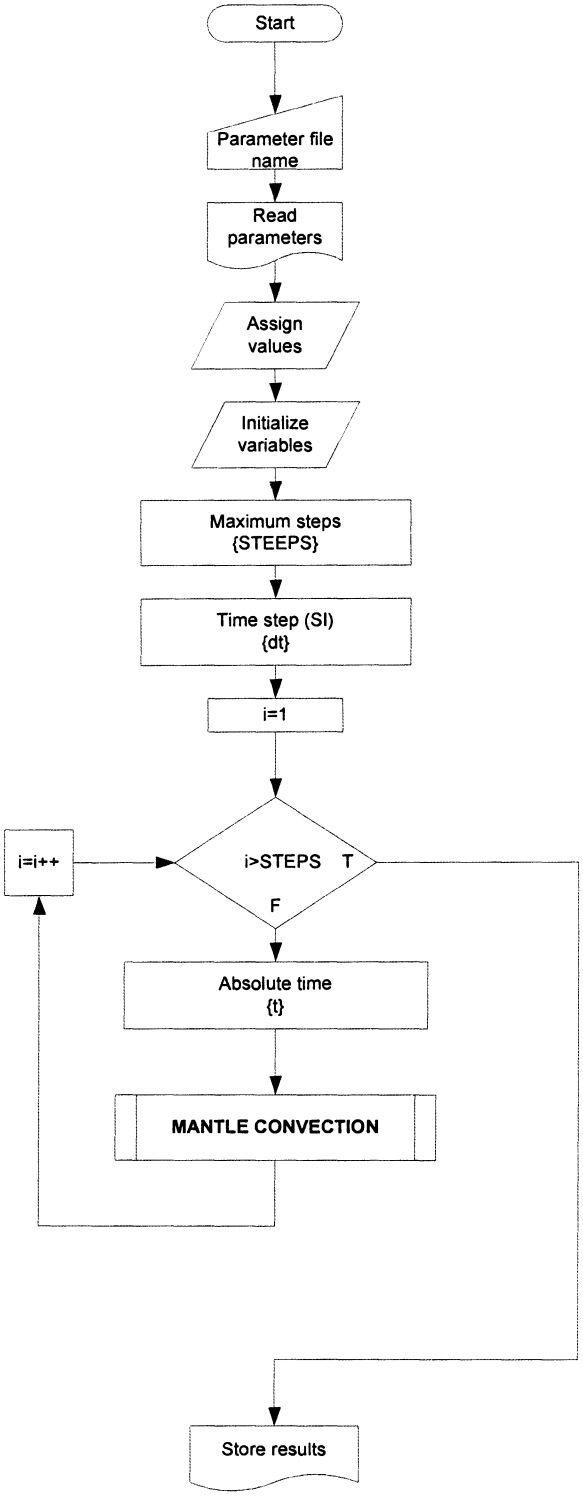
Start
Parameter file name
Read parameters
Assign values
Initialize variables
Maximum steps {STEEPS}
Time step (SI) {dt}
i=1
i=i++
i>STEPS T
F
Absolute time {t}
MANTLE CONVECTION
Store results

MANTLE CONVECTION Module

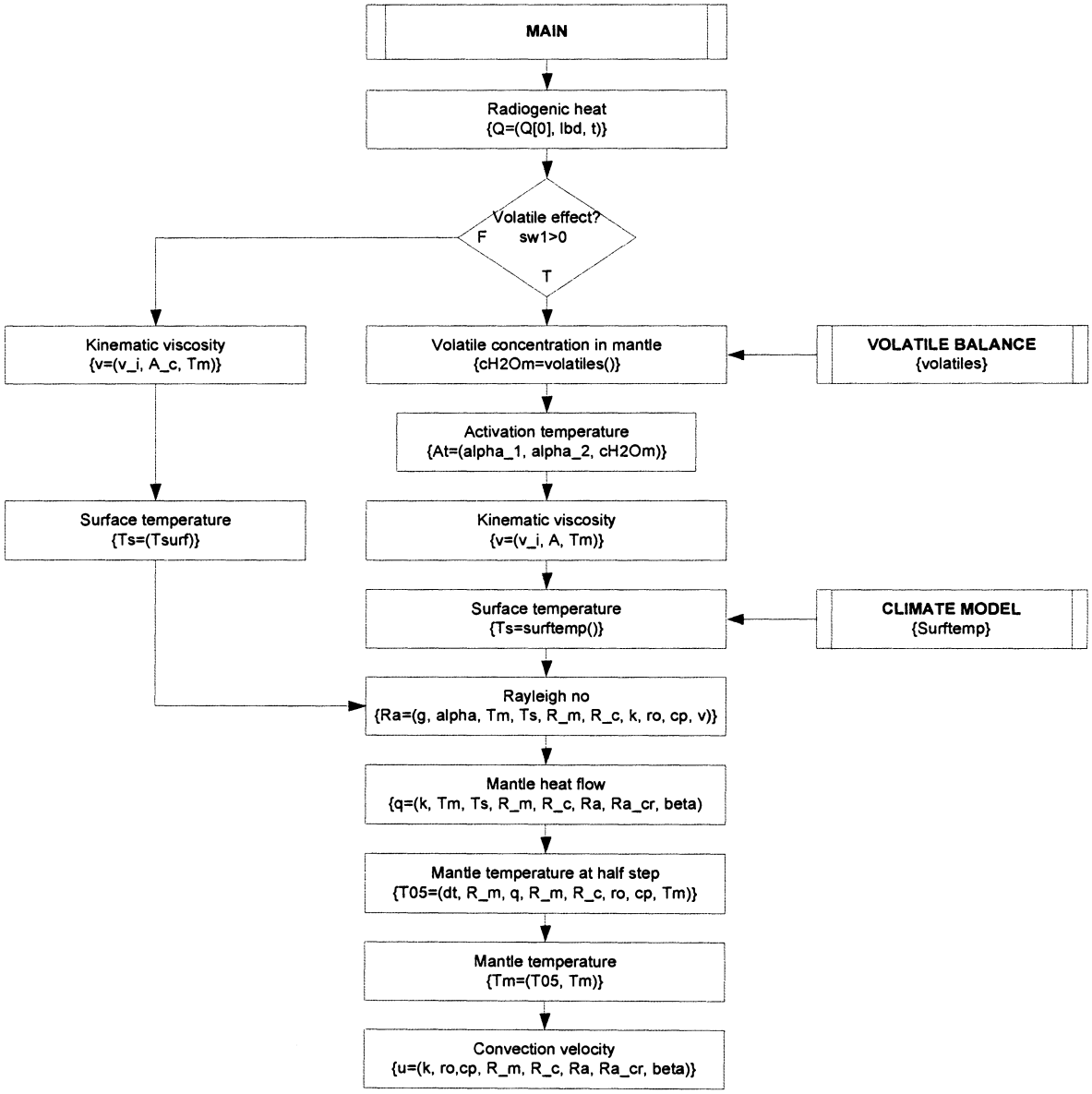

VOLATILE BALANCE Module

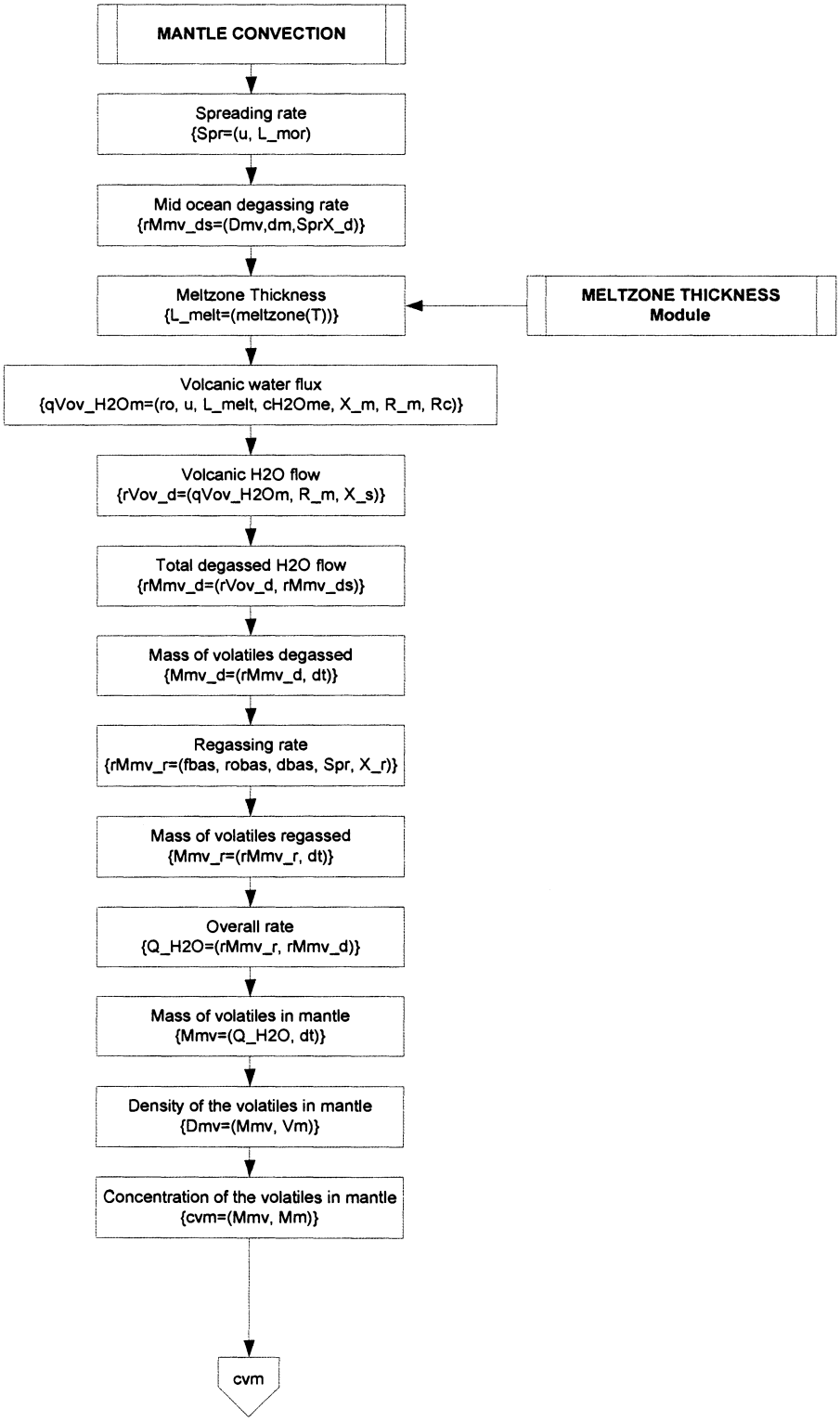

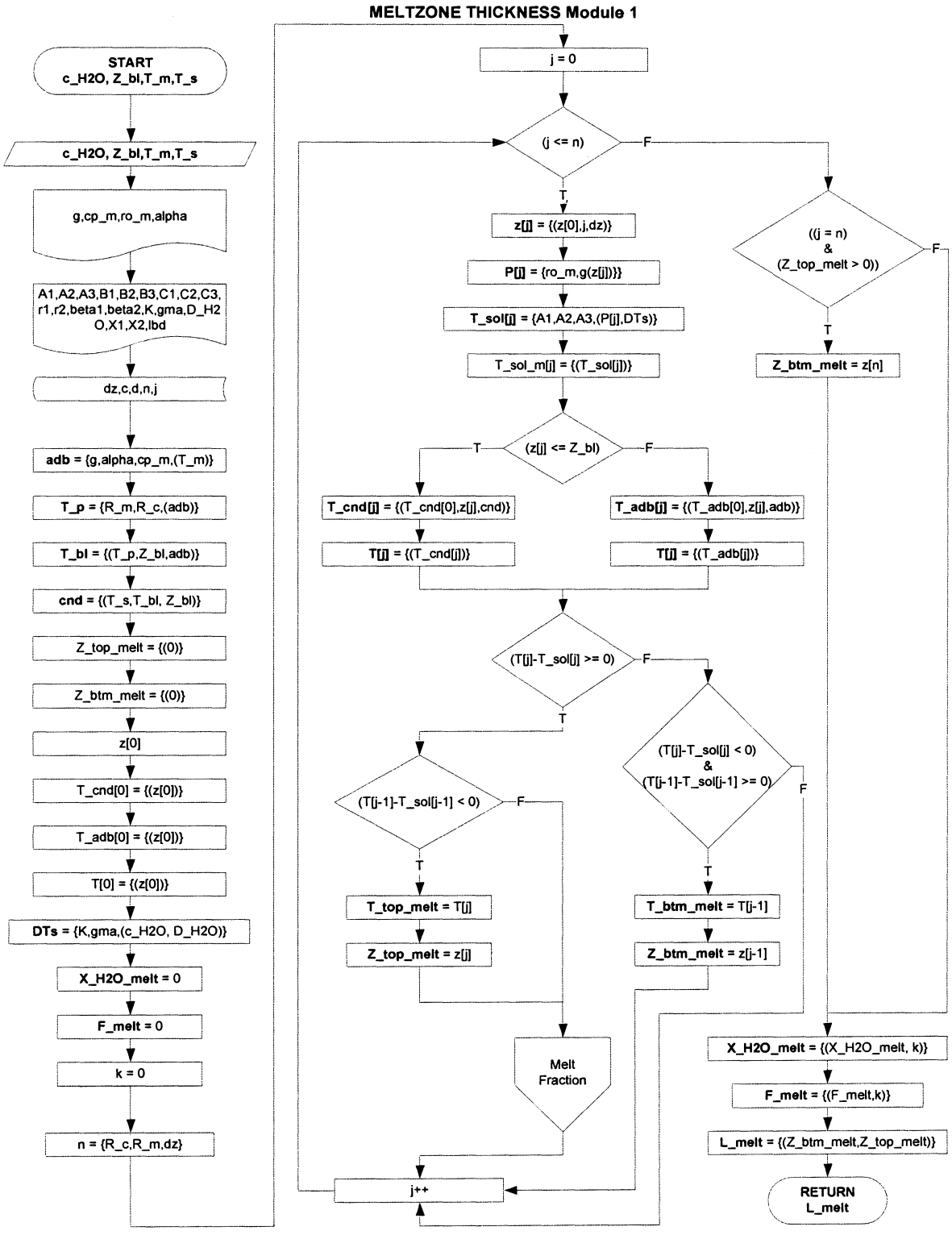
MELTZONE THICKNESS Module 1
START
c_H2O, Z_bl,T_m,T_s
c_H2O, Z_bl,T_m,T_s
g,cp_m,ro_m,alpha
A1,A2,A3,B1,B2,B3,C1,C2,C3,
r1,r2,beta1,beta2,K,gma,D_H2
O,X1,X2,lbd
dz,c,d,n,j
adb = {g,alpha,cp_m,(T_m)}
T_p = {R_m,R_c,(adb)}
T_bl = {(T_p,Z_bl,adb)}
cnd = {(T_s,T_bl, Z_bl)}
Z_top_melt = {(0)}
Z_btm_melt = {(0)}
z[0]
T_cnd[0] = {(z[0])}
T_adb[0] = {(z[0])}
T[0] = {(z[0])}
DTs = {K,gma,(c_H2O, D_H2O)}
X_H2O_melt = 0
F_melt = 0
k = 0
n = {R_c,R_m,dz}
j = 0
(j <= n)
F
T
z[j] = {(z[0],j,dz)}
P[j] = {ro_m,g(z[j])}
T_sol[j] = {A1,A2,A3,(P[j],DTs)}
T_sol_m[j] = {(T_sol[j])}
(z[j] <= Z_bl)
T
F
T_cnd[j] = {(T_cnd[0],z[j],cnd)}
T[j] = {(T_cnd[j])}
T_adb[j] = {(T_adb[0],z[j],adb)}
T[j] = {(T_adb[j])}
(T[j]-T_sol[j] >= 0)
F
T
(T[j-1]-T_sol[j-1] < 0)
F
T
T_top_melt = T[j]
Z_top_melt = z[j]
(T[j]-T_sol[j] < 0)
&
(T[j-1]-T_sol[j-1] >= 0)
F
T
T_btm_melt = T[j-1]
Z_btm_melt = z[j-1]
Melt
Fraction
j++
((j = n)
&
(Z_top_melt > 0))
F
T
Z_btm_melt = z[n]
X_H2O_melt = {(X_H2O_melt, k)}
F_melt = {(F_melt,k)}
L_melt = {(Z_btm_melt,Z_top_melt)}
RETURN
L_melt

MELTZONE THICKNESS Module 2

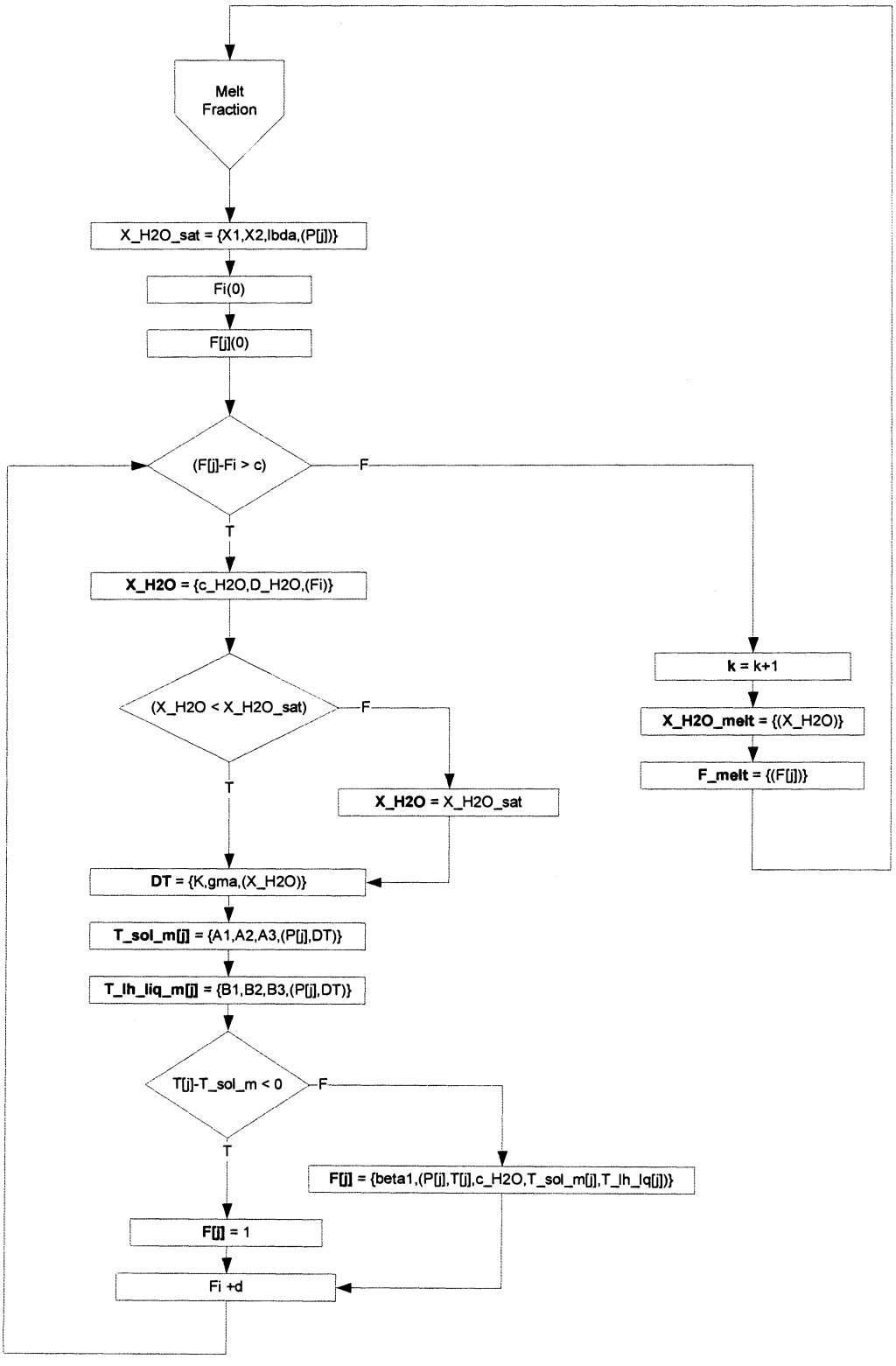

SURFACE TEMPERATURE Module

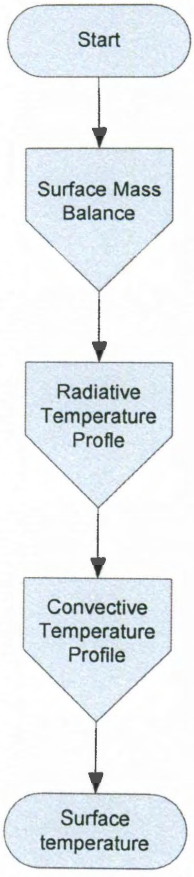

ATMOSPHERE PHYSICAL CHEMISTRY section

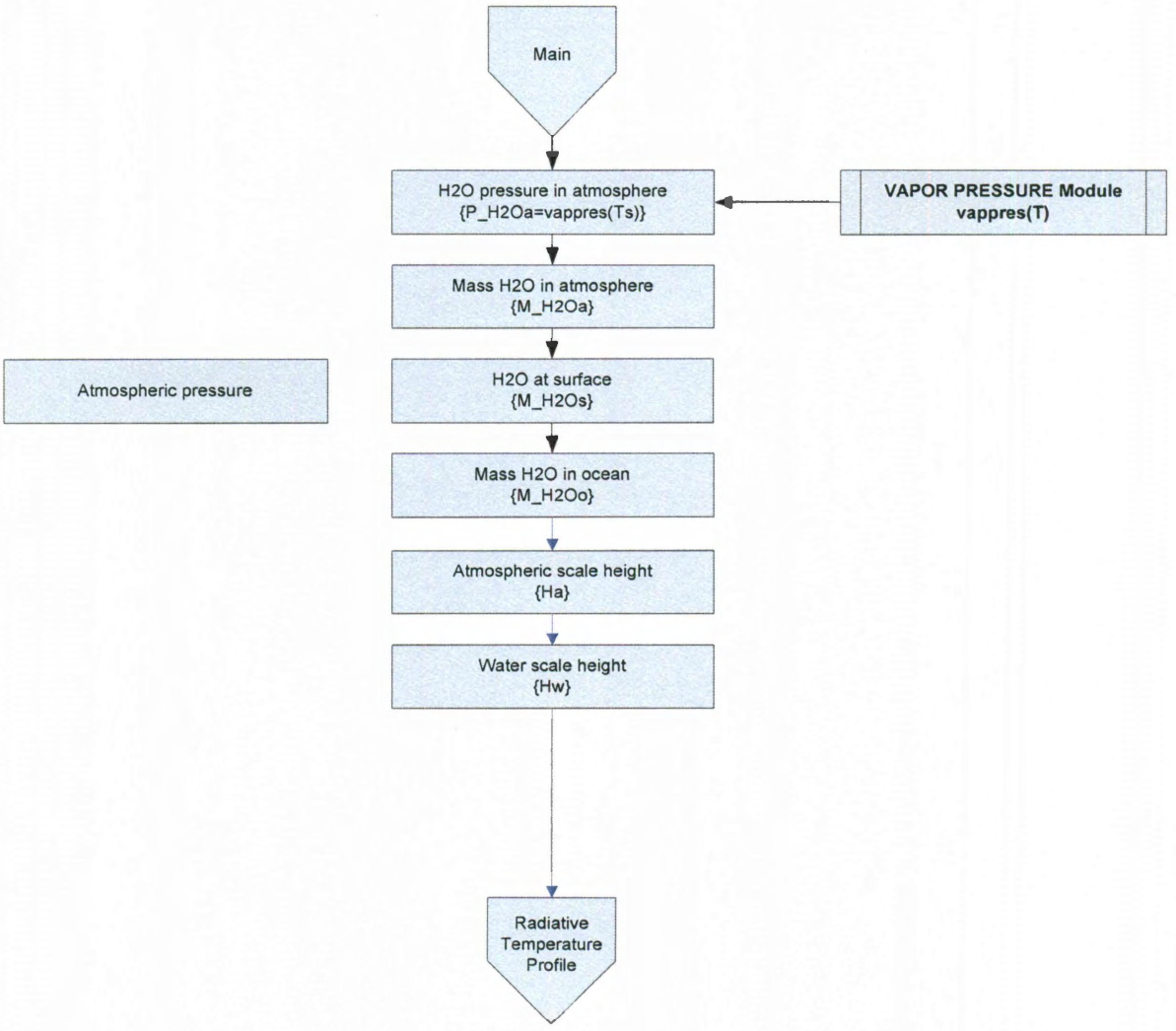

RADIATIVE TEMPERATURE PROFILE section

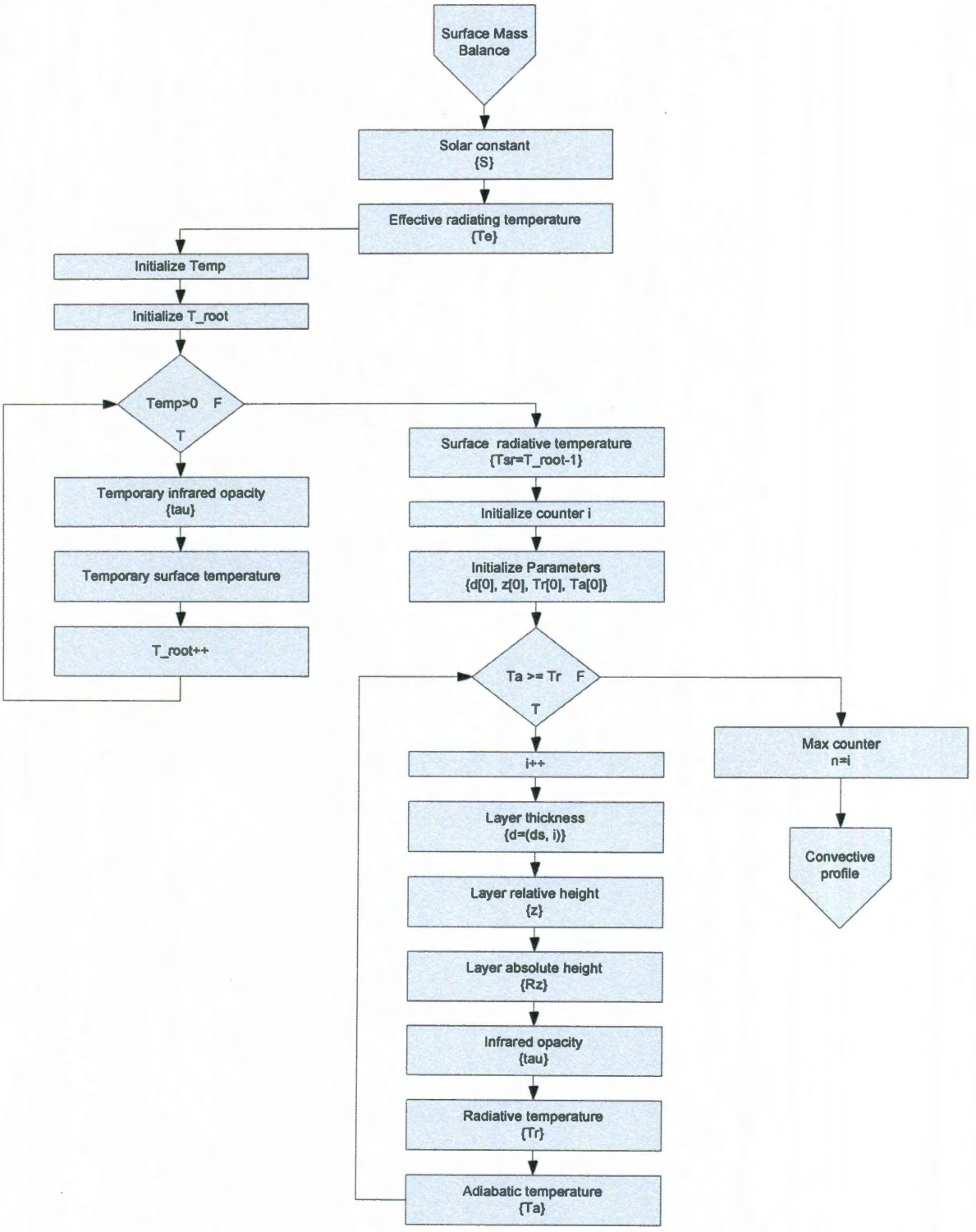

CONVECTIVE TEMPERATURE PROFILE section

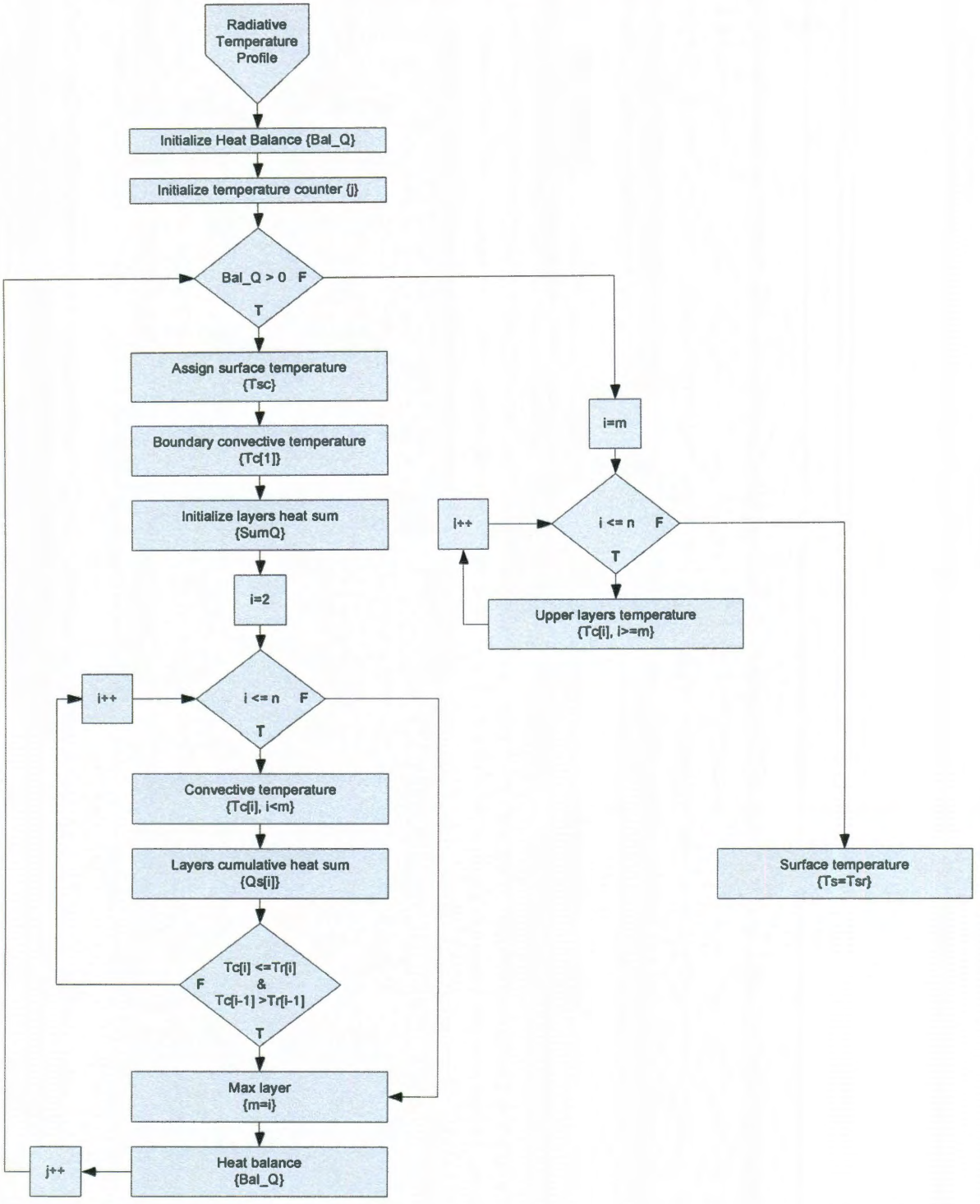

APPENDIX B

Numeric implementation of model

Part 2. Source code

thermevol.c

```
/*************************************************************************
 *   Copyright (C) 2007 by Constantin Sandu   *
 *   csandu@rice.edu   *
 *
 *************************************************************************/
/* 1D Thermal convection model */
/* Author: Constantin Sandu */

# include <stdio.h>
# include <math.h>
# include <string.h>
# include <globaldef.h>
# define NO_PARAM 60
# define PI 3.14
# define R 8.314

int main(int argc, char *argv[])
{

      double param[NO_PARAM];
      char FILE_NAME[80], INPUT_FILE[80],
OUTPUT_FILE_S[80],OUTPUT_FILE_M[80], one_line[100];
      unsigned long int i;
      double t_abs;
      unsigned short int sw1, sw2;
      unsigned long int h, t_start, t_end, STEPS;
      float ts, T_s_ini, T_m_ini, T_s, T_m;
      double c_H2O_m, M_N2_s_ini, M_O2_s_ini, M_CO2_s_ini, M_H2O_s_ini,
Z_sl_ini;
      float SOL_ini, r_SOL, Sol;
      double vi_m, M_H2O_m_ini;
      FILE *inp, *outps, *outpm;

      float surftemp(float S, double M_N2, double M_O2, double M_CO2, double
M_H2O);
      double visc(double cw, float T);
      float convection(float Ts, double vi);
      double volatiles(float Tm, float Ts, double uc);
      double vappres(double Tv);

/*printf("Enter the parameter file name: ");
scanf("%79s",FILE_NAME);*/

if (argc < 2)
{
printf("Input file argument not specified\n");
printf("Nothing done!\n");
return 1;
}

FILE_NAME[0] = '\0';
strcat(FILE_NAME, argv[1]);
strcpy(INPUT_FILE, FILE_NAME);
strcat (INPUT_FILE,".inp");
```

```
/*Read parameters*/

inp = fopen(INPUT_FILE,"r");
if (inp == NULL)
{
printf("Could not find input file: %s\n", INPUT_FILE);
printf("Nothing done!\n");
return 2;
}
else
printf("Input file is: %s\n", INPUT_FILE);

for (h=1; h<=(NO_PARAM-1); h++)
      {
      (void) fgets(one_line, sizeof(one_line), inp);
      (void) sscanf(one_line, "%le\n", &param[h]);
    /* printf("constant %i is %g\n", h, param[h]); */
      }
fclose(inp);

sw1 = param[1];          /* Climate effect */
sw2 = param[2];          /*  Mantle volatile effect */
sw3 = param[3];          /* Viscosity law */
sw4 = param[4];          /*  Areal Spreading law */
sw5 = param[5];          /*  Degassing */
sw6 = param[6];          /*  Regassing */
sw7 = param[7];          /*  Stagnant lid */

/* Initial and boundary condition  */
t_start = param[8];                  /* Start time [Ma]    */
t_end = param[9];              /* End time [Ma]     */
T_m_ini = param[10];                 /* Initial mantle temperature [K] */
T_s_ini = param[11];                 /* Surface temperature [K]  */
Qr_m_ini = param[12];          /* Initial radioactive heat [J/(m^3*s)] */
M_N2_s_ini = param[13];        /* Mass of initial N2 at surface [kg] */
M_O2_s_ini = param[14];        /* Mass of initial O2 at surface [kg] */
M_CO2_s_ini = param[15];       /* Mass of initial CO2 at surface [kg] */
M_H2O_s_ini = param[16];       /* Mass of initial H2O at surface [kg] */
M_H2O_m_ini = param[17];       /* Mass of initial H2O in mantle [kg] */
SOL_ini = param[18];           /* Initial solar radiation */
/* Model parameters */
/* Planetary constants */
g = param[19];                       /* Gravity constant [m*s^-2] */
R_c = param[20];               /* Lower mantle boundary */
R_m = param[21];               /* Upper mantle boundary */
ro_m = param[22];              /* Mantle density [kg*m^-3] */
k_m = param[23];                     /* Thermal conductivity [W/m/K] */
cp_m = param[24];              /* Specific heat [J/kg/K]  */
/* Mantle convection constants */
alpha = param[25];                   /* Coefficient of thermal expansion [K^-
1] */
a = param[26];
b = param[27];
beta = param[28];              /* Scaling factor     */
lbd = param[29];               /* Radioactive decay constant[s^-1] */
Ra_cr = param[30];                   /* Critical Ra */
eta0 = param[31];              /* Viscosity constant [m^2/s]    */
```

```
Acre = param[32];       /*  */
r = param[33];          /*     */
AE_c = param[34];             /*  */

/* Climate constants */
tau_ex = param[35];
abd = param[36];
ems = param[37];
k_CO2 = param[38];
k_H2O = param[39];
r_SOL = param[40];
rh = param[41];

/* Volatile circulation constants */
d_melt = param[42];                 /* Equivalent depth of melt */
f_bas = param[43];                  /* Fraction of volatile in basalt */
ro_bas = param[44];                 /* Density of basalt */
d_bas = param[45];                  /* Average thickness of basaltic crust */
Xt_d = param[46];             /* Regassing efficiency factor */
Xt_r = param[47];             /* Degassing efficiency factor */
Xs_d = param[48];             /* Regassing efficiency factor */
Xs_r = param[49];
tau_cr = param[50];
Z_sl_ini = param[51];

/* Grid definition parameters   */
ts = param[52];               /* Time step (elem. time interval Ma) */
ds = param[53];
dT = param[54];
dz = param[55];


/* Start */

M_o = 1.39E+021;
S_m = 4*PI*pow(R_m,2);
V_m = PI*(pow(R_m,3)-pow(R_c,3))*4/3;
M_m = 1.58*ro_m*V_m;    /* 4.06E+24 */
printf("Mantle mass is %e\n", M_m);

/* Initialize system */
t_abs = t_start;
T_s = T_s_ini;
M_H2O_s = M_H2O_s_ini;
M_H2O_a = rh*vappres(T_s)*S_m/g;
if (M_H2O_s < M_H2O_a)
      M_H2O_a = M_H2O_s;

Qm_H2O_m = 0;

T_m = T_m_ini;
vi_m = eta0;
M_H2O_d = 0;
M_H2O_r = 0;
M_H2O_m = M_H2O_m_ini;
c_H2O_m = M_H2O_m/M_m;
T_sl = T_s;
```

```
Z_sl = Z_sl_ini;
tau = tau_cr;

strcpy(OUTPUT_FILE_S, FILE_NAME);
strcat(OUTPUT_FILE_S,".out.atmosphere.dat");
outps = fopen(OUTPUT_FILE_S,"w");
fprintf(outps, "t_abs, Te, Qm_H2O_m, Qm_H2O_ex, M_H2O_s, M_H2O_a, M_H2O_o,
P_H2O_a, P_atm, H_atm, H_H2O_a, Tsr, Z_tropo,  T_s\n");

strcpy(OUTPUT_FILE_M, FILE_NAME);
strcat(OUTPUT_FILE_M,".out.mantle.dat");
outpm = fopen(OUTPUT_FILE_M,"w");
fprintf(outpm, "t_abs, vi_m, Ra, Nu, q_m, Ur, T_m, T_bl, Z_bl, T_sl, Z_sl,
uc_m, tau, spr, Qm_H2O_d, M_H2O_d, L_hydr, Qm_H2O_r, M_H2O_r, Qm_H2O_m,
M_H2O_m, c_H2O_m, X_H2O_melt, Z_top_melt, Z_btm_melt, T_top_melt, T_btm_melt,
L_melt, F_melt, Tect\n");

/*Processing*/

STEPS = (t_end-t_start)/ts;
dt = ts*1E+6;

for (i=1; i<=STEPS; i++)
    {

      t_abs = t_start+i*ts;
printf("Running %.1f MA \n", t_abs);
      t = i*dt;
      Sol = SOL_ini+r_SOL*ts*i;
printf("          Sol= %.1f  \n", Sol);
printf("          M_H2O_s %.2f (OM)\n", M_H2O_s/M_o);
      if (sw1 > 0)
            {
            T_s = surftemp(Sol, M_N2_s_ini, M_O2_s_ini, M_CO2_s_ini,
M_H2O_s);
            }
printf("          T_s= %.1f (K) \n", T_s);
      cwmi = c_H2O_m;
      vi_m = visc(cwmi, T_m);
      /*vi_m = 2.21E7*exp(58000/T_m);*/
printf("          eta_eff= %e (Pa*s)\n", vi_m*ro_m);
printf("          vi_m= %e (m^2/s)\n", vi_m);
      if (sw2 > 0)
            {
            c_H2O_m = volatiles(T_m, T_s, uc_m);
            }

printf("          M_H2O_m= %.2f \n", M_H2O_m/M_o);
      Tmi = T_m;
      T_m = convection(T_s, vi_m);
printf("          T_m= %.1f (K)\n", T_m);
printf("          q_m= %.1f (mW/m^2)\n", q_m*1000);


      /* Output results */
      fprintf(outps, "%.1f, %.2f, %e, %e, %e, %e, %e, %e, %e, %e, %e, %.2f,
%e, %.2f\n", //
```

```
                                t_abs, Te, Qm_H2O_m, Qm_H2O_ex, M_H2O_s/M_o,
M_H2O_a, M_H2O_o/M_o, P_H2O_a, P_atm, //
                                H_atm, H_H2O_a, Tsr, Z_tropo,  T_s);

      fprintf(outpm, "%.1f, %e, %e, %e, %e, %.2f, %.2f, %.2f, %e, %.2f, %e,
%e, %e, %e, %e, %e, %e, %e, %e, %e, %e, %e, %e, %e, %e, %e, %e, %e, %.3f,
%i\n", //
                                t_abs, vi_m, Ra, Nu, q_m*1000, Ur, T_m, T_bl, -
Z_bl/1000, T_sl, -Z_sl/1000, uc_m*100, tau, //
                                spr, Qm_H2O_d, M_H2O_d/M_o, -L_hydr/1000,
Qm_H2O_r,  M_H2O_r/M_o, //
                                Qm_H2O_m, M_H2O_m/M_o, c_H2O_m, X_H2O_melt, -
Z_top_melt/1000, -Z_btm_melt/1000, T_top_melt, T_btm_melt, L_melt/1000,
F_melt, sw7);
    }

fclose(outps);
fclose(outpm);
/*printf("Mantle mass is %e\n", M_m);*/
printf("Heat flux is %.1f mW/m^2/s\n", q_m*1000);
printf("Mantle temperature is %.1f K\n", T_m);
printf("Surface temperature is %.1f K\n", T_s);
printf("Output files saved as: %s and %s\n", OUTPUT_FILE_S, OUTPUT_FILE_M);
printf("Done!\n");
printf("**********************************************************************
*\n");

return 0;
}
```

globaldef.h

```
/*****************************************************************************
 *   Copyright (C) 2007 by Constantin Sandu   *
 *   csandu@rice.edu   *
 *                                                                           *
 *****************************************************************************/
# define MAX_LAYERS 100000

int sw3, sw4, sw5, sw6, sw7;
/* General */
double g;
double R_c, R_m, S_m, V_m, M_m, M_o;
double dt, t, dz;

/* Surftemp */
double abd, ems, rh;
double k_CO2, k_H2O, tau_ex;
float ds, dT;
double M_H2O_s_ini, Qm_H2O_ex;
      /* Output */
float Te, T0, Tsr;
double P_atm, H_atm, Z_tropo, M_H2O_a, P_H2O_a, H_H2O_a, M_H2O_a;
double zl[MAX_LAYERS], Tr[MAX_LAYERS], Ta[MAX_LAYERS], Tc[MAX_LAYERS];
unsigned short int nol;
/* Convection */
double dt, t;
float a, b, beta;
double ro_m, k_m, cp_m, alpha;
double Qr_m_ini, lbd, vi0, alpha_1, alpha_2;
double Ra_cr, tau_cr;

float Tmi, T_bl, Ur, T_sl;
      /* Output */
double Qr_m, q_m, Z_bl, uc_m, tau, Z_sl;
double Ra, Nu;
/* visc*/

double Acre, r, AE_c, eta0;
/* Volatiles */
double f_bas, ro_bas, cwmi, d_melt, d_bas;
float Xt_d, Xt_r, Xs_d, Xs_r;
      /* Output */
double M_H2O_d, M_H2O_r, M_H2O_m, M_H2O_s, M_H2O_o;
double L_melt, L_hydr;
double Qm_H2O_d, Qm_H2O_r, Qm_H2O_m;
double spr;
/* meltzone */
double dz;
/* output */
double Z_top_melt, Z_btm_melt;
float T_top_melt, T_btm_melt;
double X_H2O_melt;
float F_melt;
```

convection.c

```
/*****************************************************************************
 *   Copyright (C) 2007 by Constantin Sandu   *
 *   csandu@rice.edu   *
 *
 *****************************************************************************/
# include <math.h>
# include <stdio.h>
# define R 8.314

float convection(float Ts, double vi)
{
      float Tm;
      /* Input */
      extern int sw7;
      extern double dt, t;
      extern double g;
      extern float a, b, beta;
      extern double ro_m, k_m, cp_m, alpha;
      extern double Qr_m_ini, lbd;
      extern double AE_c, tau_cr;
      extern double Ra_cr, R_c, R_m;
      extern float Tmi, Ur;
      /* Output */
      extern double Qr_m, q_m, Z_bl, uc_m, tau, Z_sl;
      extern double Ra, Nu;
      extern float T_bl, T_sl;
      /* Internal param */
      float Tm05;
      double theta;
      double H_in, H_out;
      double tau_sub05;

            theta = AE_c/(R*pow(Tmi,2))*(Tmi-Ts);


            if (T_sl < Ts)
                  T_sl = Ts;

            if (sw7 == 0) /* Thin lid */
            {
            T_sl = Ts;
            Z_sl = 0;
            }
            else /* Stagnant lid */
            {
            /*T_sl = Tmi-2.23*R*Tmi*Tmi/AE_c;*/
            T_sl = Tmi-8/(theta/(Tmi-Ts));
            }

            Qr_m = Qr_m_ini*exp(-lbd*t);

            /*Ra =(g*alpha*Qr_m/(365*24*3600)*pow((R_m-Z_sl-
R_c),5))/(vi*k_m*k_m/ro_m/cp_m);*/
            Ra =(g*alpha*(Tmi-T_sl)*pow((R_m-Z_sl-
R_c),3))/(vi*k_m/ro_m/cp_m);
```

```
            Nu = a*pow(theta,b)*pow((Ra/Ra_cr),beta);

            q_m = k_m*(Tmi-T_sl)/(R_m-Z_sl-R_c)*Nu;

            H_in = Qr_m*(pow(R_m,3)-pow(R_c,3));
            H_out = 3*pow(R_m,2)*q_m*365*24*3600;
            Ur = H_in/H_out;
            Tm05 = 0.5*dt*(H_in-H_out)/(ro_m*cp_m*(pow(R_m,3)-
pow(R_c,3)))+Tmi;
            Tm = 2*Tm05-Tmi;
            T_bl = Tm;
            /*T_bl = 1.05*(Tm-g*alpha*Tm/cp_m*(R_m-R_c)/2);*/
            Z_bl = k_m*(T_bl-Ts)/q_m;
            tau_sub05 = pow(Z_bl,2)/(2.32*2.32*k_m/(ro_m*cp_m));
            /*tau_sub05 = pow(k_m*(Tb-
Ts),2)/(k_m/(ro_m*cp_m)*M_PI*pow(q_m,2));*/
            /*Z_bl=2.32*sqrt(k_m/(ro_m*cp_m)*tau_sub05);*/
            /*uc_m = k_m/ro_m/cp_m/(R_m-R_c)*pow((Ra/Ra_cr),(1-
beta))*365*24*3600;*/
            uc_m = (R_m-R_c)/(2*tau_sub05)*365*24*3600;
            /*uc_m = 0.45*pow(theta,-
0.72)*pow((Ra/Ra_cr),0.58)*365*24*3600;*/
            tau = ro_m*vi*uc_m/(R_m-R_c)/(365*24*3600);
            Z_sl = k_m*(T_sl-Ts)/q_m;


            if (tau > tau_cr)
                  sw7 = 0;
            else
                  sw7 = 1;

      return Tm;
}
```

meltzone.c

```
/*****************************************************************************
 *   Copyright (C) 2007 by Constantin Sandu   *
 *   csandu@rice.edu   *
 *
 *****************************************************************************/
# include <math.h>
# include <stdio.h>
# define A1 1085.7
# define A2 132.9
# define A3 -5.1
# define B1 1475
# define B2 80
# define B3 -3.2
# define C1 1780
# define C2 45
# define C3 -2
# define r1 0.5
# define r2 0.08
# define beta1 1.5
# define beta2 1.5
# define K 43
# define gma 0.75
# define D_H2O 0.01
# define X1 12
# define X2 1
# define lbda 0.6
# define d 0.0001
# define Z_max 300000
# define MAX_LAYERS 3001

double meltzone(double  cwaterm, double Zbl, float Tmantle, float Tsurf)
{
      double L;
      /* input */
      extern double g;
      extern double R_c, R_m;
      extern double cp_m, ro_m, alpha;
      extern double dz;
      extern float T_bl;

      /* output */
      extern double Z_top_melt, Z_btm_melt;
      extern float T_top_melt, T_btm_melt;
      extern double X_H2O_melt;
      extern float F_melt;
      /* intern */
      float adb, T_p, cnd, DTs, DT;
      double z[MAX_LAYERS], P_geo[MAX_LAYERS], T_cnd[MAX_LAYERS],
T_adb[MAX_LAYERS];
      double T[MAX_LAYERS], T_sol[MAX_LAYERS], T_sol_m[MAX_LAYERS];
      double T_lh_liq[MAX_LAYERS], T_lh_liq_m[MAX_LAYERS];
      float Fi, F[MAX_LAYERS];
      float T_lh_liq_melt;
      double X_H2O, X_H2O_sat;
      unsigned short int n, j, k;
```

```
float Tsolidus(float dT, double P);
float Tlhliquidus(float dT, double P);

cwaterm = cwaterm*100;
adb = g*alpha*Tmantle/cp_m;
T_p = Tmantle-adb*(R_m-R_c)/2;

cnd = (T_bl-Tsurf)/Zbl;

Z_top_melt = 0;
Z_btm_melt = Z_top_melt;
z[0] = 0;
P_geo[0] = ro_m*g*z[0]*1E-9;
T_cnd[0] = Tsurf;
T_adb[0] = T_p;
T[0] = T_cnd[0];

DTs = K*pow((cwaterm/D_H2O),gma);
T_sol[0] = Tsolidus(DTs, P_geo[0]);
T_sol_m[0] = T_sol[0];
T_lh_liq[0] = Tlhliquidus(DTs, P_geo[0]);
T_lh_liq_m[0] = T_lh_liq[0];
X_H2O_melt = 0;
F_melt = 0;
k = 0;

n = Z_max/dz;
for (j=1; j<=n; j++)
{
      L = Z_btm_melt-Z_top_melt;
      if (L > 0)
            break;
      z[j] = j*dz;
      P_geo[j] = ro_m*g*z[j]*1E-9;
      T_sol[j] = Tsolidus(DTs, P_geo[j]);
      T_sol_m[j] = T_sol[j];
      T_lh_liq[j] = Tlhliquidus(DTs, P_geo[j]);
      T_lh_liq_m[j] = T_lh_liq[j];
      if (z[j] <= Zbl)
      {
            T_cnd[j] = T_cnd[0]+(z[j]-z[0])*cnd;
            T[j] = T_cnd[j];
      }
      else
      {
            T_adb[j] = T_adb[0]+(z[j]-z[0])*adb;
            T[j] = T_adb[j];
      }
      if ((T[j]-T_sol[j]) >= 0)
      {
            if (T[j-1]-T_sol[j-1] < 0)
            {
                  T_top_melt = T[j];
                  Z_top_melt = z[j];
                  T_btm_melt = T[j];
```

```
                        Z_btm_melt = z[j];
                  }

                  X_H2O_sat = X1*pow(P_geo[j],lbda)+X2*P_geo[j];
                  F[j] = 1;
                  Fi = 0;
                  while ((F[j]-Fi)>0)
                  {
                        X_H2O = cwaterm/(D_H2O+Fi*(1-D_H2O));
                        if ((X_H2O-X_H2O_sat) >=0)
                              X_H2O = X_H2O_sat;
                        DT = K*pow(X_H2O,gma);
                        T_sol_m[j] = Tsolidus(DT, P_geo[j]);
                        T_lh_liq_m[j] = Tlhliquidus(DT, P_geo[j]);
                        if (T[j] - T_sol_m[j] < 0)
                        {
                              F[j] = 0;
                              break;
                        }
                        if (Fi >= 1)
                        {
                              F[j] = 1;
                              break;
                        }
                        else
                              F[j] = pow(((T[j]-T_sol_m[j])/(T_lh_liq[j]-
T_sol[j])),beta1);
                        Fi = Fi+d;
                  }
                  k = k+1;
                  X_H2O_melt = X_H2O_melt+X_H2O;
                  F_melt = F_melt+F[j];


            }
            else
            {
                  if (((T[j]-T_sol[j]) < 0) && ((T[j-1]-T_sol[j-1]) >= 0))
                  {
                        T_btm_melt = T[j];
                        Z_btm_melt = z[j];
                  }
            }
      }
      if ((j-1 == n) && (Z_top_melt > 0) && (L == 0))
      {
            T_btm_melt = T[n];
            Z_btm_melt = z[n];
            L = Z_btm_melt-Z_top_melt;
      }

      if (L == 0)
      {
            X_H2O_melt = 0;
            F_melt = 0;
      }
      else
```

```
        {
                X_H2O_melt = X_H2O_melt/k*0.01;
                F_melt = F_melt/k;
        }
        return L;
}

float Tsolidus(float dTw, double P)
{
        float Tso;
        Tso = (A1+A2*P+A3*pow(P,2)-dTw)+273;
        return Tso;
}

float Tlhliquidus(float dTw, double P)
{
        float Tll;
        Tll = (B1+B2*P+B3*pow(P,2)-dTw)+273;
        return Tll;
}
```

vappress.c

```
/*************************************************************************
 *   Copyright (C) 2007 by Constantin Sandu   *
 *   csandu@rice.edu   *
 *
 *************************************************************************/
# include <math.h>

double vappres(double Tv)
{
double Pv, k;

k = 10.40221-(1838.675/(Tv-31.737));
Pv = pow(10,k);
return Pv;
}
```

visc.c

```
/*************************************************************************
 *   Copyright (C) 2007 by Constantin Sandu   *
 *   csandu@rice.edu   *
 *
 *************************************************************************/
# include <math.h>
# include <stdio.h>
# define m_H2O 18.02E-3
# define m_Fe2SiO4 204.0E-3
# define m_Mg2SiO4 140.0E-3
# define r_Fe2SiO4 0.1
# define r_Mg2SiO4 0.9
# define c0 -7.9859
# define c1 4.3559
# define c2 -0.5742
# define c3 0.0337
# define R 8.314
# define vict 2.21E7


double visc(double cw, float T)
{
      double vi_kin;
      /* Input */
      extern int sw3;
      extern double ro_m;
      extern double AE_c, Acre, r, eta0, tau;
      /* Output */
      extern double Qr_m,  vi_m, Ra, q_m, uc_m;
      /* Internal param */
      double m_m, C_OH, voldep, tempdep;
      float lnfH2O, gma, eta_eff;
switch(sw3)
      {
      default:
            m_m = (m_Fe2SiO4*r_Fe2SiO4+m_Mg2SiO4*r_Mg2SiO4);
            C_OH = (cw*m_m*1E6*2)/m_H2O;
            lnfH2O =
c0+c1*log(C_OH)+c2*pow((log(C_OH)),2)+c3*pow((log(C_OH)),3);
            gma = AE_c/(R*pow(T,2));
            voldep = 1/(Acre*pow((exp(lnfH2O)),r));
            tempdep = 1/exp(-gma*T);
            eta_eff = eta0*voldep*tempdep;
            vi_kin = eta_eff/ro_m;
            break;
      case 1:
            vi_kin = vict*exp((6.4e4-6.1e6*cw)/T);
            break;
      case 2:
            vi_kin = vict*exp((6.4e4-8.1e5*cw)/T);
            break;
      case 3:
            eta_eff = 80/(3*5.3e6)*pow((1/5e-
7),2.5)*exp((240e3+3.1*5e3)/(R*T));
```

```
            vi_kin = eta_eff/ro_m;
            break;
        }

return vi_kin;
}
```

volatiles.c

```
/*************************************************************************
 *   Copyright (C) 2007 by Constantin Sandu   *
 *   csandu@rice.edu   *
 *
 *************************************************************************/
# include <math.h>
# define MORL 6E+7
# define TSERP 870
# define DCRACK 20000
# include <stdio.h>

double volatiles(float Tm, float Ts, double uc)
{

      double cwm;
      /* Input */
      extern int sw4, sw5, sw6, sw7;
      extern double ro_m, k_m, R_c, R_m, S_m, V_m, M_m;
      extern double dt, t;
      extern double f_bas, ro_bas, cwmi, d_melt, d_bas;
      extern float Xt_d, Xt_r, Xs_d, Xs_r;
      extern double Z_bl, q_m;
      extern double tau_ex;
      extern double M_H2O_s_ini, Qm_H2O_m;
      extern float T_s;
      extern double X_H2O_melt, Z_btm_melt;
      extern float F_melt;

      /* Output */
      extern double M_H2O_d, M_H2O_r, M_H2O_m, M_H2O_s, M_H2O_o, M_H2O_a;
      extern double L_melt, L_hydr;
      extern double Qm_H2O_d, Qm_H2O_r, Qm_H2O_m, Qm_H2O_ex;
      extern double q_m, spr;
      /* Internal param */
      float X_d, X_r;
      double Ao;
      double Dm_H2O_m, qm_H2O_dv, D_melt;
      /* Functions */
      double meltzone(double  cwaterm, double Zbl, float Tmantle, float
Tsurf);

      if (sw7 == 1)
      {
            X_d = Xs_d;
            X_r = Xs_r;
            D_melt = Z_bl;
      }
      else
      {
            X_d = Xt_d;
            X_r = Xt_r;
            D_melt = 500;
      }
      if (sw4 == 0)
            spr = 2*uc*MORL;
```

```
      else
            {
            Ao =
3.1E+14*pow((7.75E+17/1.1687E+18+3.937E+17*0.07/1.1687E+18/q_m),-1);
            spr = pow(q_m,2)*3.14*1E-6*Ao/pow(2*4.2*(Tm-273),2)*365*24*3600;
            }

/* Outgassing */

      if (sw5 == 0)
            {
            L_melt = meltzone(cwmi, D_melt, Tm, Ts);
            Qm_H2O_d = ro_m*F_melt*X_H2O_melt*L_melt*spr*X_d;
            }
      else
            {
            L_melt = d_melt;
            Qm_H2O_d = M_H2O_m/V_m*L_melt*spr;
            }

      M_H2O_d = M_H2O_d+Qm_H2O_d*dt;

/* Regassing */

      if (sw6 == 0)
            {
            L_hydr = k_m*(TSERP-Ts)/q_m;
            if (L_hydr > Z_bl)
                  L_hydr = Z_bl;
            if (L_hydr > DCRACK)
                  L_hydr = DCRACK;
            Qm_H2O_r = f_bas*ro_bas*L_hydr*spr*X_r;
            }
      else
            L_hydr = d_bas;
            Qm_H2O_r = f_bas*ro_bas*L_hydr*spr*X_r;

      M_H2O_r = M_H2O_r+Qm_H2O_r*dt;

/* Total*/

      Qm_H2O_m = Qm_H2O_d-Qm_H2O_r;
      M_H2O_m = M_H2O_m-Qm_H2O_m*dt;
      if (M_H2O_m < 0)
            M_H2O_m = 0;

      Qm_H2O_ex = M_H2O_a*(1-exp(-dt/tau_ex))/dt;
      M_H2O_s = M_H2O_s+(Qm_H2O_m-Qm_H2O_ex)*dt;
      M_H2O_o = M_H2O_s-M_H2O_a;

    cwm = M_H2O_m/M_m;
      return cwm;
}
```

atmtemp.c

```
/*************************************************************************
 *   Copyright (C) 2007 by Constantin Sandu   *
 *   csandu@rice.edu   *
 *
 *************************************************************************/

/* Standard climate model */
/* Author: Constantin Sandu */

# define _USE_MATH_DEFINES
# include <stdio.h>
# include <math.h>
# include <string.h>
# include <surftemp.h>
# define NO_PARAM 20

int main(int argc, char *argv[])
{
      double param[NO_PARAM];
      char FILE_NAME[80], INPUT_FILE[80], OUTPUT_FILE[80], one_line[100];
      unsigned short int h, j;
      float Sol, T_s, Tsi0;
      double M_N2_s, M_O2_s, M_Ar_s, M_CO2_s, M_H2O_s;
      float surftemp(float S, double M_N2, double M_O2, double M_Ar_s, double
M_CO2, double M_H2O);
      FILE *inp, *outp;


/* printf("Enter the parameter file name: ");
scanf("%79s",FILE_NAME);*/

if (argc < 2)
{
printf("Input file argument not specified\n");
printf("Nothing done!\n");
return 1;
}

FILE_NAME[0] = '\0';
strcat(FILE_NAME, argv[1]);

strcpy (INPUT_FILE, FILE_NAME);
strcat (INPUT_FILE,".inp");

inp = fopen(INPUT_FILE,"r");
if (inp == NULL)
{
printf("Could not find input file: %s\n", INPUT_FILE);
printf("Nothing done!\n");
return 2;
}
else
printf("Input file is: %s\n", INPUT_FILE);

/*Read parameters*/
```

```
for (h=1; h<=(NO_PARAM-1); h++)
      {
      (void) fgets(one_line, sizeof(one_line), inp);
      (void) sscanf(one_line, "%le\n", &param[h]);
      /*printf("constant %i is %g\n", h, param[h]);*/
      }

fclose(inp);
printf("--------------------------------\n");

g = param[1];
Sol = param[2];
abd = param[3];
ems = param[4];
R_m = param[5];
Tsi0 = param[6];
rhi = param[7];

M_N2_s = param[8];
M_O2_s = param[9];
M_Ar_s = param[10];
M_CO2_s = param[11];
M_H2O_s = param[12];

k_CO2 = param[13];
k_H2O = param[14];

dT = param[15];
ds = param[16];
d_feed = param[17];

Tsi = Tsi0;
/* Processing */
S_m = 4*M_PI*pow(R_m,2);

T_s = surftemp(Sol, M_N2_s, M_O2_s, M_Ar_s, M_CO2_s, M_H2O_s);

strcpy (OUTPUT_FILE, FILE_NAME);
strcat (OUTPUT_FILE,".dat");
outp = fopen(OUTPUT_FILE,"w");
fprintf(outp, "zl,  ro_CO2, ro_H2O, ir_od, Tr, Ta, Tc\n");
for  (j=1; j<=nol; j++)
fprintf(outp, "%.4f, %.3e, %.3e, %.2f, %.2f, %.2f, %.2f\n", zl[j]/1000,
ro_CO2[j], ro_H2O[j], ir_od[j], Tr[j], Ta[j], Tc[j]);
fclose(outp);

strcpy (OUTPUT_FILE, FILE_NAME);
strcat (OUTPUT_FILE,"_p.dat");
outp = fopen(OUTPUT_FILE,"w");
fprintf(outp, "Tsi0, Sol, M_CO2_s, Te, T0, P_H2O_a, M_H2O_a, rh, rov_s,
roc_s, P_atm, DALR, SALR, MALR, H_atm, H_CO2, H_H2O, Tsr, Z_tropo, T_s\n");
fprintf(outp, "%.2f, %.f, %.2e, %.2f, %.2f, %.f, %.3f, %.6f, %.3e, %.3e,
%.2e, %.3f, %.3f, %.3f, %.1f, %.1f, %.1f, %.2f, %.0f, %.2f\n", //
            Tsi0, Sol, M_CO2_s, Te, T0, P_H2O_a, M_H2O_a, rh, rov_s, roc_s,
P_atm, DALR*1000, SALR*1000, MALR*1000, H_atm, H_CO2, H_H2O, Tsr, Z_tropo,
T_s);
fclose(outp);
```

```
printf("Effective temperature is Te = %.2f K\n", Te);
printf("Absolute temperature is T0 = %.2f K\n", T0);
printf("Water vapour pressure at surface is P_H2O_a = %.3f Pa\n", P_H2O_a);
printf("Water in atmosphere is M_H2O_a = %.3f kg\n", M_H2O_a);
printf("Saturated water in atmosphere is M_H2O_sat = %.3f kg\n", M_H2O_sat);
printf("Relative humidity is rh = %.3f \n", rh);
printf("Atm pressure at surface is P_atm = %.3f Pa\n", P_atm);
printf("DALR = %.3f \n", DALR*1000);
printf("SALR = %.3f \n", SALR*1000);
printf("MALR = %.3f \n", MALR*1000);
printf("Atm scale is H_atm = %.3f m\n", H_atm);
printf("Water vapour scale is H_H2O = %.3f m\n", H_H2O);
printf("Radiative temperature is Tsr = %.2f K\n", Tsr);
printf("Troposphere height is Z_tropo = %.0f m\n", Z_tropo);
printf("Surface temperature is T_s = %.2f K\n", T_s);
printf("rwyg = %i \n", runwyg);
      if (runwyg == 0)
            printf("NORMAL CONDITION!\n");
      else
            printf("RUNNAWAY CONDITION!\n");
printf("Done!\n");
printf("**********************************************************************
*\n");

return 0;
}
```

surftemp.h

```
/*****************************************************************************
 *   Copyright (C) 2007 by Constantin Sandu   *
 *   csandu@rice.edu   *
 *                                                                           *
 *                                                                           *
 *****************************************************************************/
     # define MAX_LAYERS 100000
     /* Input */
     float Tsi;
     double g, R_m, S_m;
     double abd, ems, rh, rhi;
     double k_CO2, k_H2O;
     float  ds, dT, d_feed;
     /* Output */
     float  Tr[MAX_LAYERS], Ta[MAX_LAYERS], Tc[MAX_LAYERS];
     double zl[MAX_LAYERS];
     double ro_a[MAX_LAYERS], ro_CO2[MAX_LAYERS], ro_H2O[MAX_LAYERS];
     float ir_od[MAX_LAYERS];
     float Te, T0, Tsr, DT_forc;
     float rh_max, rov_s, roc_s;
     double P_atm, Z_tropo, P_H2O_a, M_H2O_a, M_H2O_sat;
     float H_atm, H_H2O, H_CO2;
     double DALR, SALR, MALR;
     unsigned short int nol, tol;
     int runwyg;
     double dl[MAX_LAYERS], Rl[MAX_LAYERS];
```

surftemp.c

```
/*************************************************************************
 *   Copyright (C) 2007 by Constantin Sandu   *
 *   csandu@rice.edu   *
 *
 *************************************************************************/
# define _USE_MATH_DEFINES
# include <math.h>
# include <stdio.h>

# define m_N2 28.02E-3
# define m_O2 32.00E-3
# define m_Ar 39.95E-3
# define m_CO2 43.01E-3
# define m_H2O 18.02E-3
# define cp_N2 1.04E3
# define cp_O2 0.92E3
# define cp_Ar 0.52E3

# define cp_H2Ol 4.2E3
# define cp_H2Ov 2.0E3
# define lbdv_H2O 2.2E6
# define sbz 5.67e-8
# define kbz 1.3807E-23
# define R 8.31447

double ma, cpa, Ha, Hw, Pa, P_H2O;

float surftemp(float S, double M_N2, double M_O2, double M_Ar, double M_CO2,
double M_H2O)
      {

      float Ts;
      /* Input */
      extern float Tsi;
      extern double g, R_m, S_m;
      extern double abd, ems, rh, rhi;
      extern double k_CO2, k_H2O;
      extern float  ds, dT, d_feed;
      /* Output */
      extern float Tr[], Ta[], Tc[];
      extern int runwyg;
      extern float Te, T0, Tsr, DT_forc;
      extern float rh_max, rov_s, roc_s;
      extern double P_atm,  Z_tropo, P_H2O_a, M_H2O_a, M_H2O_sat;
      extern float H_atm, H_H2O, H_CO2;
      extern unsigned short int nol, tol;
      extern double ma, cpa, Ha, Pa, MALR, DALR, SALR;
      extern double zl[], dl[], Rl[];
      extern double ro_a[], ro_CO2[], ro_H2O[];
      extern float ir_od[];

      /* Internal param */
      unsigned short int j, q, swc1;
      float Tt, Tavg, Tn1, Tn, DT, Tci, Tci_1, Tsi0;
      float var_dir;
```

```
double Ma, P_CO2, maxP_H2O, maxP_H2Oa;
double Hc, Hwd, cp_CO2, k_CO2i;
float tau_CO2, tau_H2O;
double BALQn1, BALQn;
double M_H2O_t_0, M_H2O_sat_t_0, M_H2O_t, M_H2O_sat_t;
double vappres(float Tv);
float Tvap(double Pv);
double balqT(float Temp);

/* Effective radiating temperature */

Te = pow((S*(1-abd)/(4*ems*sbz)),0.25);
T0 = pow(2,-0.25)*Te;

/* Physical chemistry parameters dry */
Ma = M_N2+M_O2+M_Ar+M_CO2;
ma = Ma/(M_N2/m_N2+M_O2/m_O2+M_Ar/m_Ar+M_CO2/m_CO2);


/* Processing */

/* WET Calculations */
runwyg = 0;

var_dir = 0;
rh = rhi;
Tsi0 = 0;
Ts = Tsi;

P_H2O = 0;
maxP_H2Oa = M_H2O*g/S_m;

swc1 = 1;

/*Processing*/


do
{

        Tsi = Ts;
printf("Testing Tsi: %.2f\n", Tsi);
        cp_CO2 = (24.9+55.1*Tsi/1000-
33.6*pow(Tsi/1000,2)+7.9*pow(Tsi/1000,3)-0.1*pow(Tsi/1000,-2))/m_CO2;
        cpa =
(ma/Ma*(cp_N2*M_N2/m_N2+cp_O2*M_O2/m_O2+cp_Ar*M_Ar/m_Ar+cp_CO2*M_CO2/m_CO2));
        P_H2O = rh*vappres(Tsi);

        maxP_H2O = vappres(Tsi);
        if (P_H2O > maxP_H2Oa)
              P_H2O = maxP_H2Oa;
printf("P_H2O  %.3f\n", P_H2O);
        rov_s = P_H2O*m_H2O/(R*Tsi);
        Pa = Ma*g/S_m;
        P_CO2 = M_CO2*g/S_m;

        /* Adiabats */
```

```
            DALR = g/cpa;

            SALR =
DALR*(1+lbdv_H2O*maxP_H2O*m_H2O/Pa/R/Tsi)/(1+pow(lbdv_H2O,2)*maxP_H2O/Pa*m_H2
O/ma/cpa/R*m_H2O/pow(Tsi,2));
            MALR = DALR*(1+lbdv_H2O*
P_H2O*m_H2O/Pa/R/Tsi)/(1+pow(lbdv_H2O,2)*
P_H2O/Pa*m_H2O/ma/cpa/R*m_H2O/pow(Tsi,2));

            /* Scale heights */
            Ha = R*(Te+Tsi)/2/ma/g;

            Hc = R*(Te+Tsi)/2/m_CO2/g;

            /*Hw = (R/ma*pow(Tsi,2))/(g*Tsi+5417*R/ma*SALR);*/
            /*Hw = ((Tsi-T0)/MALR)/log(P_H2O/(rh*vappres(T0)));*/
            Hw = -((Tsi-T0)/MALR)/log(vappres(T0)/P_H2O);

            Hwd = R*(Te+Tsi)/2/m_H2O/g;

            if (Hw > Hwd)
                  Hw = Hwd;
            ro_CO2[0] = m_CO2/(R*Tsi)*P_CO2;

            ro_H2O[0] = m_H2O/(R*Tsi)*P_H2O;

            ro_a[0] = ma/(R*Tsi)*Pa;

            k_CO2i = k_CO2-0.270917E-4*(Tsi-288);

            /* Surface radiative equilibrium temperature */
            tau_CO2 = k_CO2i*ro_CO2[0]*Hc;
            tau_H2O = k_H2O*ro_H2O[0]*Hw;
            ir_od[0] = tau_CO2+tau_H2O;

            Tsr = Te*pow((0.75*ir_od[0]+0.5),0.25);

            /* Radiative profile */
            j = 0;
            dl[0] = 0;
            zl[0] = 0;
            Rl[0] = R_m;
            Tr[0] = Tsr;
            Ta[0] = Tsr;
            Tci_1 = Tsi;
            Tci = Tsi;
            M_H2O_t_0 = 0;
            M_H2O_sat_t_0 = 0;

            tol = 0;

            while ((Ta[j] > Tr[j]) || (j == 0))

            {
                  j=j+1;

                  dl[j] = ds*j;
```

```
                zl[j] = zl[j-1]+dl[j-1]/2+dl[j]/2;
                Rl[j]  = Rl[0]+zl[j];
                Tci_1 = Tci;
                Tci = Tsi-MALR*zl[j];

                if ((j > tol) && (tol > 0))
                      Tci = Tr[j-1];
                ro_CO2[j] = m_CO2/(R*Tci)*P_CO2*exp(-zl[j]/Hc);
                ro_H2O[j] = m_H2O/(R*Tci)*P_H2O*exp(-zl[j]/Hw);
                ro_a[j] = ma/(R*Tci)*Pa*exp(-zl[j]/Ha);
                tau_CO2 = Hc*k_CO2i*ro_CO2[j];
                tau_H2O = Hw*k_H2O*ro_H2O[j];
                ir_od[j] = tau_CO2+tau_H2O;
                Tr[j]= Te*pow((0.75*ir_od[j]+0.5),0.25);
                Ta[j]=Ta[0]-MALR*zl[j];
                M_H2O_t_0 = M_H2O_t_0+ro_H2O[j]*dl[j];
                M_H2O_sat_t_0 =
M_H2O_sat_t_0+vappres(Tci)*m_H2O/(R*Tci)*dl[j];
                if ((Tci <= Tr[j]) && (Tci_1 > Tr[j-1]))
                {
                      tol=j;
                      M_H2O_t = M_H2O_t_0;
                      M_H2O_sat_t = M_H2O_sat_t_0;

                }
          }
          nol = j;

          /* Convective adjustment  */

          Tn1 = Tsr;
          BALQn1 = balqT(Tn1);
          Tn = Te;
          BALQn = balqT(Tn);
          for (q = 1; q <= 100; q++)
          {
                DT = (Tn-Tn1)/(BALQn-BALQn1)*BALQn;
                if (fabs(DT) < dT)
                {
                      Ts = Tn;
                      break;
                }

                Tn1 = Tn;
                BALQn1 = BALQn;
                Tn = Tn-DT;
                BALQn = balqT(Tn);
          }
          Tc[0] = Tn;
          Ts = Tn;

/*************************************************************************
***************/
     /* Max rh*/
          Tt = Tc[tol];
printf("Ts: %.2f  Tt: %.2f\n", Ts, Tt);
          Tavg = (Ts-Tt)/2;
```

```
            Z_tropo = zl[tol]+dl[tol]/2;


            P_H2O = P_H2O*(1+d_feed*(Ts-Tsi));
            rh = P_H2O/vappres(Ts);
            if (rh > 1)
                  rh = 1;



            if (fabs(Tsi-Tsi0) <= fabs(Ts-Tsi))
            {

                  runwyg = 1;

            }
            if (Tsi0 == 0)
                  var_dir = 0;
            else
                  var_dir = (Ts-Tsi)/(Tsi-Tsi0);

            Tsi0 = Tsi;

      }     while ((fabs(Ts-Tsi) > 0.2) && (var_dir >= 0));

printf("END WHILE\n");

      for (j=tol; j<=nol; j++)
            {
            Tc[j]=Tr[j];
            }


      P_H2O_a = P_H2O;
      M_H2O_a = M_H2O_t;
      M_H2O_sat = M_H2O_sat_t;
      P_atm = Pa;
      H_atm = Ha;
      H_H2O = Hw;
      H_CO2 = Hc;

      return Ts;
}

double balqT(float Temp)
      {
      double Ql, SumQ;
      unsigned short int j;
      extern unsigned short int nol, tol;
      extern float Tr[], Tc[];
      extern float Tsi;
      extern double ma, cpa, Ha, Hw, Pa, MALR, SALR;
      extern double M_H2O_a, P_H2O, M_H2O_sat;
      extern double zl[], dl[], Rl[];
      double vappres(float Tv);
```

```
        SumQ = 0;

        Tc[0] = Temp;


        for (j=1; j<=nol; j++)
              {

              Tc[j] = Temp-MALR*zl[j];
              Ql = Pa*ma/(R*Tc[j])*exp(-zl[j]/Ha)*cpa*(Tc[j]-Tr[j])*dl[j];
                    /* *pow(Rl[j],2)*4*M_PI */


              SumQ = SumQ+Ql;
              if ((Tc[j] <= Tr[j]) && (Tc[j-1] > Tr[j-1]))
                    {
                    tol=j;
                    break;
                    }
              }

        return SumQ;
        }
/*************************************************************************
****************/
```

sample.inp
sample input file

```
0           "sw1"  "Climate effect"                "0,1"
1           "sw2"  "Volatile dependent"           "0,1"
0           "sw3"  "Viscosity law"                "0=Li, 1=Anita, 2=Aheim"
0           "sw4"  "Areal Spreading law"                "0=vel, 1=area"
0           "sw5"  "Degassing"            "0=melt, 1=ct"
0           "sw6"  "Regassing"            "0=hydr, 1=ct"
0           "sw7"  "Stagnant lid"         "0,1"
0           "t_start "      "Start time"    "[Ma]"
4600        "t_end"         "End time"      "[Ma]"
3000        "Tm_ini"        "Initial mantle temperature"  "[K]"
300         "Ts_ini"        "Initial surface temperature"  "[K]"
4.51E+000           "Q_ini "        "Initial radioactive heat"      "[J/(m^3*y)]"
3.91E+018           "M_N2a_ini"  "Nitrogen mass in atmosphere"       "[kg]"
1.20E+018           "M_O2a_ini"  "Oxygen mass in atmosphere"         "[kg]"
3.08E+015           "M_CO2a_ini"        "Carbon dioxide mass in atmosphere"       "[kg]"
0.00E+000           "M_H2O_s_ini"       "Initial water at surface"      "[kg]"
4.17E+021           "M_H2O_m_ini"       "Initial water in mantle"       "[kg]"
1028        "Sol_ini"       "Initial solar radiation"       "[W/m^2]"
9.8         "g "    "Gravity constant"      "[m/s^-2]"
3471000             "R_c " "Lower mantle boundary (radius)"    "[m]"
6271000             "R_m "          "Upper mantle boundary (radius)"    "[m]"
3000        "ro_m""Density of mantle"   "[kg*m^-3]"
4.2         "k_m"  "Thermal conductivity of mantle"     "[W/m/K]"
1400        "cp_m"          "Specific heat of mantle"       "[J/kg/K]"
3.00E-005           "alpha "        "Coefficient of thermal expansion"   "[K^-1]"
1           "a"     "Frank-Kamenetskii constant"
0           "b"     "Frank-Kamenetskii exponent"
0.3         "beta"  "Scaling factor for convection"
3.40E-010           "lbd "  "Radioactive decay constant" "[y^-1]"
1100        "Ra_cr "        "Critical Ra"
1.78E+017           "eta0"  "Viscosity constant"   "[Pa*s]"
90          "Acre "         "Viscosity material constant" "[MPa^-r/s]"
1.2         "r "    "Viscosity exponent constant"
4.80E+005           "AE_c"          "Activation energy for creep" "[J/mol]"
1.70E+008           "tau_ex"        "Exospheric escape time for H"        "[Ma]"
0.3         "abd"   "Integrated planetary albedo"
1           "ems"   "Planetary emissivity"
1.45E-030           "k_CO2"         "Infrared absorption coefficient for CO2"
1.18E-026           "k_H2O"         "Infrared absorption coefficient for H2O"
0.08        "r_SOL "        "Solar radiation gain rate"     "[W/m^2/MA]"
0.45        "rh"    "Relative humidity of atmosphere"
1.00E+005           "d_melt"        "Equivalent depth of melt"
0.13        "f_bas""Fraction of volatile in basalt"
```

```
2950        "ro_bas"      "Density of basalt"
5000        "d_bas"       "Average thickness of basaltic crust"
0.05        "Xt_d" "Degassing efficiency factor"
0.009       "Xt_r" "Regassing efficiency factor"
0.05        "Xs_d""Degassing efficiency factor"
0.0         "Xs_r" "Regassing efficiency factor"
1           "ts "   "Time step (elem. time interval)"     "[Ma]"
1           "ds"    "Atmosphere calculation spacing"    "[m]"
1           "dT"    "Surface temperature increment step"        "[K]"
1000        "dz"    "Mantle calculation spacing"  "[m]"
0           "tau_cr"
0           "Z_sl_ini"      "[m]"
```